PHASE CONTRAST IMAGING OF LASER-INDUCED MICROCAVITATION

A Thesis

by

KEVIN J. LY

Submitted to the Office of Graduate and Professional Studies of
Texas A&M University
in partial fulfillment of the requirements for the degree of

MASTER OF SCIENCE

Chair of Committee,	Sy-Bor Wen
Committee Members,	Philip Hemmer
	Adonios Karpetis
Head of Department,	Andreas A Polycarpou

December 2018

Major Subject: Mechanical Engineering

ABSTRACT

As the medical field becomes more advanced, the scale of operation becomes increasingly smaller. Due to this trend, traditional mechanical tools like a scalpel may not become fine enough to be used for such manipulation. As a result, laser based medical surgeries such as LASIK (Laser assisted in situ keratomileusis) have become popular in recent decades. The associated laser tissue interactions, in particular photoablation, have become an important field of study to reduce unpredictable aftereffects of laser surgery. A consequence of photoablation is laser-induced microcavitation. Laser – induced microcavitation is a process in which optical energy from a laser converts to thermal energy of the tissue and creates a shockwave and a vapor bubble inside a liquid rich environment. As most bio-tissue is liquid rich, laser-induced microcavitation is an important field to study. There have been a number of theoretical and experimental studies regarding laser-induced microcavitation. However most theoretical studies are semi-analytical and focus on the oscillation of the cavitation bubble after it has formed. Additionally, most visual experimental studies use brightfield microscopy to image the microcavitation process. In order to supplement the existing theoretical and experimental studies, this thesis will develop a thermodynamic numerical simulation for the early (< 1 μs) microcavitation process and an experimental setup to image microcavitation develop with phase contrast microscopy. The goal of the numerical simulation is to accurately model the microcavitation process. The corresponding goal of the experimental setup is to identify additional features not visible in brightfield microscopy. The numerical simulation developed in this study was able to

model the bubble and shockwave features, but still needs refinement due to only considering linear light absorption instead of plasma induced ablation. The pulsed illumination phase contrast microscopy developed in this study was able to image the vapor bubble boundary with higher contrast and resolve additional features in the high pressure region between the bubble and shockwave. As phase contrast microscopy is a qualitative imaging rather than a quantitative imaging process, the next step is to use differential interference contrast (DIC) microscopy to quantify the features resolved in phase contrast microscopy.

DEDICATION

I would like to dedicate this thesis to my parents and professors.

ACKNOWLEDGEMENTS

I would like to thank my committee chair, Dr. Sy-Bor Wen, for his guidance and support throughout the course of this research. I would also like to thank my committee members, Dr. Adonis Karpetis and Dr. Phillip Hemmer for the guidance and helpful discussions.

I would like to thank my colleagues Arun Bhaskar, Aravind Jakkinapalli, and Hongjie Zhang for their valuable discussion and support. I would like to thank Dr. Robert Thomas for providing access to the Air Force Research Laboratory, Dr. Morgan Schmidt for providing advice on the microscopy setup, and Gary Noojin for providing technical support and advice.

Finally, I would like to thank my mother, father, and sister for their encouragement and support.

CONTRIBUTORS AND FUNDING SOURCES

This work was supervised by a thesis committee consisting of Dr. Sy-bor Wen and Dr. Adonis Karpetis of the Department of Aerospace Engineering and Dr. Phillip Hemmer of Department of Electrical & Computer Engineering.

All work for the thesis was completed by the student, under the advisement of Professor Sy-bor Wen of the Department of Mechanical Engineering. This work was made possible in part by Air Force Contract FA8650-14-D-6519 (Engility Corporation) and the US Air Force Summer Faculty Fellowship Program.

Its contents are solely the responsibility of the authors and do not necessarily represent the official views of the Engility or the Air Force Research Laboratory.

TABLE OF CONTENTS

Page

LIST OF FIGURES

1 INTRODUCTION[*]

1.1 Laser Surgery Overview

As the medical field becomes more advance, the scale of operation becomes increasingly smaller. Due to this trend, traditional mechanical tools like a scalpel may not become fine enough to be used for such manipulation. As a result, laser based medical surgeries such as LASIK (Laser assisted in situ keratomileusis) providing tens of micrometers resolutions have become popular in recent decades [1]. Due to this popularity, laser-tissue interactions have become an important field to study. The study of the interactions between the biomaterial and the laser are typically considered in three classes: photochemical interactions, thermal interactions, and photoablation [2-4]. Study of photochemical interactions focuses on empirical observations of chemical effects and reactions within macromolecules or tissues that typically occurs at very low power densities (~1 W/cm^2) over long exposure times (continuous wave down to seconds). Study of thermal interactions focuses on observations of thermal effects that typically occurs at low power densities (~1000W/cm^2) over long exposure times (1 min down to 1 μs). Study of photoablation focuses on tissue removal though a laser or with higher power density (~10^7-10^{14} W/cm^2) and short exposure time (<1 μs) [5]. As laser surgeries like LASIK occurs using nano- and pico-second pulses to remove tissue, an understanding of photoablation is the more important interactions to be studied [6].

1.2 Photoablation

In order for photoablation to occur, energy needs to be transferred from the laser to the tissue. Light interacts with the tissue is mainly through valence electron interactions with photon

---

[*] Part of this chapter is reprinted with permission from "Direct numerical simulation of microcavitation processes in different bio environments" by Kevin Ly, Sy-bor Wen, Morgan s. Schmidt, and Robert J. Thomas, 2017. *Optical Interactions with Tissue and Cells Xxviii*, Vol. 100602, Copyright 2017 by SPIE.

energy. The absorption mechanisms can be either single or multi-photon absorption. Multiphoton absorption is one of the non-linear process for which elections absorb multiple photons simultaneously [7]. Multiphoton absorption is possible with ultrafast light (e.g., femtosecond pulsed laser) due to having high peak light intensities. However due to the limited availability of high powered femtosecond lasers, photoablation due to multiphoton absorption is not considered in our study.

Single photon absorption is a process where a single photon excites an electron. The most common excitation process is from the valence band to the conduction band[8]. Linear light absorption is one of many single photon absorption mechanisms in which excited electrons can go into the conduction band and collide with other electrons and surrounding atoms. The collisions will raise the thermodynamic (i.e., temperature and pressure) energy of the irradiated material [5]. Ablation occurs when thermodynamic energy raises the temperature of the irradiated tissue is high enough to induce vaporization or plasma formation and the following material ejection [9].

In some high power density cases (~10^{11}-10^{14} W/cm^2), electrons in the conduction band can also absorb additional photons have even higher kinetic energy [2]. The resulting high kinetic energy electrons can strike and move additional electrons from the valence band into the conduction band as an avalanche process, which is called optical breakdown. The avalanche process will eventually create a temporary pool of electrons in the conduction band [10]. The electrons pool will continue to absorb photon energy and transfer the energy to atom in the form of thermodynamic energy (i.e., temperature and pressure). This will in turn heat the atoms to a high enough temperature to induce vaporization or plasma formation and the following material ejection [9]. Optical breakdown can happen at near infrared wavelengths in bio-tissues as the high transmissivity reduces the amount of energy lost due to linear light absorption [11]. The higher transmitted near IR energy allows for high power densities to form inside the bio-tissue with a focused laser and induce vaporization and/or plasma formation [12]. This vaporization and/or plasma formation can induce microcavitation in soft bio-tissues.

1.3 Laser-Induced Microcavitation

Laser – induced microcavitation is a process in which optical energy from a laser is converted to thermal energy of the tissue and creates a shockwave and a vapor bubble inside a liquid rich environment. Laser –induced microcavitation can be created from the photoablation mainly through light absorption and/or optical breakdown when ns laser is applied. Microcavitation from linear light absorption occurs when the temperature of the molecules is high enough to start vaporization and forms a vapor bubble around the focal spot inside the water rich material. Microcavitation from optical breakdown occurs when the thermal energy accumulated in the pool of electrons in the conduction band is dissipated in the form of shock waves and/or vapor bubble formation. In bio-tissue at IR wavelength, optical breakdown can occur before linear light absorption as the absorption coefficient is extremely low. Therefore, Avalanche breakdown is the dominant mechanisms of microcavitation in most highly transparent water rich substances such as bio-tissues. For less transparent bio-tissue, linear light absorption can also be important in the laser-induced microcavitation process. Since the first LASIK surgery, there are numerous studies focusing on dynamics of laser-induced microcavitation. Vogel et al. studied the formation, oscillation and collapse of the vapor bubble in nanosecond (ns) and femtosecond (fs) laser pulses [13-15]. Blake et al. investigated the dynamics of cavitation bubbles near boundaries [16]. Kodama et al. studied bubble-shockwave interaction during a microcavitation process as well as bubble interactions with elastic boundaries [17]. Schmidt et al. investigated microcavitation processes of retinal pigment epithelium (RPE) melanosomes and polystyrene microspheres [18-20].

1.4 Laser Microscopy

Most of the experimental studies regarding microcavitation used microscopy to visualize the microcavitation process. Brightfield, darkfield, and phase contrast are the most common microscopy methods [21]. Of these three methods, brightfield microcopy is the most straightforward and is the microscopy method used by the many microcavitation studies [17, 22-25]. The brightfield method creates an image via light transmission though a specimen. In other words, light pass through a sample and creates an image that is collected by the objective. Absorption, scattering, and deflection of the light with the sample will translate to intensity variation in the image. The intensity variation can be used to identify features in the sample [26]. However, if the sample does not absorb much light (is transparent), then finer details of the sample might not be imaged as well [27]. This might be the case with microcavitation bubbles as both the water and water vapor transmit a significant amount of visible light. Thus is might be beneficial to use another microscopy method to view the microcavitation event.

Darkfield microscopy is one of the microscopy methods that can better resolve transparent samples. While brightfield microscopy images are based on spectral absorption, darkfield microscopy images is based on collection of light that is diffracted from the sample [21]. In a darkfield microscopy, the illumination light enters the sample with a steep oblique angle from all azimuthal directions. The steep incoming angle of illumination is even larger than the numerical aperture of the objective lens. Thus, the objective lens does not collect any incident beam directly. In other words, only the diffracted light from the sample can be collect as the image after the objective lens. However, to properly use darkfield microscopy, high intensity illumination light is required for the objective to be collected enough diffracted light to image the sample. The high intensity of the illumination light can possibly damage biomaterial samples, so another diffraction based mode might be better.

Phase contrast microscopy also images based on diffraction like darkfield microscopy, but does so through phase shifting the diffracted light of the sample from the light to enhance the destructive interference with the undiffracted light. . There are many techniques that could accomplish phase contrast microscopy, with the most common being Zernike phase contrast microscopy and Differential Interference Contrast (DIC) microscopy [28]. Zernike Phase contrast microscopy uses a phase plate to shift the diffracted light. The phase plate will have regions that will phase shift and/or reduce the intensity of the g passing through it. For most Zernike phase contrast microscopes, there is a phase shifting ring. Typically, the phase shifting region changes the undiffracted light, also known as the surround light. The phase shifting region correspond to an annulus that shapes the light prior to going through the condenser of a microscope. As the undiffracted light will not deviate from the original optical path, it will only travel though the phase shifted part of the phase plate. The resulting image is created from the interference pattern between the diffracted and altered undiffracted light [29]. Differential interference contrast microscopy (DIC) is a variation of phase contrast microscopy that uses the interference between two different polarized light that are diffracted by the sample. The two polarized lights were formed by passing polarized light through a Normarski prism. After the two lights pass through the sample, another Normarski prism combines the diffracted lights. The resulting diffraction pattern is the image after the combined light passes through a polarizer that removes the any light in the original polarization. [30].

1.5 Pulsed Laser Microscopy

To increase the time resolution of the imaging process to nanoseconds, the continuous semi-coherent illumination used in microscopy will be replaced with a pulsed laser semi-coherent illumination. This pulsed laser is considered as a high temporal resolution probe (strobe) laser and will be used to illuminate the sample at different delay times with ns exposure time. The resulting imaging process will be microscopy pulsed laser microscopy, which will allow for imaging of the microcavitation process.

1.6 Scope of the Study

The goal of this study is to better understand the early development of the microcavitation process. The study is primarily experimental with an emphasis on laser-based microscopy, however the study contains a numerical model as well. Based on the previous studies, many of the microcavitation numerical models were limited in scope and tend to not focus on early stage laser-induced microcavitation [31]. A model focusing on early stage microcavitation would be beneficial for studying heating and stress during the early microcavitation process. Therefore, we try to solve a portion of the early microcavitation process by creating a numerical model based on the conservation equations of water-rich bio-tissue. If successful, the model can be used to simulate the temperature, pressure, and vapor quality among other physical values during microcavitation under various conditions. The values can be used to find the optical conditions to reduce damaging physics effects of microcavitation surgery like high heat zones and high peak stress values.

Previous microscopy setups have been focused on brightfield imaging, which can have difficulty identifying features in transparent samples like water-rich bio-tissue. Phase Contrast microscopy and DIC microscopy utilizes diffraction, which might better identify features in the transparent samples. With available equipment, phase contrast will be used as a basis for a new laser-induced microscopy setup. The new setup will also allow for brightfield laser imaging so that phase contrast and brightfield laser imaging can be compared. The new setup will be used to image the cavitation process in distilled water and 10% polyacrylamide gel in water solution (10% PAA gel) as both materials have similar properties to transparent optical tissue, particularly in the threshold for plasma formation [15].With this comparison, we hope to identify additional details of the cavitation process. Discovery of the additional details will allow for a better understanding of the laser-induced microcavitation process and the effects of the process on surround biomaterial in a laser surgery.

2 THEORETICAL BACKGROUND AND INTEGRATED ANALYSIS*

2.1 Introduction

This section will provide the theoretical background for the numerical model of early laser-induced microcavitation formation. Many models regarding microcavitation have already exist for some time. For example, H.G. Flynn presented a model to determine the evolutions of cavitation bubbles formed through ultrasound pulses varying from 1 MHz to 10 MH in inhomogeneous solutions though semi-analytical analysis. Flynn's semi-analytic model is based on mass, momentum, and energy conservations of the simulation domain. By using integral method with uniform density and linear velocity variation from the center to the interface of vapor bubble/surrounding liquid, Flynn's was able to determine the evolution of the size of the vapor bubble as well as its density variation after the formation of the vapor bubble. By furthering solving the heat transfer equation in the vapor and liquid domains, Flynn also determined the temperature and pressure distributions in the vapor bubble and surrounding with a help of equation of state and/or isentropic assumptions [31-33]. While this model can be used to determine the evolution of the size of the vapor bubble, the adopted uniform density and linear velocity variation assumptions do not allow accurate modeling of the physical values within the vapor bubble.

Compared with above assumptions for above semi-analytical model, a pure numerical analysis require much less assumption that would make the obtained solutions more realistic. Numerical solution for microcavitation under 1D assumption that the bubble is perfectly spherical and all fields are rotational symmetric have been adopted by many research groups. For example, Keller

---

* Part of this chapter is reprinted with permission from "Direct numerical simulation of microcavitation processes in different bio environments" by Kevin Ly, Sy-bor Wen, Morgan s. Schmidt, and Robert J. Thomas, 2017. *Optical Interactions with Tissue and Cells Xxviii*, Vol. 100602, Copyright 2017 by SPIE.

Miksis 1D simulation model has been developed to model collapse of the microcavitation bubble. Governing equations of this model under 1D simplification can be solved numerically either by Saurel-Abgrall approach in order to model two phase flow or real ghost fluid method in order to handle compressible liquid-gas flow across the phase interface. Compared with the experimental data, this 1D model was able to determine a possible cause of the bubble collapse near a ridge boundary as the gas accelerated inside the bubble due a shockwave reflecting off the phase boundary of the bubble and surrounding fluid. [32].

Zein also developed multiple models to numerical investigate the collapse and rebound of a laser-induced cavitation bubble in liquid water. The basis of the models are on mass, momentum and energy conservation equations in multi-phase flow. The first model has the water vapor and liquid water phase, while the second model also includes non-condensable gas phase inside the bubble. The interfacial pressure is calculated with acoustic impedance. These conservation equations are solved using Strang splitting, a numerical scheme in solving multidimensional partial differential equations, with relaxation solved in the following order: pressure, then temperature, then Gibbs free energy. The results of this solution are shown with respect to time for the radius of the bubble, the pressure and temperature at the center of the bubble, and the velocity at the interface. Experimental results of bubble radius over time was used to verify the fidelity of the model. Using this model, Zein was able to determine that in order for a cavitation bubble in the mass transfer model to rebound similarly to that of the experimental data, it must contain a sufficient amount of non-condensable gas. The amount and composition of this gas will also effect on the behavior the rebound [33]. While this model allow physical values to be measured within and outside of the bubble, the assumption the bubble is perfectly spherical and rotationally symmetrical reduces its scope.

Mueller did not limit himself to one dimension by developing a two dimensional compressible flow model of laser-induced cavitation in free flow and near a solid boundary. Basis of Mueller's model were also on the mass, momentum, and energy equation for inviscid flow along with the stiffened equation of state. The stiffed equation of state is used for water under very high pressure, which is what a cavitation bubble would do to the surround material. The model assumes that there is negligible gravity, surface tension, viscosity, and heat conduction. This numerical model is solved using upwind finite volume discretization [32]. Many of these assumptions still cannot be applied for initial formation stage of a laser-induced microcavitation bubble, which reduce the scope of the model. So an improved model would be beneficial especially for studying the formation stage of a laser-induced vapor bubble.

To develop a new model that can describe the initial stage of laser-induced vapor bubble leads to the numerical model established in this section. The core of this new model will be the conservation equations. However, to ensure that the material properties of the model matches better with those of water-rich bio-tissues, a more specific equation of state and internal energy equation was developed. The development of these two equations are explained in sections 2.2 and 2.3 respectively. The model does ignore gravity as gravitation effects are negligible in microscale of the bubble. Viscosity and heat conduction are accounted for in the development of the conservation equations shown in Section 2.4. To describe laser transport and absorption in the bio-tissue, an additional model using wave optics is made to calculate the heat generation from the later at different locations in the microcavitation model. Details of this model will be explained in section 2.5, which is followed with a summary of the theoretical background.

A numerical model simulates laser-induced microcavitation in water rich bio-tissue. Creating these models for this analysis would be beneficial in areas of heat and stress during microcavitation. The subsequent modeling and identification of these physical events would help optimize conditions for laser surgery associated with damage promoting events, such as reduction of heat zones and lessening the peak stress value during laser-induced microcavitation. The core of the model is composed of the governing equations of mass, momentum, and energy conservation in bio-tissue. Additional constitutive equations will be used to solve for temperature, pressure, specific volume, and stress fields during a laser-induced microcavitation event. A modified Peng-Robinson equation of state (PR EOS) and specific volume derived internal energy equation is used to help model the tissue. The energy imparted from the laser is modeled using the time harmonic Maxwell equations at is calculated in a separate model.

2.2 Equation of State for Water-rich Bio-tissues

In the numerical model, it is assumed that the equation of state of water-rich bio-tissues can be approximated with that of water when the bio-tissue is in liquid or vapor phase. When the bio-tissue is in elastic solid phase at lower temperatures and higher density, the equation of state of water gives a higher prediction of the pressure value. Thus a scaling factor is implemented for that particular phase. To illustrate, the modified Peng-Robinson equation of state (PR EOS) is used, which provides a good estimation of pressure, temperature, and specific volume of pure water at the subcooled liquid and superheated vapor phase [34]. The full expression of PR EOS is in eq. 1.

$$a(T) = 0.45724\frac{(RT_c)^2}{P_c}\left[1+m(1-\sqrt{T_r})\right]^2$$

$$m = 0.37464+1.5422\varpi-0.26992\varpi^2 \tag{1}$$

$$T_r = \frac{T}{T_c}\,;\ \tilde{b} = 0.0778\frac{RT_c}{P_c}\,;\ \tilde{v} = v + c$$

with P representing the thermal pressure, T the temperature, v the specific volume, T_c the critical temperature of water (~ 647.1 K), P_c the critical pressure of water (~ 22060 kPa), the acentric factor of water (~ 0.334), c the corrected factor for specific volume (0.24091x10-3 m3/kg), and R the gas constant of water (0.4615 kJ/kg·K). Using the Maxwell equal area rule, the specific volumes of saturated liquid, vapor, and saturated pressure can be determined.

When the temperature of the water-rich bio-tissue is below its dissociation temperature (e.g., ~340 K for stroma of cornea) and the specific volume of the bio-tissue is still around its intrinsic value (~0.001 m3/kg), the fibroblast cells (or collagen in each cell) of the bio-tissue hold the structure of the tissue as an elastic solid. The bulk modulus B of bio-tissue in elastic solid phase varies from MPa level (e.g., stroma of cornea) to GPa level (e.g., brainstem tissue), which can be very different from that determined with the modified PR EOS for pure water (i.e., ~2 GPa). In other words, the pressure determined with eq. 1 can have several orders of magnitude of overestimation when of the bio-tissue is in elastic solid phase. To rectify this error, when T is less than the dissociation temperature and when the specific volume of the bio material is less than v_f as illustrated in Figure 1a, the following equation of state is adopted in eq. 2.

$$\boldsymbol{P}_{\boldsymbol{elastic}} = \left[\frac{RT}{\tilde{v}-\tilde{b}} - \frac{a(T)}{\tilde{v}^2 + 2\tilde{b}\tilde{v} - \tilde{b}^2} - P_{sat}(T) \right] * (scaling\ factor) + P_{sat}(T) \qquad (2)$$

where the scaling factor scales down the pressure increment when the specific volume of the tissue is less v_f . The scaling factor is determined from the experimentally measured bulk modulus B of the bio-tissue, which is a function of elastic modulus E and Poisson ratio v, as eq. 3.

$$(scaling\ \ facotr)\times\left[\frac{RT_{atm}}{\tilde{v}_{atm}-\tilde{b}}-\frac{a(T_{atm})}{\tilde{v}_{atm}^{2}+2\tilde{b}\tilde{v}_{atm}-\tilde{b}^{2}}-P_{sat}(T_{atm})\right]$$
$$=B\frac{\rho_{atm}-\rho_{l}(T_{atm})}{\rho_{l}(T_{atm})}=\frac{E}{1+\nu}\frac{\nu}{1-2\nu}\frac{\rho_{atm}-\rho_{l}(T_{atm})}{\rho_{l}(T_{atm})} \tag{3}$$

with T_{atm} the room temperature; $\tilde{v}_{atm} = v_{atm}+c$ and v_{atm} the specific volume of the tissue under room condition; $P_{sat}(T_{atm})$ the saturated water pressure at room temperature; ρ_{atm} the density of the tissue under room temperature; $\rho_l(T_{atm})$ the density of saturated liquid water under room temperature. The scaling factor becomes one when the temperature of the bio-tissue is higher than the dissociation temperature and when the specific volume of the tissue is still less than v_f.

2.3 Internal Energy, E

In traditional thermo-optics of bio-tissue, internal energy is a function of temperature only. However, this method is invalid for phase changes in the fluid during simulation. A better, more general case would include a dependence on specific volume as shown in eq. 4.

$$de=c_{v}(T)dT+\left(\frac{\partial e}{\partial v}\right)_{T}dv \tag{4}$$

Using Maxwell identity, $(\partial e/\partial v)T$ can be expressed as eq. 5.

$$\left(\frac{\partial e}{\partial v}\right)_{T}=T\left(\frac{\partial P}{\partial T}\right)_{V}-P \tag{5}$$

At higher than critical temperature Tc , the integrated energy equation is eq. 6.

$$e(T,v)_{\text{vapor}}=0.45724\frac{(RT_{c})^{2}}{P_{c}}\left[1+m(1-\sqrt{T_{r}})\right](1+\text{m})\left\{\frac{\ln\left[\dfrac{b+\tilde{v}-\sqrt{2}b}{b+\tilde{v}+\sqrt{2}b}\right]}{2\sqrt{2}b}-\frac{\ln\left[\dfrac{b+v_{R}+c-\sqrt{2}b}{b+v_{R}+c+\sqrt{2}b}\right]}{2\sqrt{2}b}\right\}+fct(T) \tag{6}$$

With the associated de equation being eq. 7.

$$\boldsymbol{de(T,v)}_{\text{vapor}} = \left\{ -0.45724 \frac{(RT_c)^2}{P_c} \left[\frac{1}{2} m \frac{1}{\sqrt{T_r}} \frac{1}{T_c} \right] (1+\mathrm{m}) \left\{ \frac{\ln\left[\dfrac{b+\tilde{v}-\sqrt{2}b}{b+\tilde{v}+\sqrt{2}b} \right]}{2\sqrt{2}b} - \frac{\ln\left[\dfrac{b+v_R+c-\sqrt{2}b}{b+v_R+c+\sqrt{2}b} \right]}{2\sqrt{2}b} \right\} + c_R(T) \right\} dT + \tag{7}$$

$$\frac{0.45724 \dfrac{(RT_c)^2}{P_c} \left[1+m(1-\sqrt{T_r}) \right] (1+\mathrm{m})}{\tilde{v}^2 + 2\tilde{b}\tilde{v} - \tilde{b}^2} dv$$

With $c_R(T)$ the specific heat of the reference high specific volume state which can also be extracted from the IAPWS-95 formula. The internal energy is calculated through substituting the modified PR EOS and approximating the pure function of temperature fct(T) from IAPWS-95 formula due to selecting a large specific volume, vR (~200 m3/kg) [35] .

For the saturated phase, $P = P_{sat}(T)$ making eq. 4 become eq. 8.

$$\left(\frac{\partial e}{\partial v} \right)_T = \left[T \frac{dP_{sat}(T)}{dT} - P_{sat}(T) \right] \tag{8}$$

With the related e and de equation becoming eq. 9 and eq 10.

$$e(T,v)_{\text{saturated}} = \left[T \frac{dP_{sat}(T)}{dT} - P_{sat}(T) \right] \cdot \left[v - v_g(T) \right] + e_g(T) \tag{9}$$

where $e_g(T)$ the internal energy of the saturated vapor at temperature T and specific volume v_g.

$$\boldsymbol{de(T,v)}_{\text{saturated}} = \left\{ T \frac{d^2 P_{sat}(T)}{dT^2} \left[v - v_g(T) \right] - \left[T \frac{dP_{sat}(T)}{dT} - P_{sat}(T) \right] \frac{dv_g(T)}{dT} \right\} dT + \left[T \frac{dP_{sat}(T)}{dT} - P_{sat}(T) \right] dv + de_g(T) \tag{10}$$

For the liquid, eq. (5) is integrated from v to vr and substituted into eq. 5 to form eq. 11 and associate eq. 12.

$$e(T,v)_{\text{liquid}} = 0.45724 \frac{(RT_c)^2}{P_c} \left[1+m(1-\sqrt{T_r}) \right] (1+\mathrm{m}) \left\{ \frac{\ln\left[\dfrac{b+\tilde{v}-\sqrt{2}b}{b+\tilde{v}+\sqrt{2}b} \right]}{2\sqrt{2}b} - \frac{\ln\left[\dfrac{b+v_f+c-\sqrt{2}b}{b+v_f+c+\sqrt{2}b} \right]}{2\sqrt{2}b} \right\} + e_f(T) \tag{11}$$

$$\boldsymbol{de(T,v)}_{\text{liquid}} = \left\{ -0.45724\frac{(RT_c)^2}{P_c}\left[\frac{1}{2}m\frac{1}{\sqrt{T_r}}\frac{1}{T_c}\right](1{+}\mathrm{m})\left\{\frac{\ln\left[\dfrac{b+\tilde{v}-\sqrt{2}b}{b+\tilde{v}+\sqrt{2}b}\right]}{2\sqrt{2}b} - \frac{\ln\left[\dfrac{b+v_f+c-\sqrt{2}b}{b+v_f+c+\sqrt{2}b}\right]}{2\sqrt{2}b}\right\} \right. \tag{12}$$

$$\left. -\frac{0.45724\dfrac{(RT_c)^2}{P_c}\left[1+m(1-\sqrt{T_r})\right](1{+}\mathrm{m})}{\tilde{v}_f^2+2\tilde{b}\tilde{v}_f-\tilde{b}^2}\frac{dv_f}{dT}\right\} dT + \frac{0.45724\dfrac{(RT_c)^2}{P_c}\left[1+m(1-\sqrt{T_r})\right](1{+}\mathrm{m})}{\tilde{v}^2+2\tilde{b}\tilde{v}-\tilde{b}^2}dv + de_f(T)$$

At the elastic solid phase, the low dissociation temperature and high specific volume leads to near incompressible conditions. With the incompressible assumption, the internal energy is almost independent of specific volume. Thus, $\boldsymbol{de}(\boldsymbol{T},\boldsymbol{v})_{elastic\ solid}$ can be estimated from either $\boldsymbol{de}(\boldsymbol{T},\boldsymbol{v})_{saturated}$ or $\boldsymbol{de}(\boldsymbol{T},\boldsymbol{v})_{liquid}$ as both equations are similar at low temperature and near incompressible conditions.

2.4 Conservation Equations

2.4.1 Mass Conservation

A density based approach is used in order to better handle the large density variations of the bio-tissue during microcavitation. The local density eq. 13 will contain the local density ρ, and the local velocity field $\vec{V}$

$$\frac{\partial \rho}{\partial t} = -\nabla \cdot (\rho \vec{V}) \tag{13}$$

2.4.2 Momentum Conservation

The Navier-Stokes equations and the definition of material derivative in Euler (found in eq. 14 and 15) describes the evolution of the velocity field $\tilde{V}$ and the associated displacement field $\tilde{u}$ in the bio-tissue during the microcavitation process.

$$\rho\frac{\partial \vec{V}}{\partial t} + \rho(\vec{V}\cdot\nabla)\vec{V} = \nabla\cdot\bar{\bar{\sigma}} + \vec{F}_b \tag{14}$$

$$\frac{\partial \vec{u}}{\partial t} + (\vec{V} \cdot \nabla)\vec{u} = \vec{V} \tag{15}$$

The gravitational acceleration $\overrightarrow{F_b}$, is negligible in the simulation for early microcavitation. The stress tensor depends on the phase of the tissue. In the elastic material phase, the stress tensor σ_{ik}, can be estimated with linear elastic equations as a first order approximation in eq. 16.

$$\begin{aligned} \sigma_{ik,elastic} &= \frac{E}{1+\nu}\varepsilon_{ik} + \frac{E}{1+\nu}\frac{\nu}{1-2\nu}\varepsilon_{jj}\delta_{ik} - \left[P_o + \frac{E\alpha\Delta T}{3(1-2\nu)}\right]\delta_{ik} = \frac{E}{1+\nu}\varepsilon_{ik} - P_m\delta_{ik} \\ P_m &= \frac{1}{3}\sigma_{jj} = \frac{E}{1+\nu}\frac{\nu}{1-2\nu}\varepsilon_{jj} - \left[P_o + \frac{E\alpha\Delta T}{3(1-2\nu)}\right] + \frac{E}{3(1+\nu)}\varepsilon_{jj} \end{aligned} \tag{16}$$

with E the elastic modulus of the bio-tissue, ν the Poisson's ratio, ε_{ik} the strain tensor which is a function of the displacement field $\vec{u}$ as $(u_{i,j} + u_{j,i})/2$, P_0 the environmental pressure (1 atm in this study), and P_m the mechanical pressure. As most water-rich bio-tissues are highly incompressible with v close to 0.5, the mechanical pressure P_m is approximated with thermodynamic pressure P in eq. 17.

$$P_m = \frac{E}{1+\nu}\frac{\nu}{1-2\nu}\varepsilon_{jj} - \left[P_o + \frac{E\alpha\Delta T}{3(1-2\nu)}\right] + \underbrace{\frac{E}{3(1+\nu)}\varepsilon_{jj}}_{\substack{\text{small compared with} \\ \text{other terms when } \nu\sim 0.5}} \sim \frac{E}{1+\nu}\frac{\nu}{1-2\nu}\varepsilon_{jj} - \left[P_o + \frac{E\alpha\Delta T}{3(1-2\nu)}\right] = P \tag{17}$$

Artificial viscous force is added to the simulation to minimize the artificial noises and ensure numerically stable solutions. Adjusting the artificial viscous force to be one to two orders less than the pressure force to prevent alterations in the physical dynamics of the microcavitation. As a result, eq. 18 includes the adopted stress tensor of bio-tissue in elastic solid phase, where μ_{art} , is the artificial viscosity.

$$\sigma_{ik,elastic} \approx -P\delta_{ik} + \frac{E}{1+\nu}\varepsilon_{ik} + \underbrace{\mu_{art}(V_{i,k} + V_{k,i})}_{artificial\ viscous\ term} \tag{18}$$

When the bio-tissue is in liquid or vapor phases, assumption of Newtonian fluid (when the material is highly incompressible) is applied with the following stress tensor expression. (eq. 19)

$$\sigma_{ik,\,fluid} \approx -P\delta_{ik} + \mu(V_{i,k} + V_{k,i}) + \underbrace{\mu_{art}(V_{i,k} + V_{k,i})}_{artificial\ viscous\ term} \tag{19}$$

with μ the dynamic viscosity of the bio-tissue. When the bio-tissue is in a liquid or vapor phase, an artificial viscous force term is included in order to improve the numerical stability.

2.4.3 Energy Conservation

The local energy conversation in the bio-tissue expressed in eq. 20 as

$$\frac{\partial e}{\partial t} + (\vec{V} \cdot \nabla)e \approx \nabla \cdot (\boldsymbol{\kappa} \nabla T) + Q_r \tag{20}$$

where $\boldsymbol{\kappa}$ is the thermal conductivity of the bio-tissue, and Q_r referring to the heat generation rate due to laser light absorption and the associated Joule heating. Local energy is determined from wave optics by solving a flat-top laser light propagating through a lens, and then focused at a specified location inside the bio-tissue with time harmonic Maxwell's equations as

$$\nabla \cdot \vec{D} = 0\,;\ \nabla \cdot \vec{B} = 0\,;\ \nabla \times \vec{E} = -j\omega\mu_o\vec{H}\,;\ \nabla \times \vec{H} = j\omega\varepsilon_r\varepsilon_o\vec{E} \tag{21}$$

with ω the laser frequency; $\vec{E}, \vec{L}, \vec{B}$, and $\vec{H}$ the electric field, electric displacement, magnetic induction and field in the frequency domains; $\varepsilon_{\mathrm{r}}$the relative permittivity of the bio-tissue; $\varepsilon_o$is the permittivity of free space; $\mu_o$is the permeability of the bio-tissue. The induced current density in the frequency domain is $\vec{J} = j\omega\vec{D}$. The time average joule heating Φ per unit volume is $\Phi = \frac{\mathbf{1}}{\mathbf{2}}\boldsymbol{Re}(-\boldsymbol{j}\omega E \cdot D)$. The heat generation rate Q_r is equal to Φ during the laser pulse and is zero after the laser pulse.

2.5 Heat Generation Term

In order to calculate the heated generation term, a separate model was created based on joule heating. Figure 2b shows the simulation domain and the obtained spatial distribution of joule heating Φ under time harmonic condition. The incident flat-top beam had a diameter of 200 μm with a wavelength (λ) of 4 μm. The hemispherical lens had a diameter of 300 μm with a refractive index of 2.5. The numerical aperture of the focal beam was ~0.9. The focal position was ~80 μm beneath the surface of the tissue, which is a common location during a LASIK surgery. The focal spot was ~4 μm in diameter. The refractive index of the tissue domain is 1.37 with an absorption coefficient of ~8759 m-1. Using a long wavelength with a large absorption coefficient provides thermal microcavitation without Avalanche breakdown in the bio-tissue. Furthermore, a body of resolution was used in order to reduce the original 3D simulation to a quasi-2D simulation.

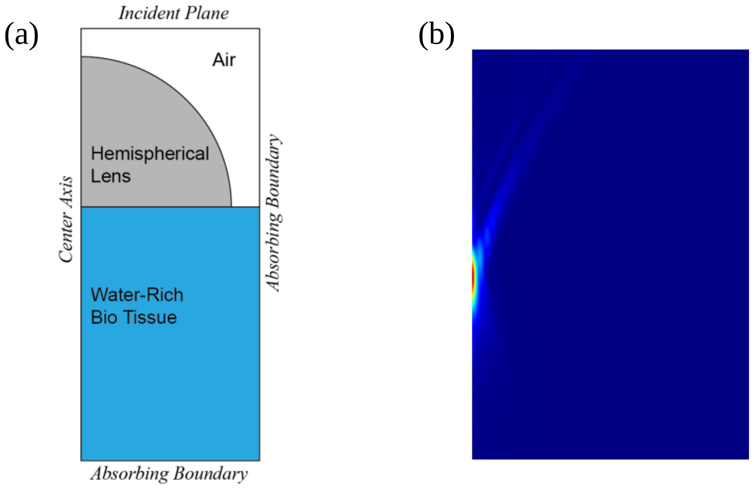

Figure 1: (a) Simulation domain for the plane wave propagation through a hemispherical lens and then focus inside the bio-tissue. (b) Spatial distribution of joule heating inside the bio-tissue. A rainbow color scale is applied to illustrate the relative intensity value. The domain size of the joule-heating plot is 100 μm x 150 μm.

2.6 Numerical Model Results and Analysis

With the above theoretical model, we directly simulate a micro-cavitation process induced by a 10 ns, λ=4 μm laser pulse focused at ~80 μm beneath the surface of the tissue with elastic modulus ~60 kPa and Poisson ratio = 0.4995 (i.e., highly incompressible tissue which is true for water-rich tissues). The distribution of laser-induced joule heating inside the tissue is the same as that in Figure 1b. A 0.02 mJ laser energy was delivered from the incident plane of Figure 1a in order to raise the tissue temperature and create a strong thermal microcavitation event. Since the dynamic process inside the bio-tissue is axi-symmetric, a quasi-2D simulation was adopted to solve the micro-cavitation processes. The width and height of the quasi-2D simulation domain were 100 μm and 200 μm, respectively. The initial temperature of the bio-tissue was 293.15K, and the outer boundaries of the simulation domain were fixed at 293.15K during the simulation. The top surface boundary was not fixed, and maintained at 1 atm. The movement of the top surface was determined from the velocity of the boundary determined with an arbitrary Lagrangian Euler (ALE) scheme. The obtained simulation results are listed in Figure 2.

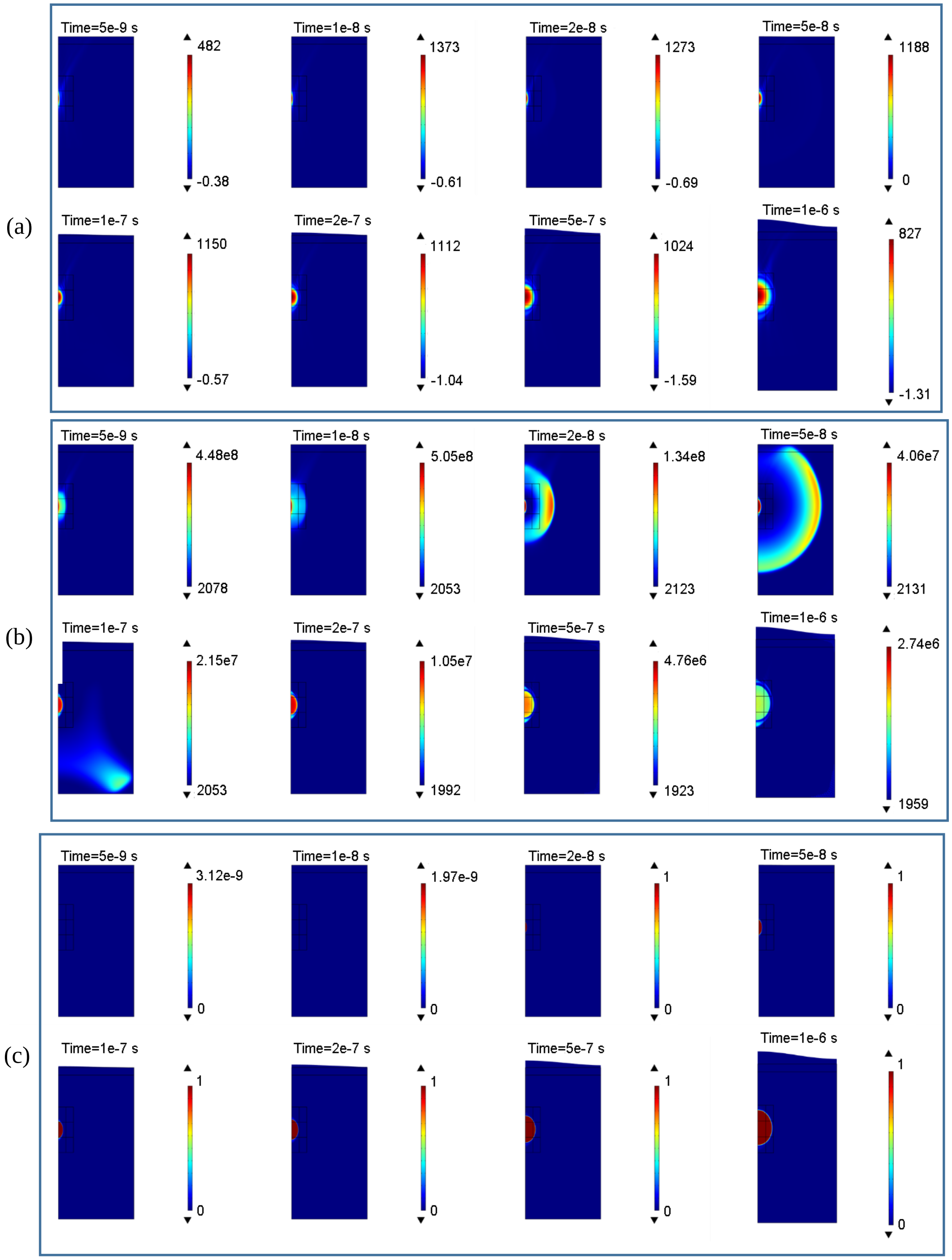

Figure 2: (a) Temperature increment (on top of 293.15 K with unit of Kelvin) inside the bio-tissue at different delay time from the beginning of the 10 ns laser pulse. (b) Pressure distribution (with unit of Pa) inside the bio-tissue at different delay time. (c) Vapor quality inside the bio-tissue at different delay time. "1" means pure vapor phase.

As illustrated in the temperature plots of Figure 2a, the tissue temperature increases monotonically during the 10 ns laser pulse. However, the temperature increment is not exactly linear with respect to time due to the varying specific heat as a function of temperature and specific volume. The tissue cools down after the laser pulse with a speed much slower than the heating. The heat-affected zone also increases monotonically with respect to the delay time. The radius of the heat-affected zone is ~25 μm at 1 μs from the beginning of the laser pulse. High pressure occurs around the focal spot during the laser pulse due to the rapid heating of the bio-tissue as illustrated in Figure 2b. The maximum pressure is ~5e^8 Pa at the end of the laser pulse, which is within the failure limit of most water-rich bio-tissue (>GPa). The thermally induced high pressure around the laser pulse causes a pressure wave propagating from the laser spot to the surrounding area, seen in the pressure plots from ~10 ns to ~100 ns from the beginning of the laser pulse. The pressure front is nearly spherical. The pressure wave leaves the right boundary at t ~ 60 ns, which correspond to an average speed >~1600 (m/s). This propagation speed is much higher than the sound speed in the bio-tissue, which is $\sqrt{E(1-\nu)/\rho/(1+\nu)/(1-2\nu)} \sim 282.75$ (m/s) when the tissue density is ~1000 (kg/m^3), and so the pressure wave can be considered a shockwave. Note that no shear wave was observed in the simulation, which indicates that the micro-cavitation dynamics is dominated by normal pressure. Note that compared with the temperature distribution, the pressure shows a uniform distribution at the heat affected zone. The uniform distribution attributed to the shockwave, which can even out the pressure gradient in the heat-affected zone.

Figure 2c shows the evolution of the vapor quality which is defined as the mass fraction of vapor inside the tissue during the micro-cavitation process. It is interesting to point out that the vapor bubble does not appear right after the end of the laser pulse when the maximum temperature occurs. Instead, the vapor bubble (i.e., red region in Figure 2c) was observed at ~16 ns from the beginning of the laser pulse, which is 6 ns after the end of the 10 ns laser pulse. This delay relates to the pressure wave propagation: the high temperature at the laser spot during the laser pulse does not convert the portion of tissue into a vapor bubble directly due to the accompanied high pressure around the laser spot. To trigger the vaporization process, an outgoing shockwave is required to release a portion of the high pressure around the laser pulse to the surrounding, and it takes a few ns for the shockwave to detach from the highly heated zone around the laser spot. The shape of the vapor bubble follows the joule heating profile in Figure 2b initially, and rapidly evolves into a larger more spherical bubble within 1 μs. The averaged expansion speed of the vapor bubble (defined as the radius increasing rate in this study) is <20 (m/s), which is much less than the sound speed in the bio-tissue. Another interesting phenomenon observed in the vapor quality plot is the thickness of the phase transition zone (where the quality number varies from zero to one), which is very thin compared with the diameter of the vapor bubble once the diameter of the vapor bubble is larger than a couple of microns. This observation indicates that previous micro-cavitation simulations treating vapor and condensed phases as two separated domains with different governing equations without considering their transition is valid as long the vapor bubble is more than a few microns in diameter.

2.7 Summary

In summary, a numerical model for laser-induced microcavitation based on fluid conservation equations. Additionally, a wave optics model is created to calculate the heat generation added to the sample. With the direct simulation, we can reproduce the laser-induced joule heating in bio-tissues based on linear light absorption, temperature increment and heat affected zone inside the tissue, phase change of the water-rich bio-tissues, vapor bubble generation and expansion, stress field formation and shockwave propagation, and the tissue swelling due to the presence of the vapor bubble when an ablation laser is set at mid-IR range. However it would be beneficial to verify these results with experimental imaging.

3 LASER MICROSCOPY IMAGING SETUP AND RESULTS[*]

3.1 Introduction

This section will provide the background for the laser microscopy imaging of early laser-induced microcavitation formation. Light matter interactions such as reflection, refraction, and absorption can be applied for different types of optical imaging. The resulting optical microscopy techniques including reflection microscopy, absorption microscopy, transmission microscopy, fluorescence microscopy, Raman microscopy and photoluminescence microscopy. When the light source is changed from broadband to narrow band (e.g., using laser), interference effects can also be applied in the optical imaging technique. For example, interference reflection microscopy (IRM) uses the interface pattern created from laser light that reflects off of a sample to study cell adhesion or cell mobility on a glass coverslip [36].

Many methods have been developed for imaging microcavitation with laser microscopy. In each method, sample can be either illuminated with continuous or pulsed lasers through an optical microscope. When a continuous laser is applied, high speed camera that triggered precisely can be applied to image the dynamic process during the microcavitation. One of the drawbacks of using continuous laser in microcavitation imaging is that the sample would be continuously absorbing laser energy during the entire imaging process. This photon energy could be converted to thermal or chemical energy in the sample, which could damage the sample and affect the microcavitation process to be observed. Compared with continuous laser, using pulsed laser would minimize energy absorption by the imaging sample. With sufficiently large gaps among

---

[*] Part of this chapter is reprinted with permission from “Direct numerical simulation of microcavitation processes in different bio environments” by Kevin Ly, Sy-bor Wen, Morgan s. Schmidt, and Robert J. Thomas, 2017. *Optical Interactions with Tissue and Cells Xxviii*, Vol. 100602, Copyright 2017 by SPIE.

pluses, sample damage due to cumulative laser energy absorption in the sample can be prevented.

Due with the semi-transparent nature of the sample before and during the microcavitation process, transmitted optical microscopy can be better combined with pulsed laser during the laser microscopy imaging of the dynamics of the microcavitation process. Transmitted microscopy imaging relies on transmitted light pass through a sample to create an image after the objective lens. Brightfield, darkfield, phase contrast and Differential Interference Contrast (DIC) are the most common transmitted microscopy methods applied in the bio study with semi-transparent samples [21]. Among these four methods, brightfield microcopy requires simpler optical alignment. An image in bright field microscopy is formed by variation of the light absorption inside the sample under a laser beam. Before reaching the sample, the illumination light typical goes through a condenser to deliver most of the light to the sample in the brightfield microscopy [26]. However, for highly transparent samples, brightfield imaging cannot resolve features of the sample, which might be the case in microcavitation bubbles as both the water and water vapor are highly transparent to the visible light. Therefore, for highly transparent samples, it can be beneficial to use another laser microscopy method to inspect the microcavitation process. Note that the reported microcavitation studies, to the best of our knowledge, are still based on brightfield microscopy due to its simpler optical alignments. Using a different microscopy imaging technique that does not rely on light absorption might uncover additional dynamics of microcavitation that haven’t been reported previously with laser brightfield microscopy.

Darkfield microscopy is one of the microscopy methods that can better resolve transparent samples. While brightfield microscopy images are based on spectral absorption, darkfield microscopy images is based on collection of light that is diffracted by the sample. In a darkfield microscopy, the illumination light enters the sample with a step oblique angle from all azimuthal directions. This step incoming angle of illumination is even larger than the numerical aperture of the objective lens [21]. Thus, incident beam without any diffraction cannot be collected by the objective lens. In other words, only the diffracted light from the sample can be collect as the image after the objective lens. When the sample size is large than the wavelength of the incoming light by 10 times or more, diffracted light does not scatter uniformly based on Mie scattering theory. Instead, most of the diffracted light propagates in the direction of the incident light as shown in Figure 3. Thus, the intensity of the diffracted light in other directions has very low intensity[37].

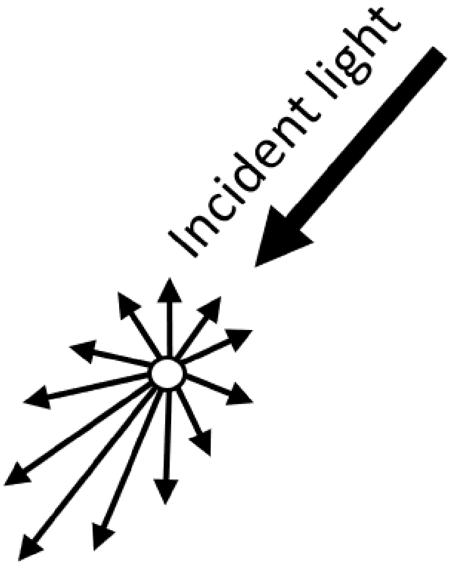

Figure 3: Mie scattering diagram where sample is greater than 10 times the wavelength. Image adapted from: Bhattacharjee 2016. [37].

Therefore, the intensity of the illumination light that can be collected the objective lens in darkfield microscopy is merely a very small fraction of the incident light intensity. To have enough brightness in darkfield microscopy, much higher illumination intensity is required compared with brightfield microscopy [30]. The higher illumination intensity may cause damage of the sample especially when pulsed laser light is applied as the illumination source.

Phase contrast microscopy is another microscopy method that also images the sample based on diffracted light. Different from darkfield imaging, phase contract imaging collects both diffracted and undiffracted light that pass through a sample. The resulting image is a combination of both light types with a phase plate. The resulting inference patterns in phase contrast imaging represent features of the probed sample. Phase contrast microscopy was invented by Zernike in 1930s, which earned him a Noble price in 1953. Zernike phase contrast microscopy uses a π/4 phase plate to shift the phase of undiffracted light. In addition, a gray filter is applied to reduce the light intensity of the undiffracted light. The net effect will be that the light intensity of undiffracted light is reduced to a level that is comparable with the light intensity of diffracted light from the probed sample. Therefore, the features of the sample carried in the diffracted light is not buried by the undiffracted light in the phase contrast microscopy. The usage of π/4 phase plate is to improve the interference between the diffracted and undiffracted light so that sample feature are more visible in the resulting image [29].

Differential interference contrast microscopy (DIC) is a variation of phase contrast microscopy that uses two different polarized light to form images. By comparison of the level of diffraction (including the phase shift) of two different polarized lights through a Normarski prism after passing through the sample, the gradient of the optical path inside the sample can be revealed. Note that the optical path variation inside the sample can be due to either the change of refractive index (i.e., features) and/or the thickness of the sample [30]. As the light is polarized before entering the Normarski prisms, the original polarization of the illumination light gets cancelled out by another polarizer called the analyzer [30].

In DIC microscopy, semi-coherent light is polarized before entering the Normarski Prism. The prism splits the light into two beams that are polarized orthogonally to each other. The beams are directed to the sample though a condenser, where their optical paths with change. An objective lens then focuses the polarized beams to another Normarski prism that combines the beams again. Any light that retains the original polarization is polarized by the analyzer to eliminate any effect the first polarization would have on the final image. Compared with phase contrast imaging, DIC imaging can better provide a quantitative estimation of the refractive index or the thickness of the probed sample [38]. Due to the usage of Wollaston prisms to split and combine lights with different polarizations, DIC microscopy can be expensive and complicated in terms of optical alignment compared with phase contrast microscopy and will not be used in this study.

To validate the experimental results of laser-induced microcavitation with the ns pulsed laser PS microscopy, a corresponding ns pulsed laser brightfield imaging is also constructed in this study. Through comparison of brightfield and phase-contrast results, we can better justify the features observed in laser PS imaging as well as the benefits of using laser PS imaging compared with laser brightfield imaging. Details of the initial version setup are described in section 3.2. The setup will image the microcavitation in both distilled water and 10% Polyacrylamide gel in water solution (10% PAA gel), with the results detailed in section 3.3. Details of the final version setup are described in section 3.4. . The setup will image the microcavitation in both distilled water and 10% PAA gel, with the results detailed in section 3.3. Distilled water and 10% PAA gel are used as they have similar properties to tissues like the cornea, which are common targets for laser microscopy [15].

3.2 Initial Version Microscopy Setup

Microcavitation process was initially recorded with a brightfield microscopy setup as a reference for the final version microscopy setup developed in this study. Illumination of the brightfield microscopy was an incoherent ns light source. The incoherent light source is generated with a pulsed Neodymium-doped Yttrium Aluminum Garnet (Nd:YAG) ns laser at 532 nm wavelength with a shutter that gives a time resolution of 4 ns. To reduce the coherence of the light from the ns laser, the laser light is delivered to a dye cell before sending to the brightfield microscope for ns time resolved imaging. The dye cell absorbs the incoming laser photons and re-emitted light around 620 nm wavelength through laser-induced fluorescence. The emitted light does not follow a uniform direction and thus has reduced temporal coherence compared to the 532 nm laser. To induce microcavitation, a second 10 ns Nd:YAG laser running at 1064 nm wavelength is focused on the sample. Figure 4 shows the resulting laser brightfield microscopy configuration for imaging microcavitation process induced by a 1064 nm ns laser.

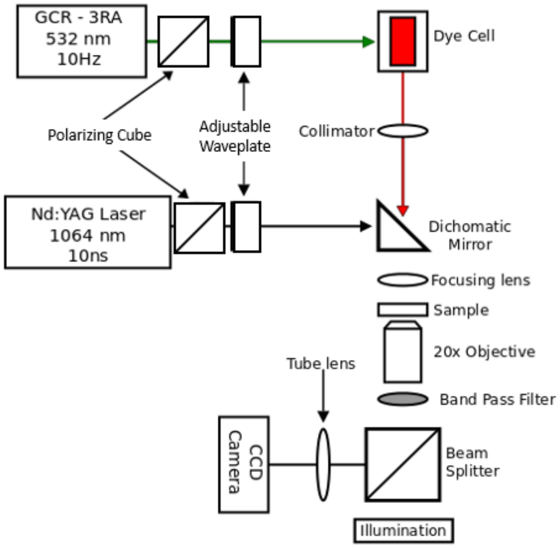

Figure 4: Schematic of brightfield experimental setup.

In Figure 4, the 532 laser passes through an optical isolator to reduce the laser energy coming from both lasers and to prevent unwanted feedback from damaging the laser. An optical isolator is composed of a polarizing cube beamsplitter and a ¼ λ waveplate. The polarizing cube beamsplitter will polarize the laser beam passing through, typically to a p polarization. P polarization light is polarized parallel to the incident plane, while s polarization is polarized perpendicular to the plane. The polarized beam then passes through the ¼ λ waveplate, which will change the polarizing to a circular polarization. The waveplate is able to change the polarization through retarding one component of the polarization to its orthogonal part. If the beam passes back though the waveplate from the other side, the waveplate will change the circular polarization to S-polarization. The polarized beamsplitter should reflect this polarization, typically to a beam dump, and protect the laser from reflected laser light. After passing though the optical isolator, the 532 nm laser light then passes through a dye cell to reduce the laser coherence. As the 532 nm laser light diverges after passing though the dye cell, a collimator is used to collimate the light before the light reaches the dichromatic mirror. The 1064 nm laser is also directed to the dichromatic mirror after passing through a separate optical isolator. The dichromatic mirror aligns the 532 nm laser and the 1064 nm laser by passing the 532 nm laser through and reflecting the 1064 nm laser. The 1064 nm laser is focused on the sample to initiate cavitation by a focusing lens. The 532 laser will also be slightly focused by the same focusing lens, but will remain incoherent. After both the probe and ablation beams pass though the sample, a 20X objective collect the ~620 nm illumination light and forms an image of the vapor bubble and shockwaves. To reduce plasma emission light to be captured in the image, a 550 nm to 650 nm band pass filter is placed in front the camera. To prevent the ablation 1064 nm laser beam from damaging the camera and the objective lens, an additional IR filter is inserted in front of the objective lens.

3.3 Final Version Microscopy Setup

In order to adapt the initial version microscopy setup to the final version microscopy setup, a better understanding of positive phase contrast (PS) microscopy is required. A diagram of a positive PS configuration is given in Figure 5 [39].

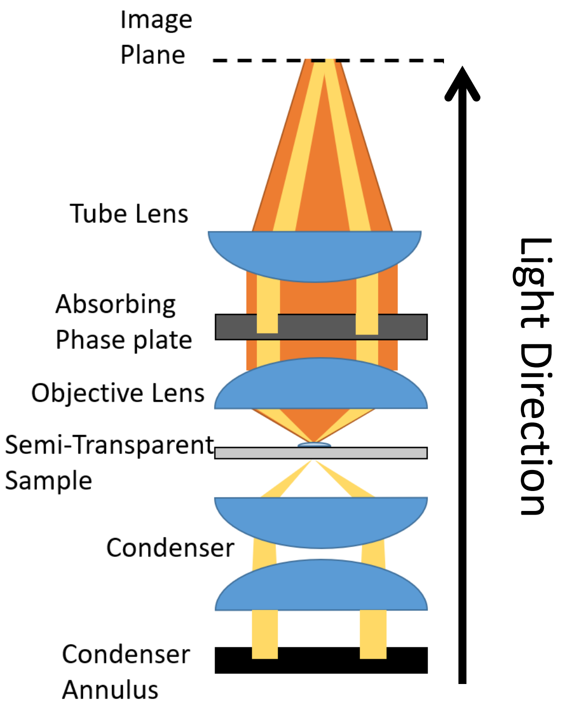

Figure 5: A configuration of positive PS. Yellow is undiffracted light and orange is diffracted light.

In a positive PS configuration, partially coherent light is focused onto a sample (specimen) by a condenser. The condenser contains an annulus to manipulate the light beam so that its cross section has a ring shape. As the light pass through the sample, some of the light will diffract through interacting with the sample. The interaction will alter the direction of the diffracted light, and have most of the light waves spread outside the ring cross section. Light that does not interact with the sample is considered the undiffracted (surround) light and will continue to have a ring-like cross section. Both the diffracted and undiffracted light are collected by the objective.

The objective will pass both the diffracted and undiffracted light through the phase plate and orient both light beams to form an interference pattern on the image plane. Interference is possible due to the diffracted and undiffracted light being partial incoherent. The phase plate contains a circular region that matches the cross section of the undiffracted light. The region both reduces the intensity and changes the phase of whatever light pass through the circular region. While the region is designed to only alter the undiffracted light, some of the diffracted light may pass through it, creating optical artifacts that might appear in positive PS microscopy images.

There are two main optical artifacts that might appear in positive PS microscopy images. One optical artifact is the halo effect, where there is a brighter region surrounding the edges of the sample that is imaged. These regions are typically very thin, which gives the appearance of halos. The halo regions are due to some of the diffracted light passing through the phase shifted part of the phase plate, and thus get shifted along with the surrounding light. This will reduce destructive interference between the surrounding light and the edge diffracted light, which creates the brighter halo regions. The other optical artifact is the shade off effect. The shade off effect is where areas of the sample with uniform diffraction are imaged lighter in the center and darker at the edges. This effect is due to the diffracted light from the center of the specimen possibly having a marginal spatial deviation compared with the surround light and thus can get phase shifted [29]. The phase shifted diffracted light will have reduced destructive interference with the surround light, and will form a lighter region in the image similar to the halo effect. Despite the optical artifacts, PS microscopy can provide images that show details of transparent sample that cannot be well handled in brightfield imaging.

To incorporate ns laser light with the PS microscopy, standard PS microscopy setup is modified to include a pump-probe system using Nd:YAG lasers. The modified setup is illustrated in Figure 6.

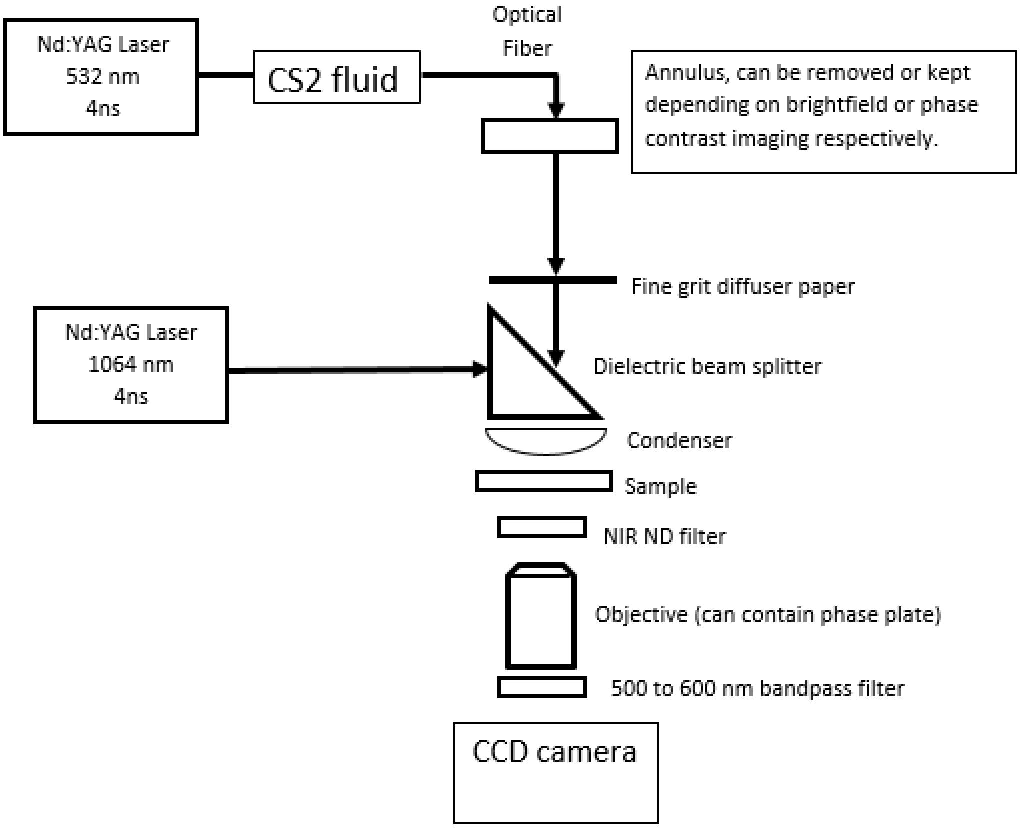

Figure 6: Schematic of final experimental setup.

In Figure 6, illumination is done by a Nd:YAG laser running at 532 nm with a time resolution of 4 ns. To destroy the coherence, the laser light passes through a tube of carbon disulfide (CS_2) fluid and a 105 μm core multimode fiber. As the light passes through the CS_2 fluid, the refractive index of the fluid slightly changes due to its large Kerr coefficient. This change in the refractive index can also shift the wavelength of part of the laser light in a process called band broadening [40]. The slightly band broadened beam then passes through the long optical fiber which provides enough Raman gain [41]. As the laser light propagates thought the fiber with enough

Raman gain, a chain of stimulated Raman scattering occurs which further increases the wavelength of the incident laser beam especially at the wavelengths with strong Raman gain resonance of the optical fiber [42]. In order to see if Raman scattering occurs, the emission spectrum of light after passing through the 105 µm core multimode fiber was created (Figure 7).

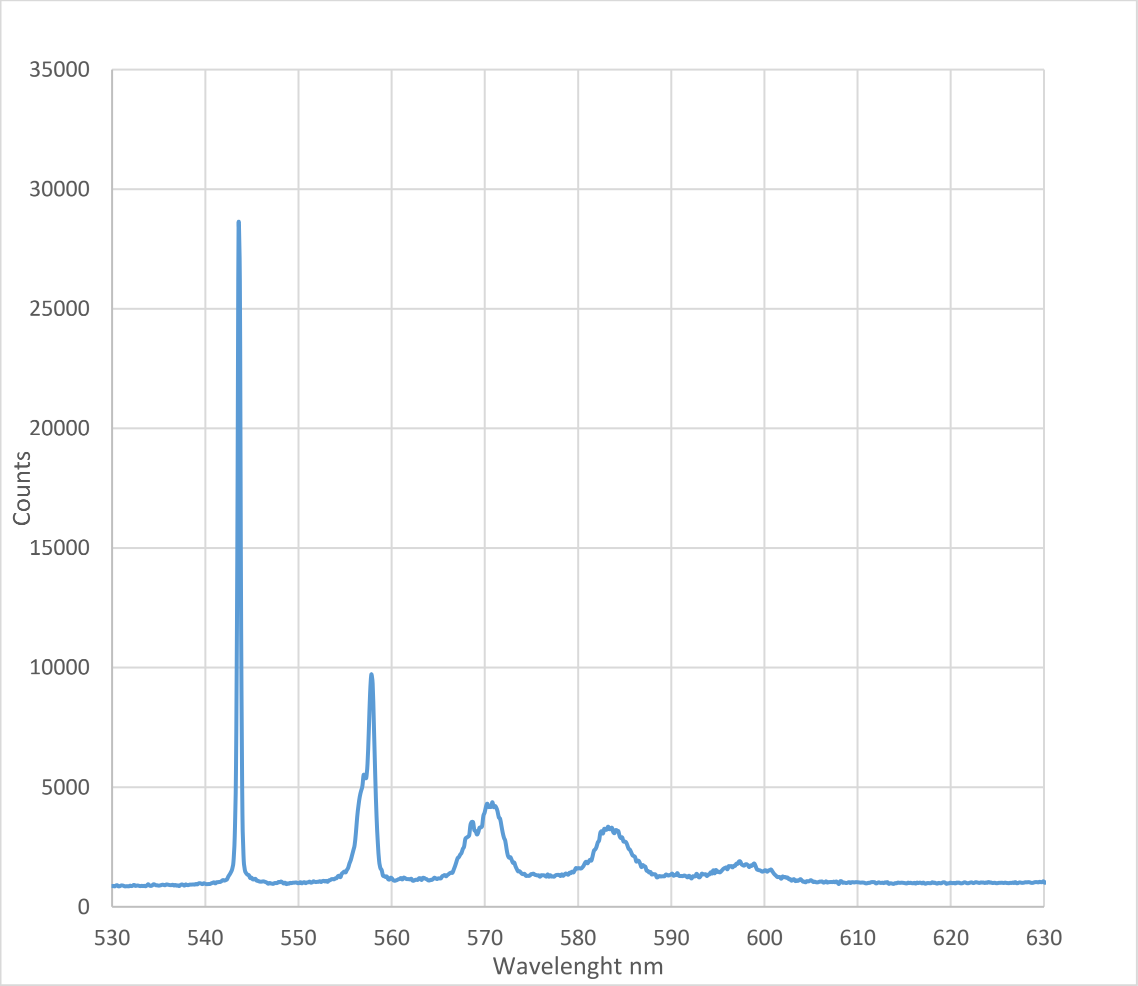

Figure 7: Emission spectrum of light emitted from the end of the long optical fiber bundle.

Figure 7 illustrates that the highest intensity wavelength of the laser light is ~545 nm. All other wavelengths have lower intensities, with the intensity inversely related to the wavelength of the laser light. Note that the bandpass filter before the camera would cut out any light with wavelengths outside of the 500 to 600 nm range.

The incoherent laser light is then passes through the annulus to a dielectric beam splitter. A second pulsed Nd:YAG laser running at 1064 nm wavelength with time resolution of 4 ns is also directed to the beam splitter. Note that polarizers are not used in this setup as the pulse energy of both the 532 nm and the 1064 nm lasers are control internal by their laser systems. The beam splitter aligns the two lasers by passing the 532 nm laser reflecting the 1064 nm laser at a 90 degree angle. The condenser lens is used to focus the 1064 nm laser on the sample and align the 542 laser for phase contrast. An NIR filter is placed between the sample and a 10x objective to protect the objective from residual 1064 laser light. This 10x objective collects the 532 laser light and passes the light through a phase plate in the objective housing. A 500 to 600 nm band pass filter is placed after the objective to reduce plasma light from optical breakdown. The image formed by the objective and phase plate is transported to the camera via optics in the microscope. Note that the annulus and objective can be altered for a brightfield configuration. In brightfield configuration, the annulus is removed and the objective with the phase plate is switched with an objective that does not have the phase plate.

3.4 Initial Version Microscopy Results

Samples studied with the initial version microscopy setup for laser-induced microcavitation are deionized water and 10% Polyacrylamide gel in water solution (10% PAA gel). The pulse energies delivered to deionized water and 10% PAA gel samples are tested are ~8 mJ respectively. A minimum of three images were collected every 10 ns for the first 200 second of the cavitation process due to the position of the cavitation bubble being unstable. The instability is due to the ablation point varying slightly due to the nature of starting position of plasma formation initiating on lucky electrons around the laser spot. Images collected within the first 20 ns were discarded as the bright light in the center of the images obscured any details of the cavitation process. Figure 8 illustrates a time evolution of the microcavitation process in distilled water. The 20 ns frame is kept to illustrate the bright light. The time between frames are 10 ns for the first 100 ns, then 100 ns for the 200 ns frame. Figure 8 illustrates a time evolution of the microcavitation process in 10% PAA gel. The time between frames are 10 ns for the first 200 ns.

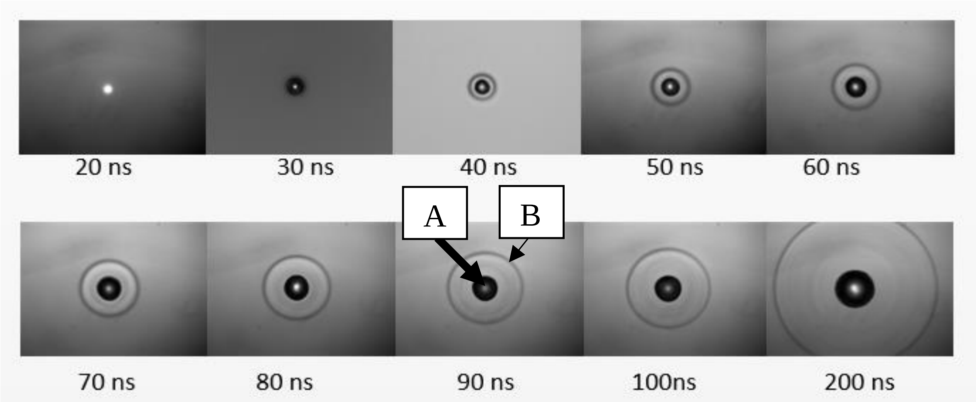

Figure 8a: Time evolution of laser-induced microcavitation initiated in distilled water. The pulse energy delivered to the sample by the pump beam is around 8 mJ.

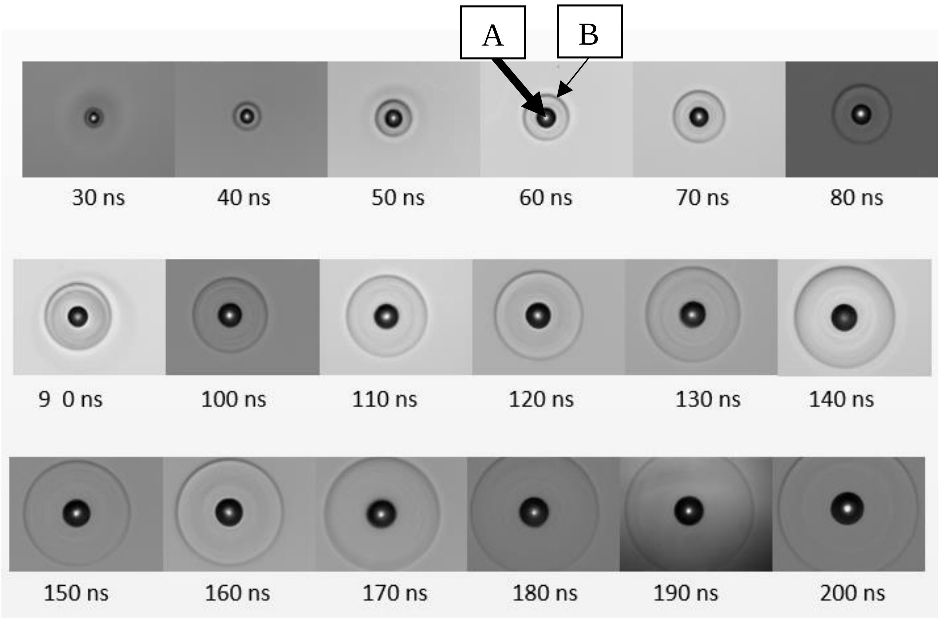

Figure 8b: Time evolution of laser-induced microcavitation initiated in 10% PAA gel. The pulse energy delivered to the sample by the pump beam is around 8 mJ.

As illustrated in Figures 8a and 8b, we can observe the laser-induced shockwave as the light ring (labeled B) and cavitation bubble as the dark circle with the bright center (labeled A). The bright center is due to plasma light emitted due to plasma formation. The shockwave show seems to expand rapidly over time. The expansion of the vapor bubble, however, has a much slower speed in both water and 10% PAA gel. The vapor bubble and shockwave are not always present at the center of the images in Figure 8b, which is probably due to the 10% PAA gel sample not being completely even at all locations. Slight changes in the 10% PAA gel sample will alter the refraction angle of the incoming 1064 nm light beam. Additionally, the PAA gel may also have impurities that may start the cavitation process early. In both Figures 8a and 8b, the vapor bubble shows also appears to become more spherical over time. Detailed discussion of the velocity of the observed laser-induced shockwave and expansion speed of the cavitation bubble are in chapter 5.

3.5 Final Version Microscopy Results

Samples studied with the final version microscopy setup for laser-induced microcavitation are deionized water and 10% Polyacrylamide gel in water solution (10% PAA gel). Note that the instability of the plasma formation is more significant in the final version setup compared with the initial version setup. Thus more trials were needed to obtain the desired brightfield and phase contrast images.

3.5.1 Phase Contrast (PS) vs Brightfield (BF) in Distilled water

The pulse energies delivered to deionized water samples are tested is ~8 mJ with .2 mJ variability. The pulse energy was selected based in order to have consistent cavitation at around the same focal point. Cavitation can occur at lower energies, however cavitation becomes very inconsistent due to reduced pulse energy stability and the nature of avalanche breakdown. Brightfield (BF) and phase contrast (PS) images were taken every 10 ns for the first 200 ns of the microcavitation process, then every 100 ns until 1 μs, then every 1 μs until 10 μs. A minimum of three trials were taken at the same delay time between the pump and probe lasers due to the position of the cavitation bubble being unstable. Images collected within the first 20 ns were discarded as the bright light in the center of the images obscured any details of the cavitation process. Figures 9a and 9b illustrate the time evolution from 30 to 200 ns of the microcavitation process in BF and PS microscopy respectively. The time between frames is 10 ns. Figures 10a and 10b illiterate the time evolution from 100 to 200 ns of the microcavitation process in BF and PS microscopy respectively. The time between frames is 100 ns. Figures 11a and 11b illiterate the time evolution from 1 to 10 μs of the microcavitation process in brightfield (BF) and phase contrast (PS) respectively. The time between frames is 1 μs.

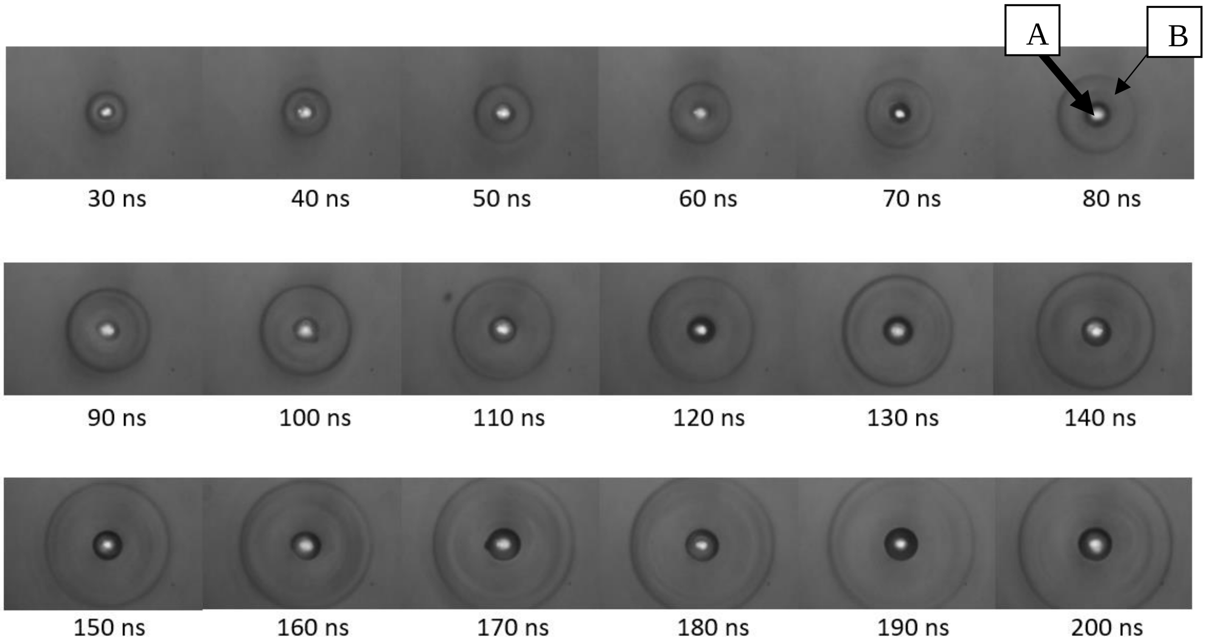

Figure 9a: Time lapsed early BF images with 10 ns between frames for laser-induced microcavitation in distilled water. The pulse energy delivered to the sample by the pump beam is around 8 mJ.

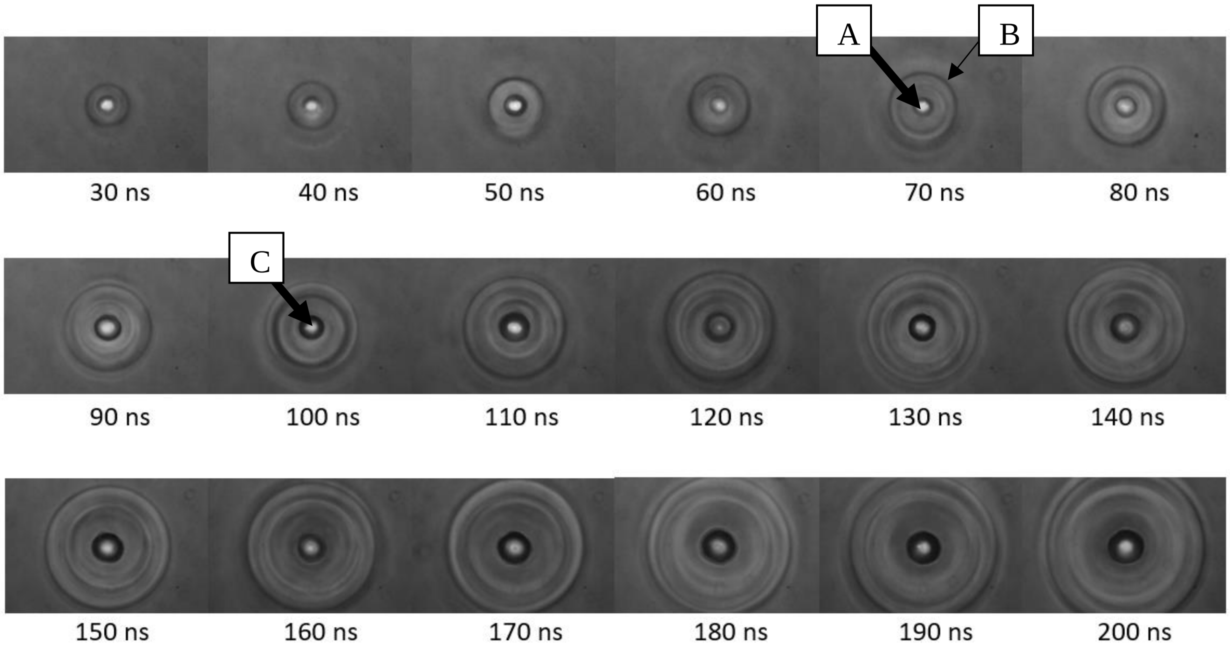

Figure 9b: Time lapsed early PS images with 10 ns between frames for laser-induced microcavitation in distilled water. The pulse energy delivered to the sample by the pump beam is around 8 mJ.

As illustrated in Figures 9a and 9b, we can observe the laser-induced shockwave as the light ring (labeled B) and cavitation bubble as the dark circle with the bright center (labeled A). The bright center is due to plasma light emitted from the avalanche breakdown process. Additional bright and dark periodic interference patterns appear between the bubble and shockwave in the phase contrast images of Figure 9b. A detailed discussion of the bright and dark periodic interference patterns is in chapter 5. The size of the vapor bubble and shockwave appears to match between the phase contrast and brightfield microscopy. Additionally in Figure 9b, there appears to be a bright ring (labeled C) surrounding the bubble. This light ring is likely due to the halo effect, an artifact of phase contrast microscopy (c.f. 3.3 section). Detailed discussion of the size of the observed laser-induced shockwave and expansion speed of the cavitation bubble are also in chapter 5.

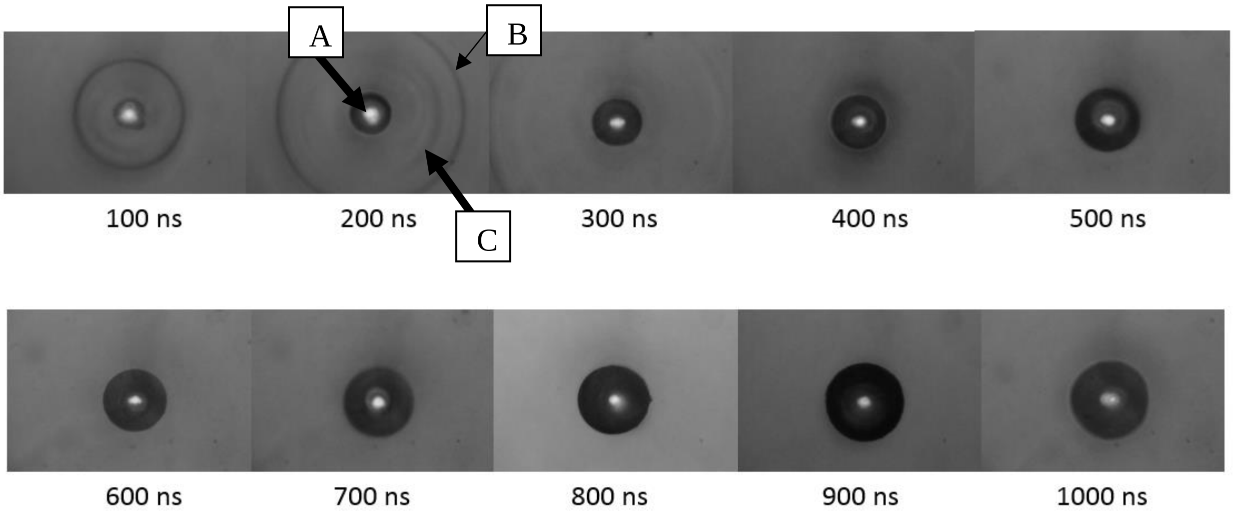

Figure 10a: Time lapsed BF images with 100 ns between frames for laser-induced microcavitation in distilled water. The pulse energy delivered to the sample by the pump beam is around 8 mJ.

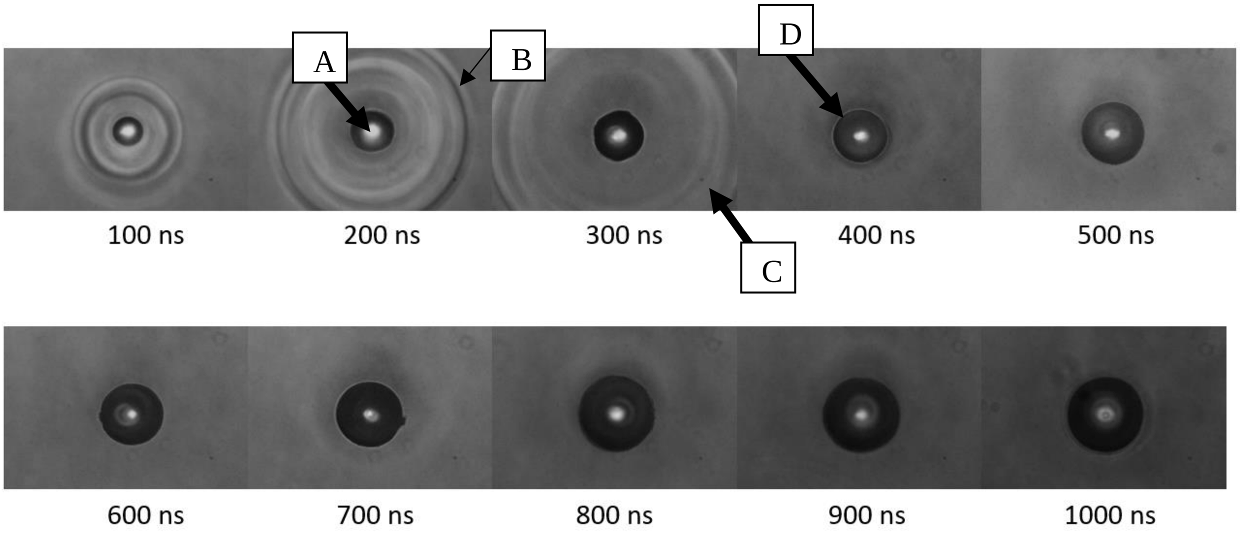

Figure 10b: Time lapsed phase contrast images with 100 ns between frames for laser-induced microcavitation in distilled water. The pulse energy delivered to the sample by the pump beam is around 8 mJ.

As illustrated in Figures 10a and 10b, the bubble appears to become more spherical over time. The bright and dark periodic interference patterns (labeled C) between the shockwave (labeled B) and the bubble (labeled A) in Figure 10b disappear between 300 and 400 ns delay times. However at the 300 ns frame, the patterns appear only near the shockwave and not the bubble. The proximate of the pattern to the shockwave would indicated that the bright and dark periodic interference patterns are possibly tied to shockwave rather than the bubble. The bright ring (labeled D) surrounding the bubble that appears in phase contrast images of Figure 9b persist in Figure 10b. This light ring is likely due to the halo effect, an artifact of phase contrast microscopy (c.f. 3.3 section). Detailed discussion of the size of the observed laser-induced shockwave is in chapter 5.

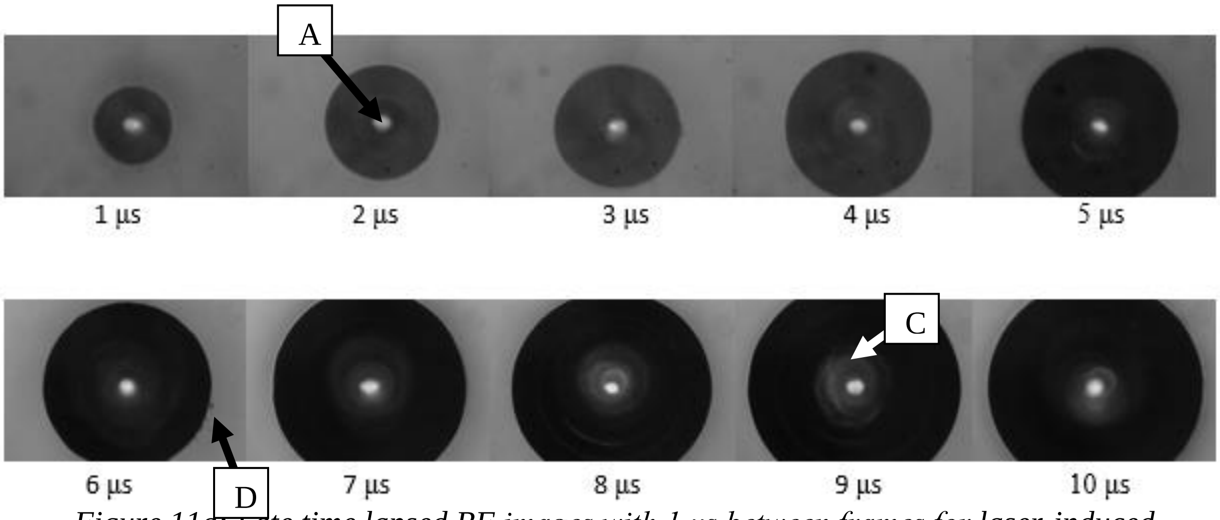

Figure 11a: Late time lapsed BF images with 1 µs between frames for laser-induced microcavitation in distilled water. The pulse energy delivered to the sample by the pump beam is around ~8 mJ.

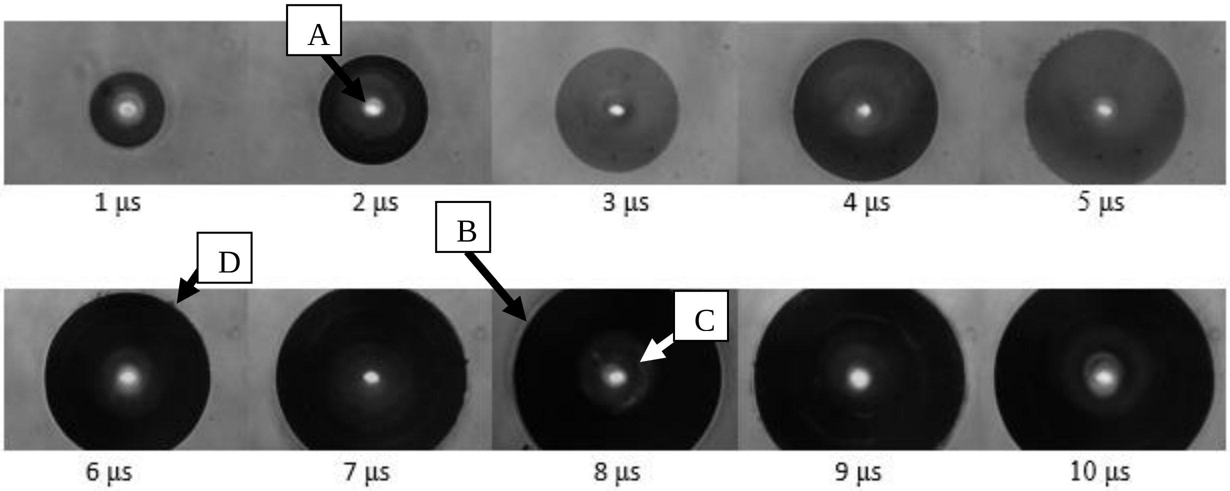

Figure 11b: Late time lapsed PS images with 1 µs between frames for laser-induced microcavitation in distilled water. The pulse energy delivered to the sample by the pump beam is ~8 mJ.

As illustrated in Figures 11a and 11b, the bubble with center (labeled A) remain spherical over time. In Figure 15, there appears to be a bright ring (labeled B) surrounding the bubble. This bright ring is apparent in all focused phase contrast images. This light ring is likely due to the halo effect, an artifact of phase contrast microscopy (c.f. 3.3 section). The bright ring (labeled B) surrounding the bubble that appears in phase contrast images of Figure 10b persist in Figure 11b.

Additionally there appears to be additional brighter regions around the center of the bubble (labeled C) in the frames after 7 μs of Figures 11a and 11b. Further discussion of these bright regions are in Chapter 5.

3.5.2 Phase Contrast (PS) vs Brightfield in 10% Polyacrylamide Gel (10% PAA Gel)

The pulse energy delivered to 10% Polyacrylamide gel (10% PAA gel) is about 2.1 mJ. The reduced pulse energy was selected as impurities in the 10% PAA gel induces microcavitation prematurely in the final version microscopy setup. Brightfield (BF) and phase contrast (PS) images were taken every 10 ns from 30ns to 50 ns, then every 20 ns until 100 ns, then every 50 ns until 200 ns. Fewer images were taken due to indications from the first version setup that the bubble expansion and shockwave speed of 10% PAA gel. Figures 12a and 12b illiterate the time evolution from 30 to 200 ns of the microcavitation process in BF and PS respectively. Time between frames is 10 ns from 30ns to 50 ns, then every 20 ns until 100 ns, then every 50 ns until 200 ns.

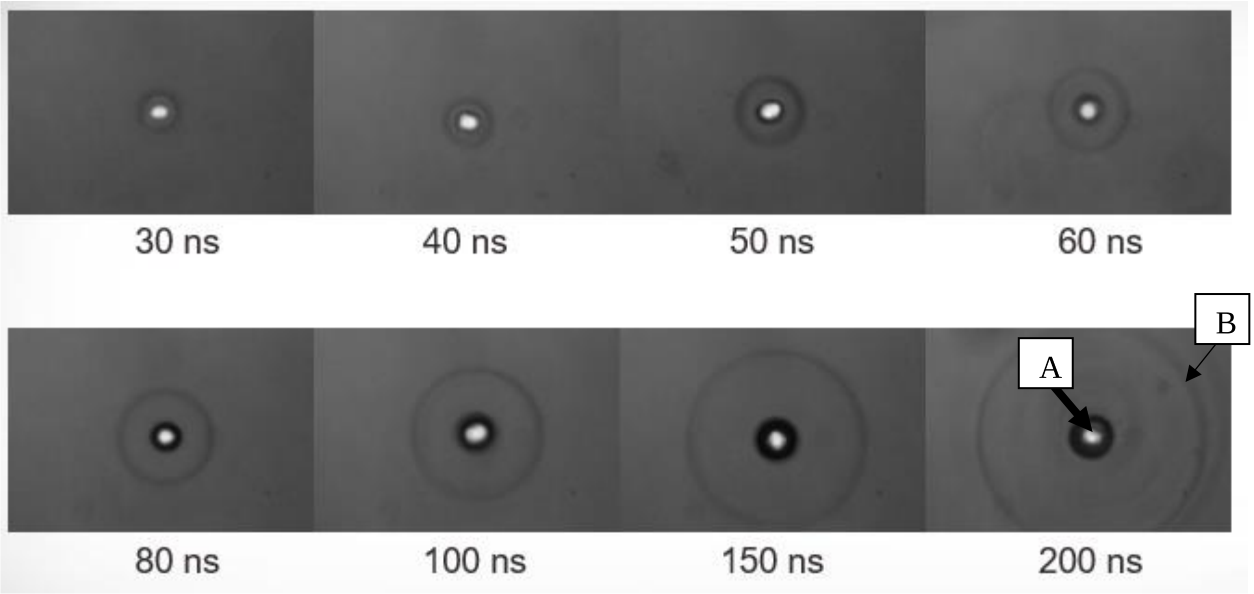

Figure 12a: Time lapsed BF images for laser-induced microcavitation in 10% PAA gel. The pulse energy delivered to the sample by the pump beam is ~2 mJ.

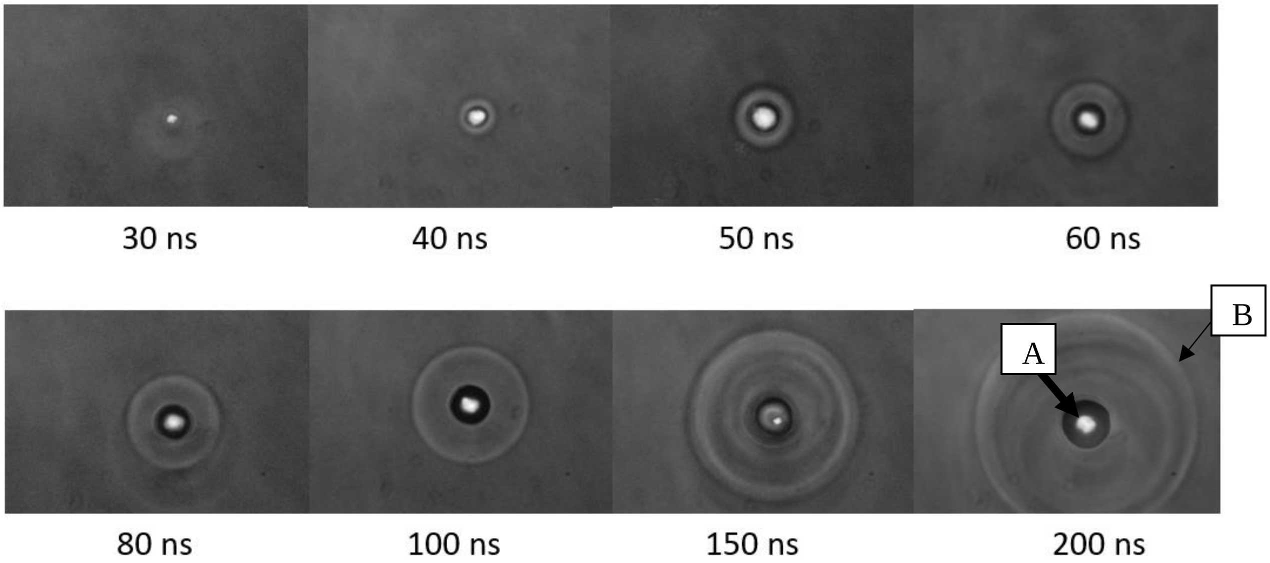

Figure 12b: Time lapsed PS images for laser-induced microcavitation in 10% PAA gel. The pulse energy delivered to the sample by the pump beam is ~2 mJ.

As illustrated in Figures 12a and 12b, the features of the shockwave (labeled B) and vapor bubble (labeled A) are present. The vapor bubble and shockwave are not always present at the center of the images, which is probably due to the 10% PAA gel sample not being completely flat at all locations. Slight changes in the 10% PAA gel sample will alter the refraction angle of the incoming 1064 nm light beam. The refracted light passing though the 10% PAA gel sample thus collects at a slightly shifted focal spot and subsequent initiation point of the vapor bubble and shockwave. For both Figures 12a and 12b, the bubble is not a spherical as it is in their respective brightfield water images. The reason for the bubble not being as spherical is due to the non-uniformity of the 10%PAA material affecting the bubble growth. Additionally in Figure 13b, the light and dark periodic patterns between the shockwave and bubble appear later compared to the water cavitation images. The delay may be due to the lower energy of the laser pulse or the PAA altering the imaging.

3.6 Summary

In summary, time lapsed images were collected using both brightfield (BF) and phase contrast (PS) configurations of a pump-probe system for the lasers. The samples tested are distilled water and 10% Polyacrylamide gel in water solution (10% PAA gel). Laser pulse energies of ~8 and ~2 mJ were focused on the distilled water and 10% PAA gel samples respectively to initiate the cavitation event. Both the shockwave and cavitation bubble can be observed in BF and PS microscopy. However, the PS images contain additional features, particular in the area between shockwave and cavitation bubble.

4 IMAGING BACKGROUND

4.1 Introduction

This section will provide the imaging background required to analyze the brightfield (BF) and phase contrast (PS) images. Explanations for the imaging of the vapor bubble and shockwave is discussed in section 4.2. Background for interpreting phase contrast images, which is the core of the study is discussed in section 4.3.

4.2 Vapor Bubble and Shockwave Imaging

Vapor bubbles are formed when a portion of a solid or liquid absorbs enough energy to change into a high pressure gas/plasma. In a fluid, the resulting gas bubble can expand and displace the fluid until the pressure of gas is near equilibrium with the surrounding liquid. Due to the large difference between the refractive index of water vapor and water , the imaging light will diffract significantly at the bubble interface, typically leaving the image of the vapor bubble dark [43]. Shockwaves are exceptionally thin regions where fluid flow properties change quickly [44]. One of these shifts is pressure, which is a factor in determining the refractive index of the fluid. The high pressure region in the shockwave usually increases the refractive index significantly, so the imaging light can be diffracted at the front of the shockwave [45]. The diffracted light may not reach the objective, and so the image of the shockwave front has lower light amplitude and shows darker color.

4.3 Positive Phase Contrast (PS) Imaging

As stated in section 1.4, phase contrast (PS) images are composed from the inteference pattern of of the diffracted and undiffracted light. Optimal destructive interference occurs when the phase difference of the lights is 180 degrees. The phase shift of the diffracted light (δ) is calculated in eq. 22.

$$\delta = 2\pi\Delta/\lambda \qquad (22)$$

Where Δ is the optical path difference and λ is the wavelength of the incident light. The optical path difference is the product of the refractive index difference between the sample and the surroundings with the thickness of the sample the incident light is passing though. Under the assumption that (a) the diffracted light has negligible intensity compared to the undiffracted light and (b) the phase shift done by the sample is small enough to use small angle theory, the phase shift for the diffracted light from a transparent sample is calculated to be no more than 90 degrees based on wave optics[46]. As the undiffracted light is not phase shifted by the sample, the phase difference between the lights is just 90 degrees and leads to a suboptimal destructive interference image. To improve the interference image, PS microscopy has the diffracted and undiffracted lights pass through a phase plate prior to forming the interference pattern. As stated in section 3.3, the phase plate contains a circular region that matches the cross section of the undiffracted light. All light passing through the region is phase shifted 90 degrees forward (advance), so the undiffracted light can now have a phase difference of 180 with the diffracted light to provide a near optimal destructive interference for PS images. Additionally, the region will contain a grey filter to reduce the intensity of the undiffracted light. Without the grey filter, the higher intensity of the undiffracted light will obscure sample features by dominating the interference images. In order to properly interpret the intensity profile of interference images, we must understand in depth how the phase shift in the sample translates to the intensity of the interference. Under the assumptions that the objective collects all the undiffracted and diffracted light from the sample and that none of the diffracted/phase shifted light is altered by the phase plate, a phasor diagrams can be used to explain the formation of PS inteference images. Phasor diagrams are especially useful in interpreting the causes of brightness variations in PS images due to the phase shift of the sample. Figures 13a-e contain a phase diagram of the microscopy image under different sample and phase plate conditions. The figures also contain with a schematic of the microscopy setup for clarity. Figure 13a is under the condition that the sample is transparent and the phase plate is absent. Figure 13b is under the condition that the sample is semi-transparent and the phase plate is absent. Figure 13c is under the condition that the sample is absent and the phase plate is non-absorbing. Figure 13d is under the condition that the sample is absent and the phase plate is absorbing. Figure 13e is under the condition that the sample is semi-transparent and the phase plate is absorbing (i.e. typical PS microscopy setup).

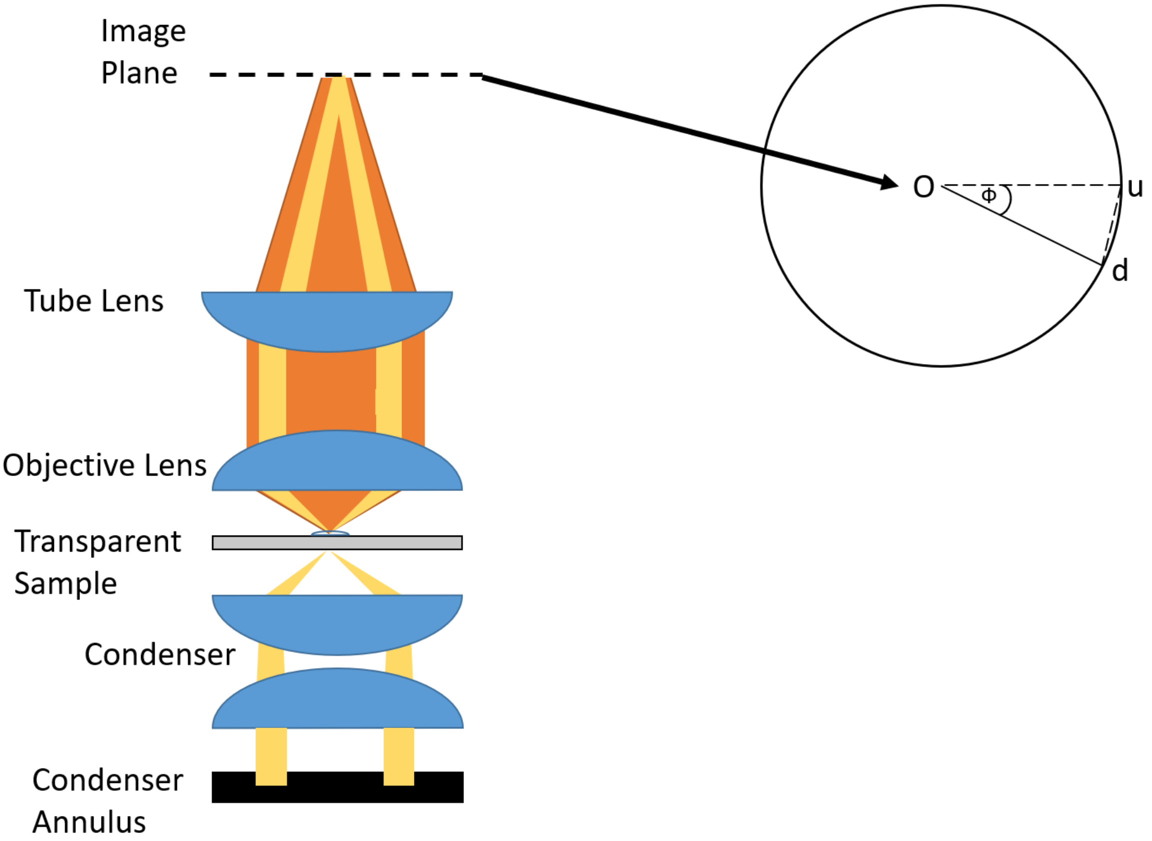

Figure 13a: Phasor representation of the microscopy of a transparent sample plotted in phase space. The microscopy setup does not contain a phase plate. Phasor length represents the root mean sum (rms) amplitude of the light, and the phasor angle relative to the horizontal represents the phase. Circles represent all possible light waves in a stage of phase contrast microscopy. Dashed lines indicate light observed at previous stages of the setup.

In Figure 13a, $\overrightarrow{Ou}$ is a phasor that represents the incidental light that illuminates the transparent sample. Assuming the sample is small and causes small amount of light diffraction and phase shifting, $\overrightarrow{Ou}$ after passing the sample will be phased shifted Φ. The resulting light imaged is represented by the phasor $\overrightarrow{Od}$ In addition to that, the small amount of diffracted portion of the incident light after passing through the small sample is represented as phasor $\overrightarrow{ud}$. The summation of $\overrightarrow{Ou}$ and $\overrightarrow{ud}$, which is $\overrightarrow{Od}$, represents the total electric field of the light at the image plane in Figure 13a. If the sample is transparent, $\overrightarrow{Od}$ has the same amplitude as the incident light $\overrightarrow{Ou}$ with an additional phase shift Φ.

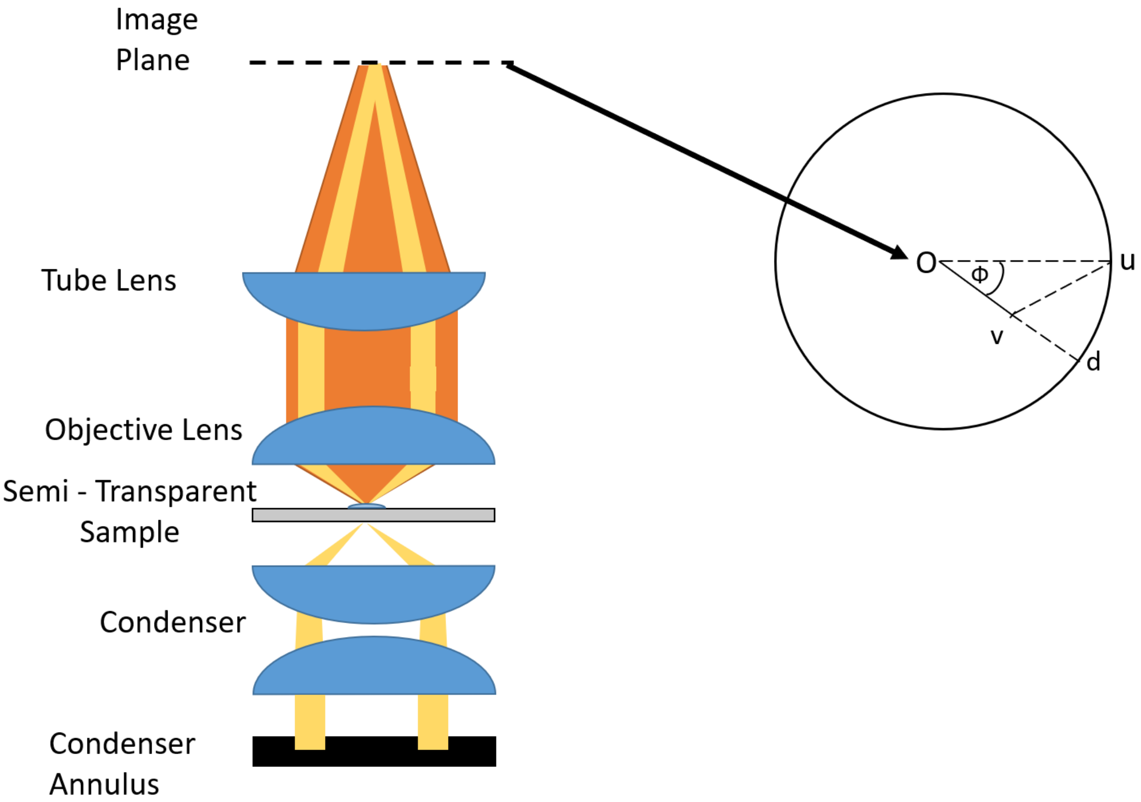

Figure 13b: Phasor representation of the microscopy of a semi-transparent sample plotted in phase space. The microscopy setup does not contain a phase plate. Phasor length represents the root mean sum (rms) amplitude of the light, and the phasor angle relative to the horizontal represents the phase. Circles represent all possible light waves in a stage of PS microscopy. Dashed lines indicate light observed at previous stages of the setup.

In Figure 13b, $\overrightarrow{Ou}$ is a phasor that represents the incidental light that illuminates the transparent sample. However, as the sample is now semi-transparent and absorbs some of the incidental light. Thus, $\overrightarrow{uv}$ rather than $\overrightarrow{ud}$ is a phasor that represents the diffracted portion of the incident light after passing through the semi-transparent sample. The summation of $\overrightarrow{Ou}$ and $\overrightarrow{uv}$, which is $\overrightarrow{Ov}$, represents the total electric field of the light at the image plane in Figure 14b. The amplitude of $\overrightarrow{Ov}$ is now smaller than the incident light $\overrightarrow{Ou}$ due to the light absorption with the semi-transparent sample, but has the same phase shift Φ as in Figure 13a.

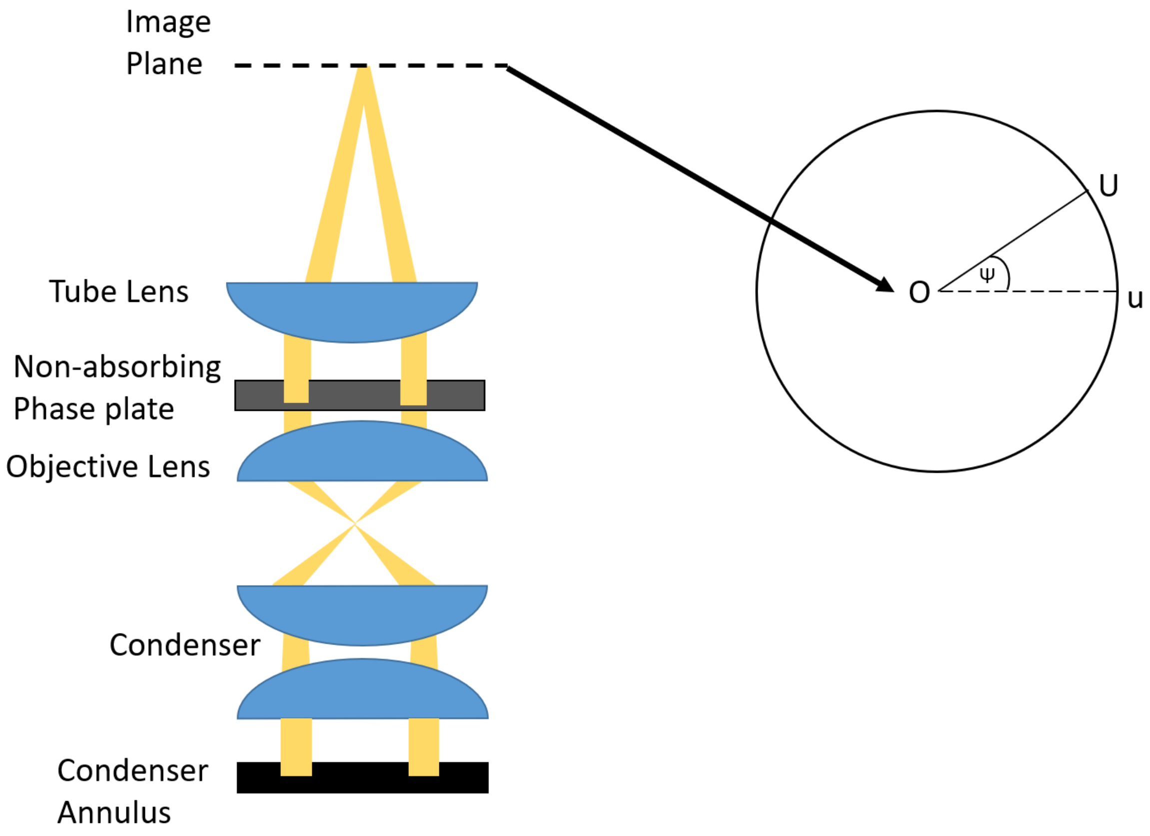

Figure 13c: Phasor representation of non-absorbing PS microscopy plotted in phase space. The microscopy setup does not contain a sample. Phasor length represents the root mean sum (rms) amplitude of the light, and the phasor angle relative to the horizontal represents the phase. Circles represent all possible light waves in a stage of PS microscopy. Dashed lines indicate light observed at previous stages of the setup.

In Figure 13c, the incidental light, $\overrightarrow{Ou}$, does not pass through an imaging sample. Instead, $\overrightarrow{Ou}$ passes through a phase plate that phase shift Ψ along the optical path of the incidental light. $\overrightarrow{OU}$ represents the total electric field of the light at the image plane in Figure 14c. If the phase plate is non-absorbing, $\overrightarrow{OU}$ has the same magnitude as $\overrightarrow{Ou}$ due to the lack of intensity reduction and the phase shift Ψ.

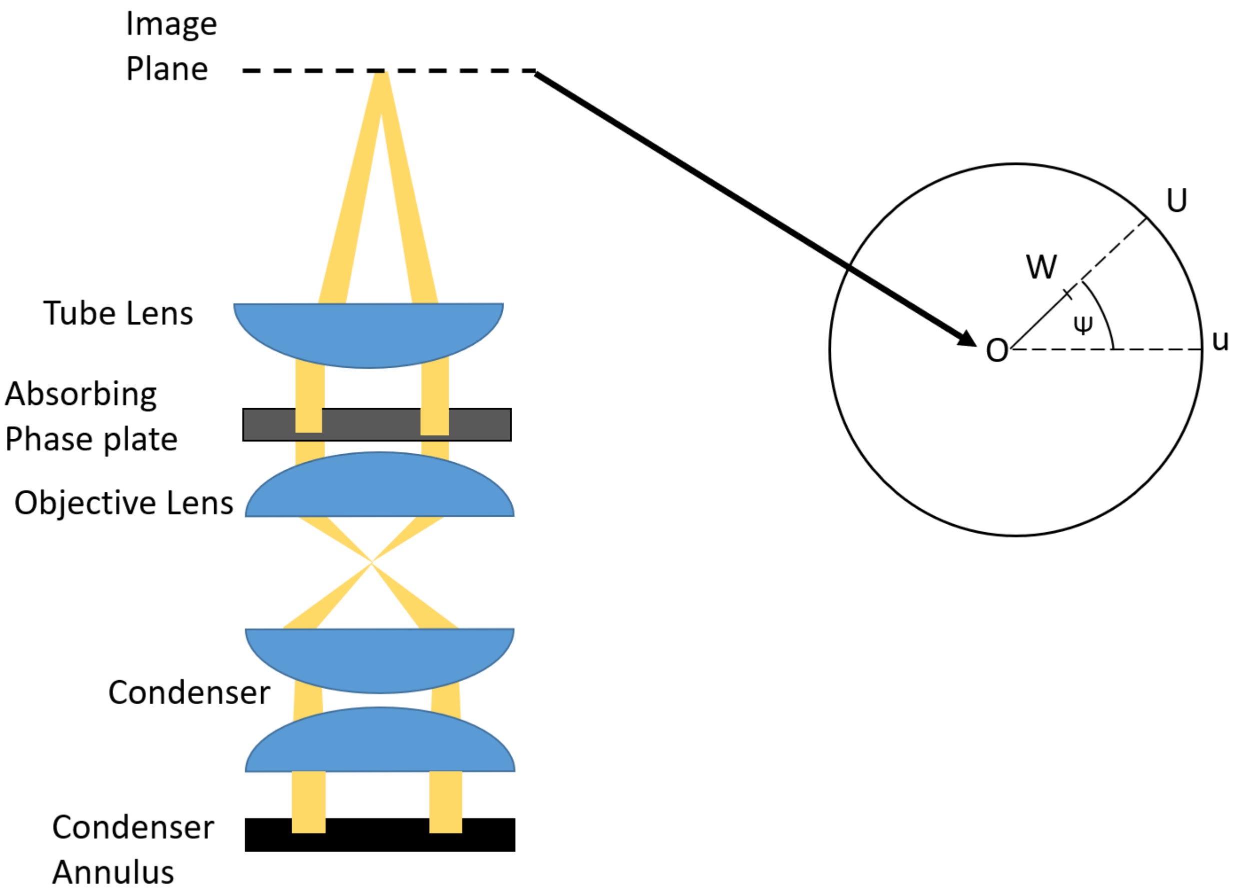

Figure 13d: Phasor representation of absorbing PS microscopy of no sample plotted in phase space. The microscopy setup does not contain a sample. Phasor length represents the root mean sum (rms) amplitude of the light, and the phasor angle relative to the horizontal represents the phase. Circles represent all possible light waves in a stage of PS microscopy. Dashed lines indicate light observed at previous stages of the setup.

In Figure 13d, the incidental light, $\overrightarrow{Ou}$, passes though a phase plate like in Figure 13c. However, the phase plate does absorb some of the incidental light. $\overrightarrow{OW}$ represents the total electric field of the light at the image plane in Figure 13d. $\overrightarrow{OW}$ has reduced magnitude in regards to $\overrightarrow{OU}$ due to the absorption reducing the intensity. However it still has the phase shift Ψ like $\overrightarrow{OU}$ in Figure 13c.

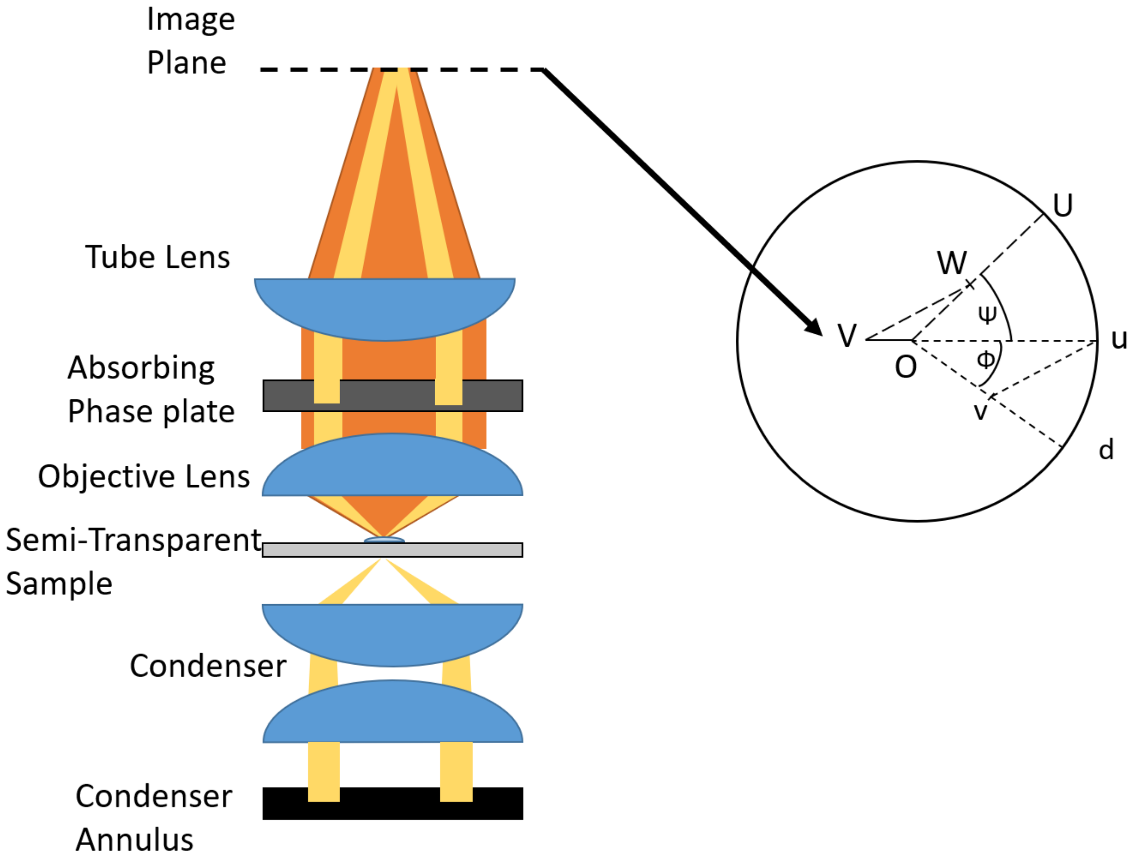

Figure 13e PS vector diagram with an absorbing phase plate and semi-transparent sample. Phasor representation of the microscopy of a transparent sample plotted in phase space. Phasor length represents the root mean sum (rms) amplitude of the light, and the phasor angle relative to the horizontal represents the phase. Circles represent all possible light waves in a stage of PS microscopy. Dashed lines indicate light observed at previous stages of the setup.

In Figure 13e, the PS analysis can be generalized with combining the setups of Figure 13b and 13d. The PS microscopy setup now contains the semi-transparent sample and an absorbing phase plate. Let $\frac{1}{K}$ and $\frac{1}{N}$ represent the fraction of reduced intensity of the light after passing though the semi-transparent sample and absorbing phase plate respectively. In other words, K and N are inverse attenuation coefficient of the semi-transparent sample and absorbing phase plate respectively. Thus, the amplitudes of $\overrightarrow{Ov}$ and $\overrightarrow{OW}$ are $\frac{1}{\sqrt{K}}$ and $\frac{1}{\sqrt{N}}$ respectively. The amplitudes of the electric fields described in the phase diagram are square roots of the amplitude of Poynting's vector describing the light propagation in ray optical analysis. Poynting's vector, $\vec{\boldsymbol{S}}$, is derived from Maxwell analysis to describe the energy flow of electromagnetic wave in eq. 23.

$$\vec{\boldsymbol{S}} = \frac{1}{\mu_0}\vec{\boldsymbol{E}} \times \vec{\boldsymbol{B}} \tag{23}$$

Where $\vec{\boldsymbol{E}}$ and $\vec{\boldsymbol{B}}$ represents the electric field and magnetic field respectively. μ_0 is the magnetic permeability, which is a constant. The vector can be time averaged to a root mean squared value For plane wave propagation, $\vec{\boldsymbol{E}} = E_m \sin(kx - \omega t)$ and $\vec{\boldsymbol{B}} = B_m \sin(kx - \omega t)$ where B_m and E_m represent the root mean squared amplitude of the electric and magnetic sinusoidal waves respectively. $k = \frac{2\pi}{wavelenght\ of\ light}$ is the propagation constant and ω is the angular frequency. As the electric and magnetic fields are orthogonal to each other in plane wave theory, the amplitude of $\vec{\boldsymbol{S}}$ can be derived in eq. 24.

$$\left|\vec{\boldsymbol{S}}\right| = \frac{1}{\mu_0} E_m \sin(kx - \omega t)\ B_m \sin(kx - \omega t) \tag{24}$$

B_m can be expressed as a function of E_m in eq. 25, which can be derived from applying plane wave theory to Maxwell's equations.

$$B_m = \frac{E_m}{c} \tag{25}$$

Where c is the speed of light. Substituting B_m in the modified $\vec{\boldsymbol{S}}$ yields eq. 26.

$$\left|\vec{\boldsymbol{S}}\right| = \frac{1}{c\mu_0} E_m^2 (\sin(kx - \omega t))^2 \tag{26}$$

The modified Poynting vector indicates that the energy flow over a cross sectional area is proportional to the square of the amplitude of the electronic field.

Combining the above phasor analysis for the electric fields as well as the correlation between the amplitude of the electric fields and the amplitude of Poynting vector (i.e., light intensity I), the following correlation among phasor intensities $\overrightarrow{Ou}, \overrightarrow{Ov}$, and $\overrightarrow{OW}$ can be obtained with the assumption that the intensity of $\overrightarrow{Ou}$ is 1.

$$\mathrm{I} = \overrightarrow{|OV^2|} = \left|\left(\overrightarrow{WV} - \overrightarrow{OW}\right)^2\right| = \left|\left(\overrightarrow{uv} - \overrightarrow{OW}\right)^2\right| = \left|\left(\overrightarrow{Ou} - \overrightarrow{Ov} - \overrightarrow{OW}\right)^2\right| \tag{27}$$

The intensity equation can be expanded into eq. 28.

$$\begin{aligned}\mathrm{I} = \left|\left(\overrightarrow{Ou} - \overrightarrow{Ov} - \overrightarrow{OW}\right)^2\right| = \ &|\overrightarrow{Ou} \cdot \overrightarrow{Ou} - \overrightarrow{Ou} \cdot \overrightarrow{Ov} - \overrightarrow{Ou} \cdot \overrightarrow{OW} - \overrightarrow{Ov} \cdot \overrightarrow{Ou} + \overrightarrow{Ov} \cdot \overrightarrow{Ov} + \\ &\overrightarrow{Ov} \cdot \overrightarrow{OW} - \overrightarrow{OW} \cdot \overrightarrow{Ou} + \overrightarrow{OW} \cdot \overrightarrow{Ov} + \overrightarrow{OW} \cdot \overrightarrow{OW}|\end{aligned} \tag{28}$$

With the correlations among the amplitude for the electric fields which can be obtained from the geometric analysis of the phasor diagram, eq. 28 is modified into eq. 29.

$$\begin{aligned}I = (1 * 1)\cos 0 - \left(1 * \tfrac{1}{\sqrt{K}}\right)\cos\phi - \left(1 * \tfrac{1}{\sqrt{N}}\right)\cos\psi - \left(\tfrac{1}{\sqrt{K}} * 1\right)\cos\phi + \left(\tfrac{1}{\sqrt{K}} * \tfrac{1}{\sqrt{K}}\right)\cos 0 + \\ \left(\tfrac{1}{\sqrt{K}} * \tfrac{1}{\sqrt{N}}\right)\cos(\phi+\psi) - \left(\tfrac{1}{\sqrt{N}} * 1\right)\cos\phi + \left(\tfrac{1}{\sqrt{N}} * \tfrac{1}{\sqrt{K}}\right)\cos(\phi+\psi) + \left(\tfrac{1}{\sqrt{N}} * \tfrac{1}{\sqrt{N}}\right)\cos 0\end{aligned} \tag{29}$$

The intensity equation can be simplified to equation 30.

$$I = 1 + \frac{1}{K} + \frac{1}{N} + \frac{2\cos(\phi+\psi)}{\sqrt{KN}} - \frac{2\cos\phi}{\sqrt{K}} - \frac{2\cos\psi}{\sqrt{N}} \tag{30}$$

If we define contrast as the difference between the background intensity and intensity at image plane over the background intensity, then the contrast equation is defined in eq. 31.

$$Contrast = \frac{\frac{1}{N} - I}{\frac{1}{N}} = 1 - NI = N + \frac{N}{K} + \frac{2\sqrt{N}cos(\psi+\phi)}{\sqrt{K}} - 2\sqrt{N}\cos\psi - \frac{2N\,cos\,\phi}{\sqrt{K}} \tag{31}$$

When the contrast value is positive, the sample in the images would appear darker than the background and vice versa for negative contrast values.

In positive phase contrast (PS), $\Psi = \frac{\pi}{2}$ and N=1. The intensity with these new values is reduced to eq. 32.

$$I = 1 + 1 + \frac{1}{K} + \frac{2\cos(90^{o} + \phi)}{\sqrt{K}} - 2\cos(90) - \frac{2\cos\phi}{\sqrt{K}} = 2 + \frac{1}{\mathrm{K}} - \frac{2(\sin\phi + \cos\phi)}{\sqrt{K}} \qquad (32)$$

If a pure phase samples are imaged, K = 1 and the intensity is reduced to eq. 33 and plotted in Figure 14.

$$I = \ 3 - 2(\sin\phi + \cos\phi) \qquad (33)$$

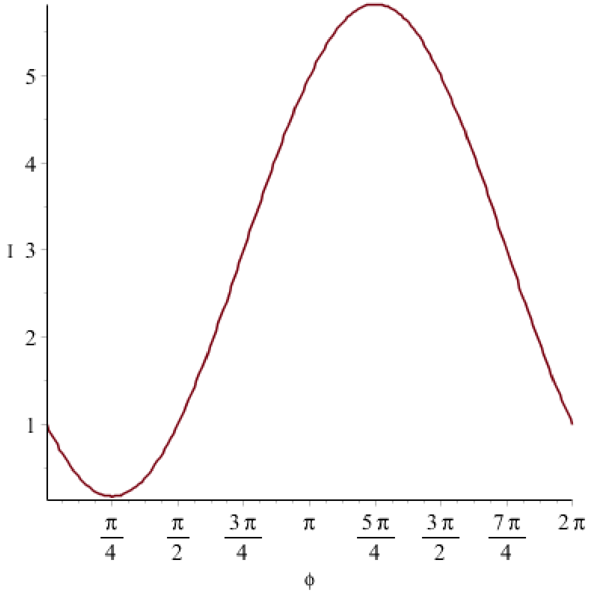

Figure 14: Intensity plot for one period of the phase shift ϕ.

The contrast is calculated from this intensity is shown in eq. 34 and plotted in Figure 15.

$$\text{Contrast} = 1 - \text{NI} = 1 - \text{I} = 2(\sin\phi + \cos\phi) - 2 \qquad (34)$$

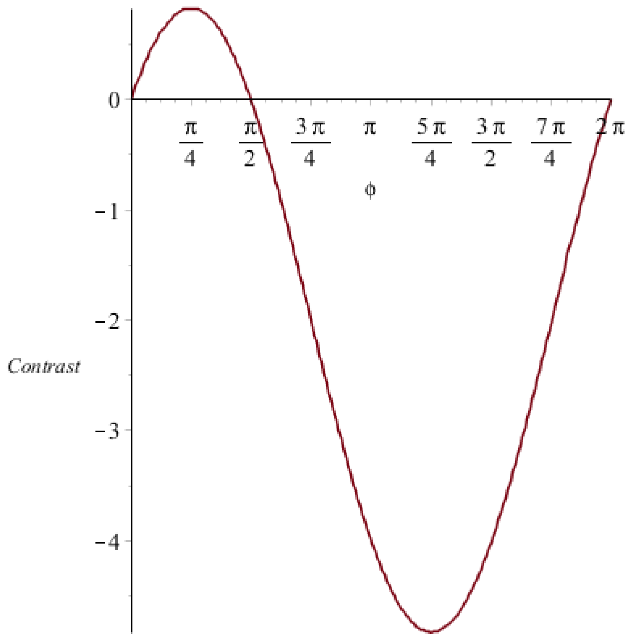

Figure 15: Contrast plot for one period of phase shift ϕ.

It appears that there is only contrast for sample phase shifts between 0-90 degrees of each period. Other phase shifts will indicate a reversal of contrast.

In samples with absorption, positive PS microscopy reduces eq. 29 to eq. 35. Eq. 35 is plotted in Figure 16 and 17.

$$Contrast = 1 - NI = -1 + \frac{1}{K} + \frac{2\,sin(\phi)}{\sqrt{K}} - \frac{2\cos\phi}{\sqrt{K}} \qquad (35)$$

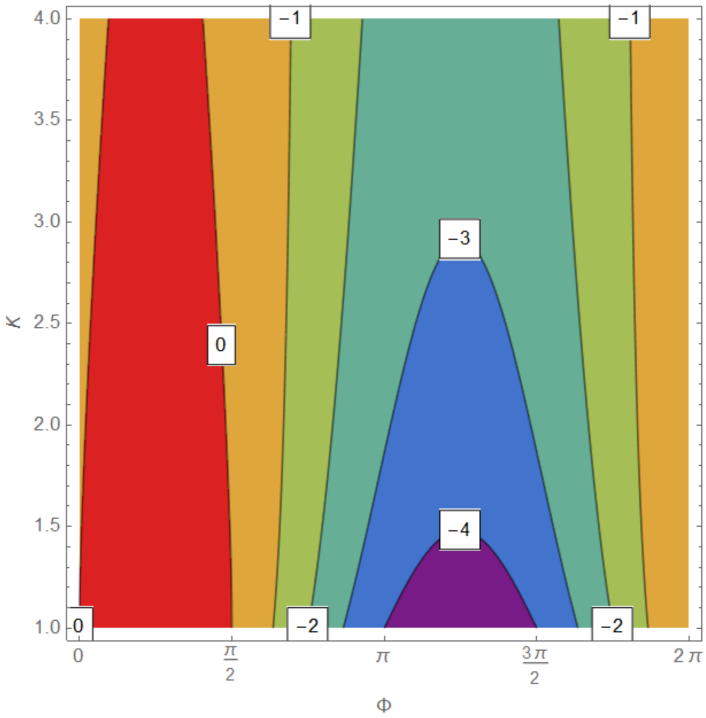

Figure 16: Contour plot of contrast value variation when the optical phase changes from 0 to 2π and when the attenuation ratio changes from 1 to 4.

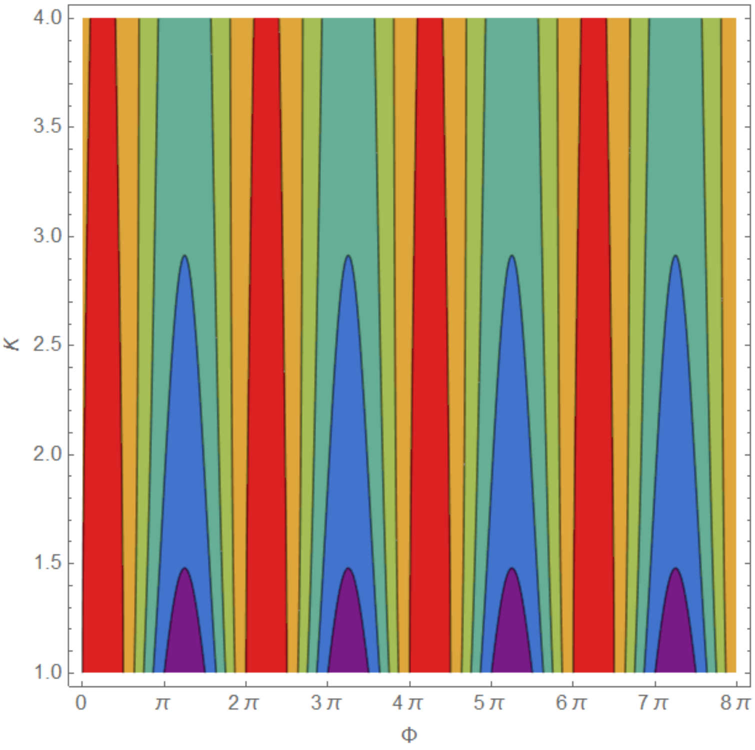

Figure 17: Contour plot of contrast value variation when the optical phase changes from 0 to 8π and when the attenuation ratio changes from 1 to 4.

In our setup, the phase plate also absorbs half the intensity of the 0^{th} order light and has a phase shift $\frac{\pi}{2}$ of all higher order light. (N=2 and $\phi = \frac{\pi}{2}$). The contrast is calculated in eq. 36 and is plotted in Figure 18.

$$Contrast = 1 - NI = -\frac{2}{K} + \frac{2\sqrt{2}\,cos\left(\frac{\pi}{2}+\phi\right)}{\sqrt{K}} - \frac{4\,cos\,\phi}{\sqrt{K}} \tag{36}$$

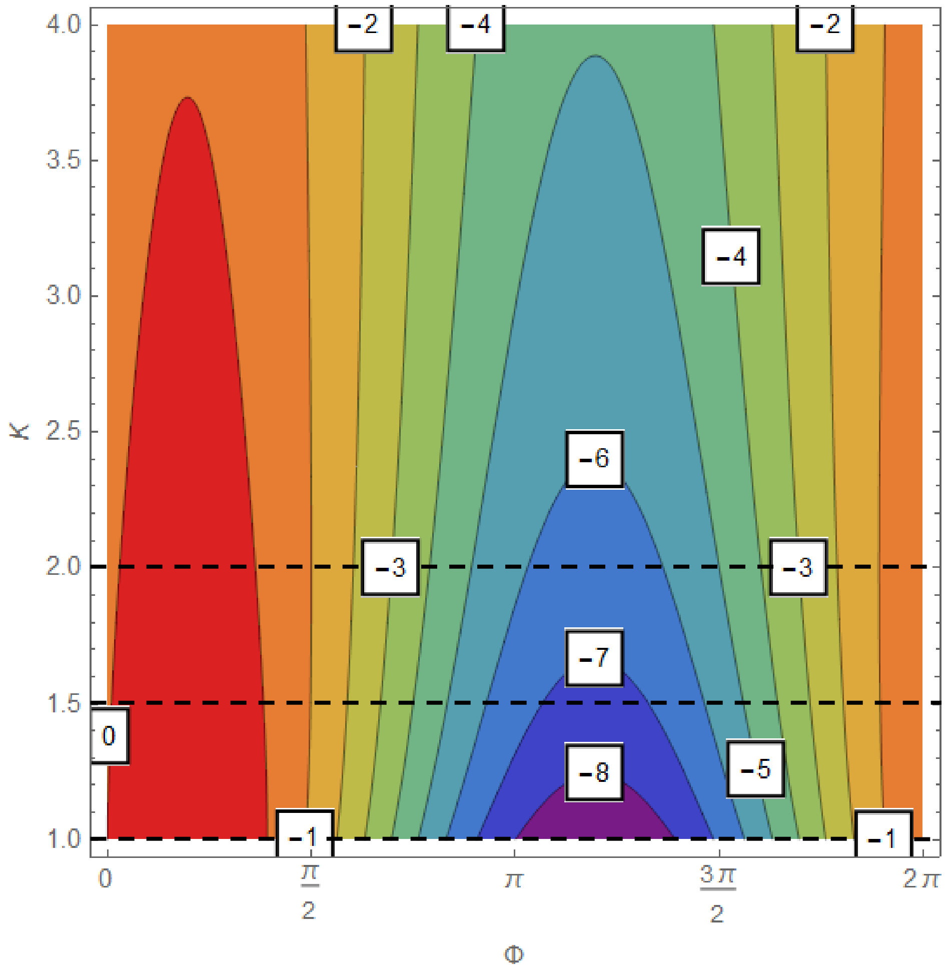

Figure 18: Contour plot of variation of contrast value when the optical phase changes from 0 to 2π and when the attenuation ratio changes from 1 to 4. Positives contrast values indicated positive PS, negative numbers indicated negative PS.

In order to better understand how the phase change relates to the contrast, Figures 19a-c are two dimensional cutouts of the contour plot in Figure 18. The Figures 19a-c will also contain an intensity bar to match the contour plot to relate the contrast plot to the intensity of the PS image.

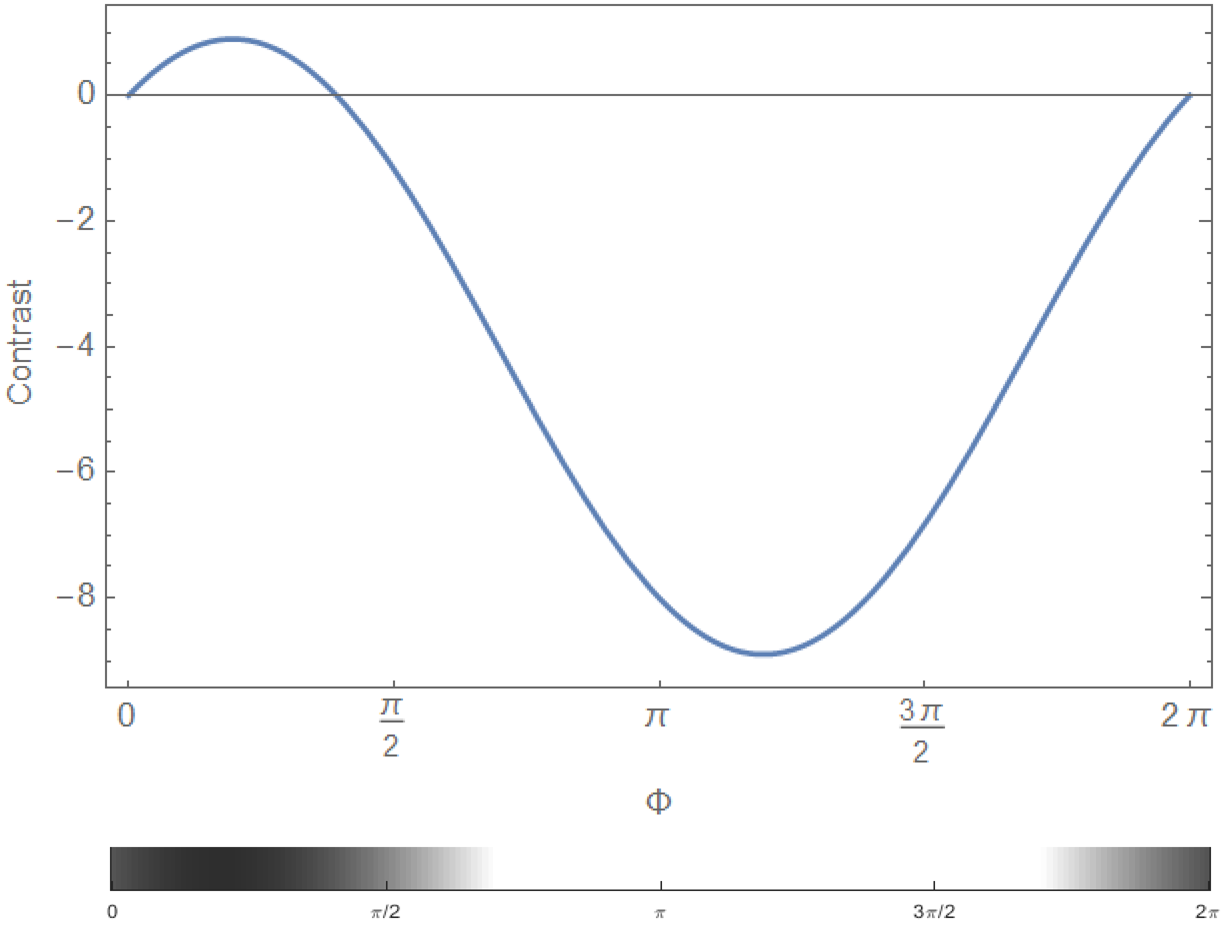

Figure 19a: Contrast plot at the horizontal dotted line starting at N = 1 in Figure 18.

The contrast plot in Figure 19a indicates that the resulting PS image of a pure phase (i.e., non-absorbing) sample will be darker than the zeroth order light between the 0 and .392 π radians sample phase shifts and be lighter than between the .392 π radians and 2 π radians sample phase shifts. The contrast will become the darkest at around .196 π radians and will be brightest around 1.196 π radians. The sinusoidal profile of the contrast plot also indicates that, there are at least two phase shift that can be derived from nearly every contrast level. The multiple phase shift values yielding the same light intensity indicate that intensity and phase shifts are not linearly proportional and thus the analysis of PS imagining should be focused on analysis of intensities of neighboring regions compared to the intensity of the zeroth order light.

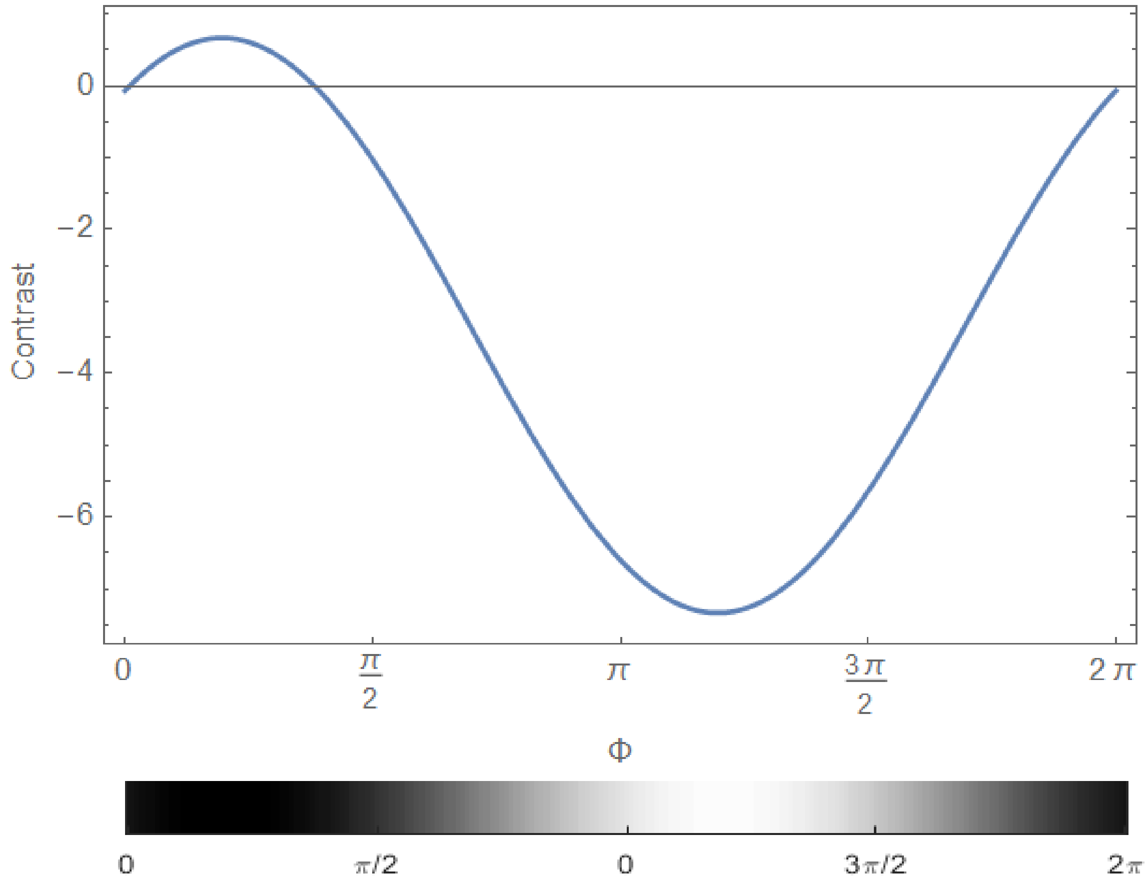

Figure 19b: Contrast plot at the horizontal dotted line starting at N = 1.5 in Figure 18.

The contrast plot in Figure 19b is similar to the contrast plot in Figure 19a, in that smaller sample phase shifts tend to indicate a dark contrast and larger sample phase shifts tend to indicate brighter contrast. However, the plot appears to be shifted forward 0.00948 π radians. This means that phase shifts between 0 and 0.00948 π radians appear slightly brighter than the background and the max dark and max light contrast happen with an added 0.00948 π radians phase shift. It should also be noted that the amplitude of the contrast plot is less than the N = 1 plot.

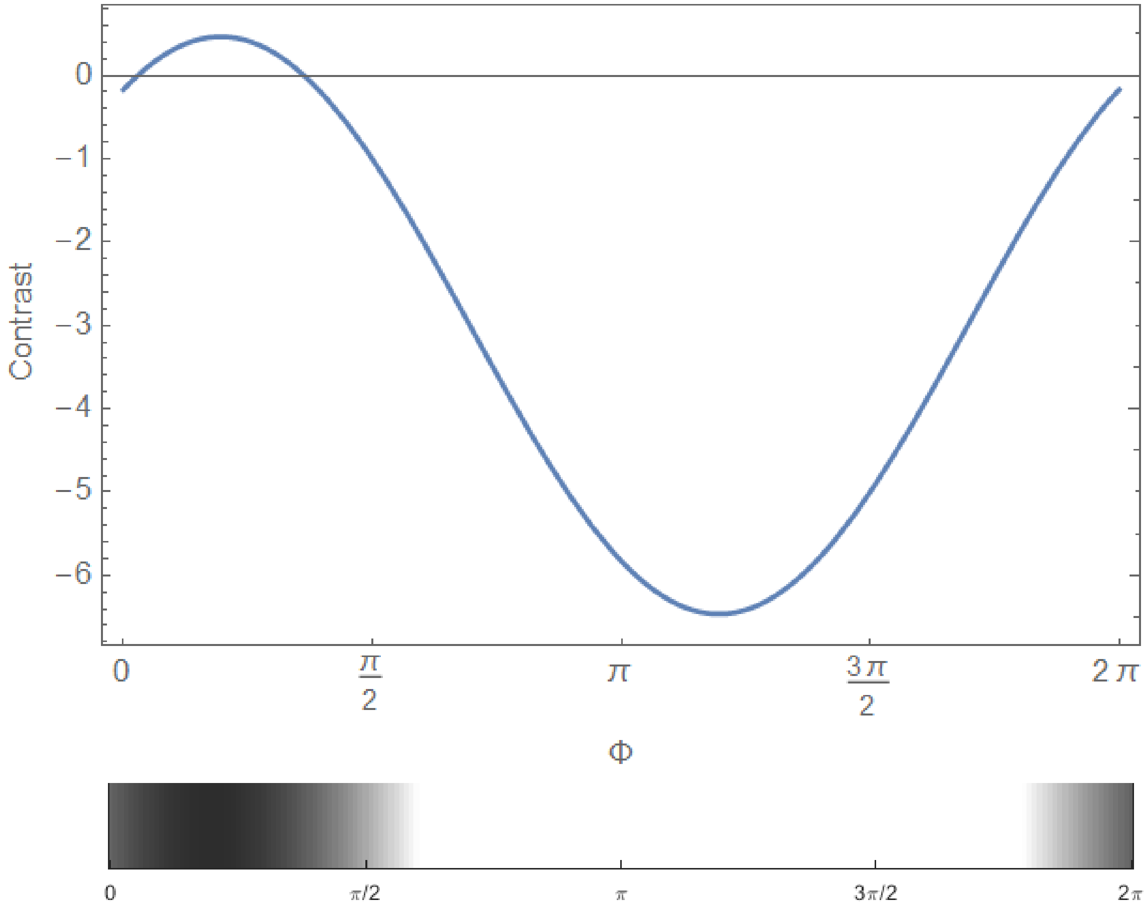

Figure 19c: Contrast plot at the horizontal dotted line starting at N = 2 in Figure 18.

The contrast plot in Figure 19c is similar to the contrast plot in Figure 19b, in that smaller sample phase shifts tend to indicate a dark contrast and larger sample phase shifts tend to indicate brighter contrast. However, the plot appears to be shifted forward 0.0292 π radians. This means that phase shifts between 0 and 0.0292 π radians appear slightly brighter than the background and the max dark and max light contrast happen with an added 0.00948 π radians phase shift. It should also be noted that the amplitude of the contrast plot is less than the N = 1 plot. To confirm that the contour plot is repeated for each phase period, the contrast equation is plotted over four periods in Figure 20.

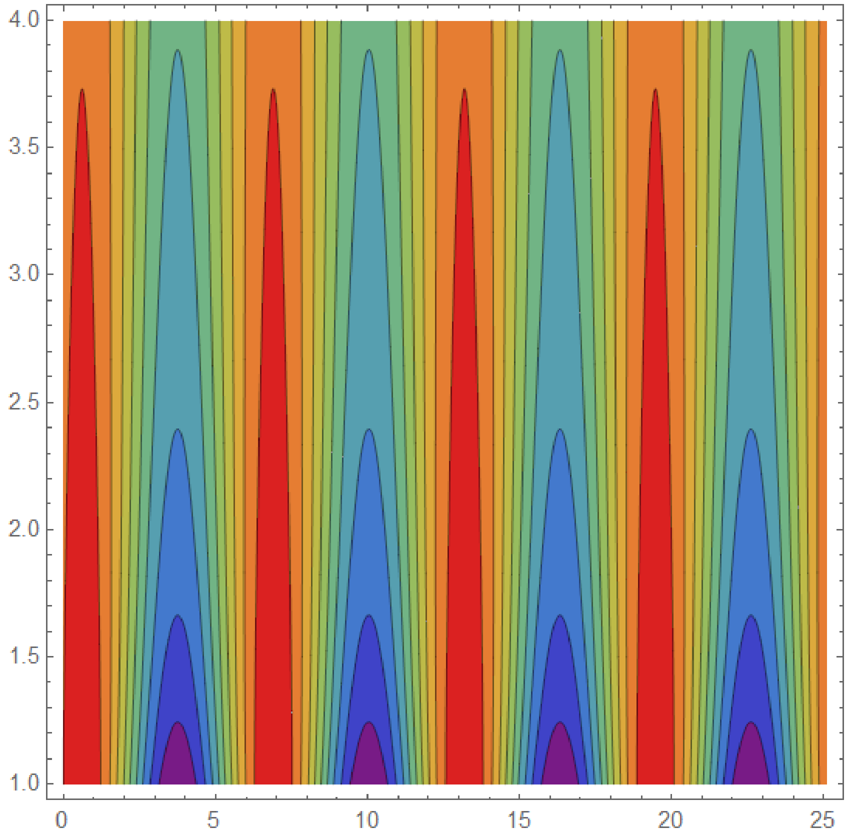

Figure 20: Contour plot of contrast for four full phase period and sample absorption from no absorption to ½ intensity absorption.

As the contour plot repeats after a full phase period (2π) for the entire plot, it reasonable to assume that the contrast will repeat after every phase period. Thus, the intensities of the PS images can be interpreted assuming that the phase plate affects none of the phase shifted light.

In practice however, some of the phase shifted light does interact with the phase shifted portion of the phase plate. In large flat samples, some of the phase shifted light around the center does not diffract significantly enough away from the optical path of the undiffracted light. The phase plate would then phase shift the diffracted light from the center along with the diffracted light. Thus the phase difference between the diffracted and undiffracted light at the center of a large is more analogues to the brightfield imaging and will have reduced destructive interference. The reduced destructive interference will leave the image of the center with a higher intensity than the regions' closer to the edges as those regions are imaged in PS microscopy. This difference in intensities is an optical artifact described as the shade off effect.

Another way phase shifted light interacts with the phase plate is on the edges of samples. As noted earlier, the diffraction on the edges do not form a wave front, and instead diffract in all directions. Some of this diffracted light from the edges may fall into the phase shifting part of the phase plate. This portion of diffracted light will then gain an additional phase shift. The additional phase shift will reduce the destructive interference and may increase constructive interference of the diffracted light portion with the undiffracted light. The new interference manifest as an optical artifact where a brighter region surrounds the edges of the sample that is imaged. The name of this artifact is the halo effect as the brighter region is typically very thin and thus has the appearance of a halo. The shade off and halo effect are the two major optical artifacts that should be considered when analyzing PS images [29].

To verify our understanding of phase contrast (PS) microscopy, analysis will be done on a PS image of an erythrocyte in Figure 21. The erythrocyte images was enlarged from a PS image provided by Dr. Richard Wheeler in Figure 22 [47].

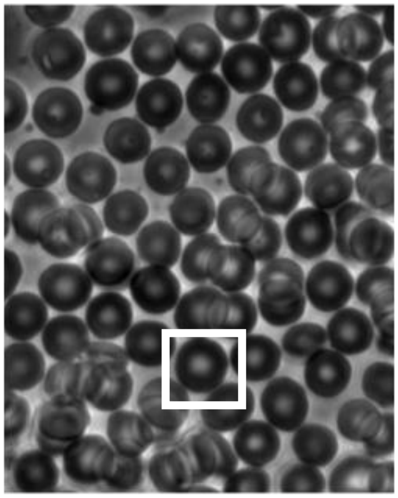

Figure 21: PS Image of erythrocyte by Dr. Richard Wheeler. Distributed by Creative Commons Attribution-Share Alike 3.0 Unported license. Image is slightly modified to include a white box to indicated the location of enlarged image of Figure 23 [47].

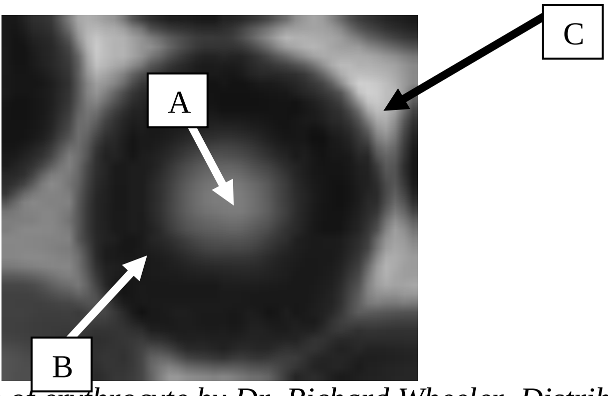

Figure 22: Enlarged PS Image of erythrocyte by Dr. Richard Wheeler. Distributed by Creative Commons Attribution-Share Alike 3.0 Unported license [47].

The erythrocyte image in Figure 22 has a bright center (labeled A). The cell image seems be surrounded with a bright ring (labeled C). The bright ring comes from the halo effect, a typical artifact of phase contrast described previously. The brightness of cell image itself appears to oscillate between dark and light rings, with the light ring labeled B. The oscillation indicates a change of the optical path within the cell. An isotonic erythrocyte typically is a biconcave disk shape with the thickest region being around 2.2 microns and the thinnest around 1.7 micron

[48]. A schematic of an approximate cross section of a free floating erythrocyte is given in Figure 23.

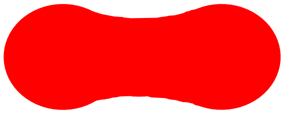

Figure 23: Cross section of a free floating erythrocyte.

It should be noted that the erythrocytes are imaged in a blood smear, so the image may not exactly match the profile of the free floating erythrocyte. The erythrocyte and the blood plasma have relatively similar refractive indexes (~1.41 and ~1.35 respectively) [49, 50]. As the erythrocyte has slightly higher refractive index, light that diffracts from the edge of the erythrocyte will angle away from the cell. It is because of this angling that the halo effect appears on the outside rather than the inside of the erythrocyte.

In order to analyze the intensity distribution inside the erythrocyte, we need to determine if the largest phase shift done to the light after interacting with the cell. The differences in refractive index between the erythrocyte and the blood plasma are relatively small (~.06). Multiplying the refractive index difference and the largest erythrocyte thickness yields (~2.2 microns) the largest expected optical path length of .132 microns (Δ). The phase shift (δ) of the light passing through the erythrocyte can be calculate from the optical path difference in eq. 22.

$$\delta = \ 2\pi\Delta/\lambda \tag{22}$$

Where λ is the wavelength of the illuminating light, which is assumed to be around 532 nm. The largest expected phase shift is expected to be around .496 π radians. This phase shift is lower than the full 2 π period of before, this would mean that a quantitative phase analysis can be performed. The contrast value for this phase shift assuming negligible absorption is about -1.12153. The negative value indicates that the thickest region should be brighter than the background image. The dark ring (labeled B) in Figure 22 appears to match the thickest region of the erythrocyte, which can confirm phase analysis. Additionally the dark region inside would match the positive contrast values found in the earlier section of the phase plot, indicting a reduced phase shift in the center region of Figure 22. The bright center labeled A indicates that there is reduced phase shift in the center due to the reduced thickness as indicated with the erythrocyte cross section. However this shift may be intensified with the shade off effect, which tend to make the center of a sample brighter due to having some of the phase shifted light pass thought the phase altering section of the phase plate.

5 ANALYSIS AND DISCUSSION OF LASER MICROSCOPY MICROCAVITATION IMAGES*

5.1 Introduction

This section will perform analysis for the both the initial version and the final version microscopy setup. The analysis of the initial version setup will include comparisons with the numerical model. The brightfield (BF) and phase contrast (PS) configurations of the final version microscopy setup are analyzed separately through diameter measurements before being compared directly. The comparison will be done for both in distilled water and polyacrylamide gel in water solution (10% PAA gel).

5.2 Initial Version Analysis

The time evolutions of the diameters of the bubble and spherical shockwave were measured from images of the initial version microscopy setup and plotted in Figures 24 and 25.

---

* Part of this chapter is reprinted with permission from "Direct numerical simulation of microcavitation processes in different bio environments" by Kevin Ly, Sy-bor Wen, Morgan s. Schmidt, and Robert J. Thomas, 2017. *Optical Interactions with Tissue and Cells Xxviii*, Vol. 100602, Copyright 2017 by SPIE.

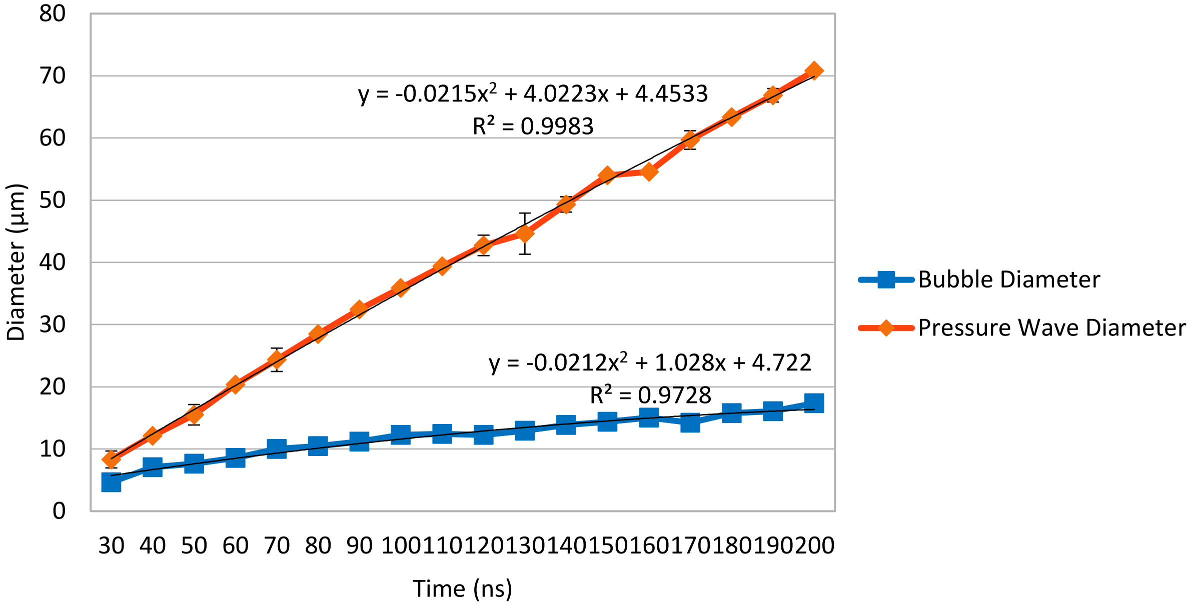

Figure 24: Evolution of the diameters of the vapor bubble and shockwave from laser-induced microcavitation in distilled water. The black line is the regression fit of the trajectory of the vapor bubble diameter. Standard deviation determines the error bars.

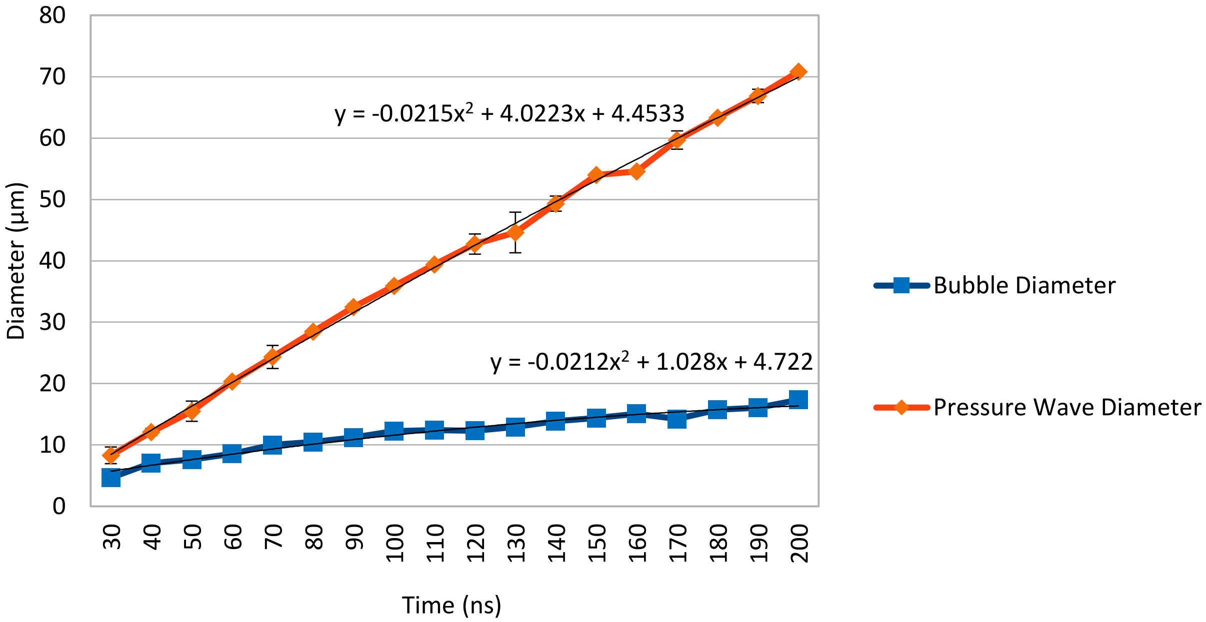

Figure 25: Evolution of the diameters of the vapor bubble and shockwave from laser-induced microcavitation in 10% PAA gel. The black line is the regression fit of the trajectory of the vapor bubble diameter. Standard deviation determines the error bars.

The spherical shockwave fits with our directly numerical simulation as in Figure 2b as a rapid outward propagating shockwave is induced after the laser ablation. The expansion of the vapor bubble, has a much lower speed in both sets of experiment. The images for both water (Figure 8a) and PAA gel (Figure 8b) show that the speed/shape of shockwaves are similar for both water and PAA gel, which lends credence to using water properties and physics to create the microcavitation simulations. This finding is reflected in the diameter plots (Figures 24-25), as the values appear to be similar for each time step. The diameter plots also indicate that the bubble and shockwave expansion gets slightly slower over time. The trend collaborates previous studies have determined that bubble and shockwave growth tends to reduce over time [15]. However the greatest reduction occurs in the first 30 ns of microcavitation event. Our setup was not able to image the first 20 ns of the microcavitation event due to plasma light obscuring the cavitation bubble and shockwave.

The average speed of the pressure waves in both materials was about 1600 m/s. This value is similar to ~1800 m/s obtained from the direct simulation. Though the shockwave propagation shows a good agreement between the experiment and the direct simulation, the evolution of the vapor bubble shows less consistency between the experimental and the simulation: where the simulation predicts an evolution of the vapor bubble from elliptical to spherical shape in the first 1 μs after the laser pulse, and the shape of the vapor bubble is a spherical shape from ~20 ns after the laser pulse based on the experiment. Also, the vapor bubble expands at a much lower speed from the simulation compared with the experimental measurement.

These deviations in the vapor bubble dynamics predicted from the direct simulation and that measured from the experiment can be attributed to two main factors. First, the wavelength applied in the simulation and the experimental are ~4 μm and 1 μm, respectively. Water provides two orders of magnitude higher light absorption at λ=4 μm compared with that at λ=1 μm. Therefore, the simulated laser energy to induce the microcavitation is ~0.02 mJ which is much lower than E~8 mJ in the experiment. Second, the light absorption mechanism in water at λ=4 μm is mainly due to linear light absorption while the light absorption mechanism in water at λ=1 μm is mainly due to photoionization and the followed Avalanche breakdown. The Avalanche breakdown can be observed from an interesting feature in all the images from the experiment that have a white light spot in the center that cannot be eliminated with a notch filter at the strobe beam wavelength. For delay times shorter than ~20- 30 ns, the white light emission from electron recombination after the Avalanche breakdown is too strong, and obscures the features of both the bubble and shockwave. As the current simulation does not yet account for the potentization and the followed Avalanche breakdown, it is not surprising that the simulation does not match the results of this portion of the experiment, especially in the evolution of the size/shape of the vapor bubble.

5.3 Final Version Analysis: Brightfield Configuration

The time evolutions of the diameters of the bubble and spherical shockwave were measured from the images of the brightfield configuration of the final microscopy setup and plotted in Figure 26.

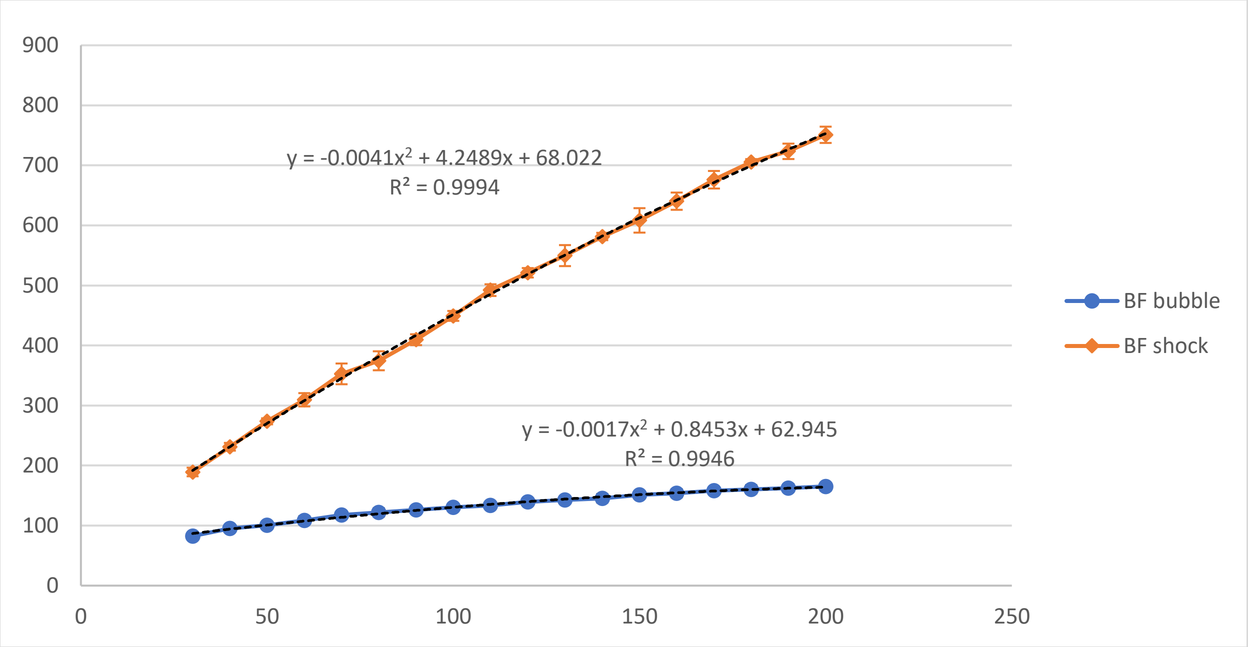

Figure 26: Evolution of the diameters of the vapor bubble and shockwave from brightfield microscopy imaging of laser-induced microcavitation with laser pulse energy at ~8 mJ in distilled water. Standard deviation determines the error bars.

The general trends of the time variation of the shockwave and bubble diameters of the microcavitation under E~ 8.2 mJ match that of the initial version setup with the shockwave diameter expanding at a faster rate than the bubble diameter. The negative second order term of all trend lines in Figure 26 indicate that the shockwave propagation and bubble velocity speed do slow down over time. Previous studies have shown that shockwave propagation and bubble expansion deceleration do occurs over time [51-53]. The average standard deviation calculated for the bubble and pressure wave measurements during early microcavitation is ~5.3 and ~11.2 µm respectively, which is much higher than the average standard deviation in the initial setup which is less than 1 µm for both the bubble and pressure wave. The reduced consistency in the measurements can be attributed to the small numerical aperture under the second setup. The numerical apertures of the initial setup is larger than .1 and the numerical aperture of the final setup less than .1. The lower numerical aperture of the final setup is due to the small laser size and the longer focal length lens required to accommodate the PS components. The lower numerical aperture reduces the stability of the focal spot and increases the likelihood of the cavitation to occur slightly above or below the focal spot.

5.4 Final Version Analysis: Phase Contrast (PS) Configuration

The time evolutions of the diameters of the bubble and spherical shockwave were measured from the images of the phase contrast configuration of the final microscopy setup and plotted in Figure 27.

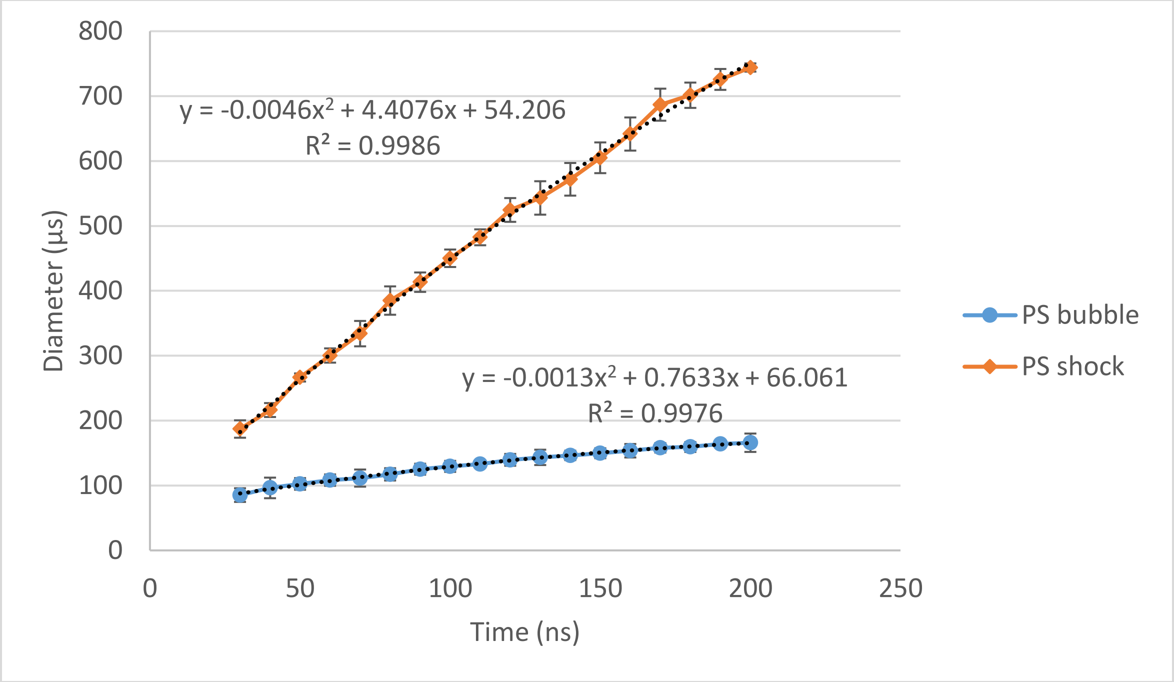

Figure 27: Evolution of the diameters of the vapor bubble and both shockwaves (pressure waves) from phase contrast imaging of laser-induced microcavitation with laser energy at 8.2 mJ in distilled water. Standard deviation determines the error bars.

The general trend of the shockwave and bubble diameters of the cavitation initiated with a 8.2mJ pulse seem to match that of the brightfield configuration with the shockwave diameter expanding at a faster rate than the bubble diameter, including the early expansion speed. The negative second order term of all trend lines in Figure 27 indicate that the shockwave propagation and bubble velocity speed does decelerate over time. Previous studies have shown that shockwave propagation and bubble expansion deceleration do occurs over time [51-53]. The average standard deviation calculated for the bubble and pressure wave measurements during early microcavitation is about 9.3 and 17.1 µm respectively, which is larger than the standard deviations of brightfield images. The larger standard derivation in the shockwave may be due to phase contrast imaging the cavitation bubble boundary with high contrast to the surrounding material. As the boundary is not very spherical during the early cavitation period (<200ns), there would be more variation between cavitation images depending on the direction the diameter is measured in. The bubble boundary will discussed in more detail in section 5.5.

5.5 Phase Contrast (PS) vs Brightfield in Distilled Water

PS contrast results at 200 ns and 300 ns are selected to explain the detailed features of imaging as well as their causes. Phase contrast (PS) images are in Figures 28a and 28b to the brightfield (BF) images are in Figures 28c and 28d.

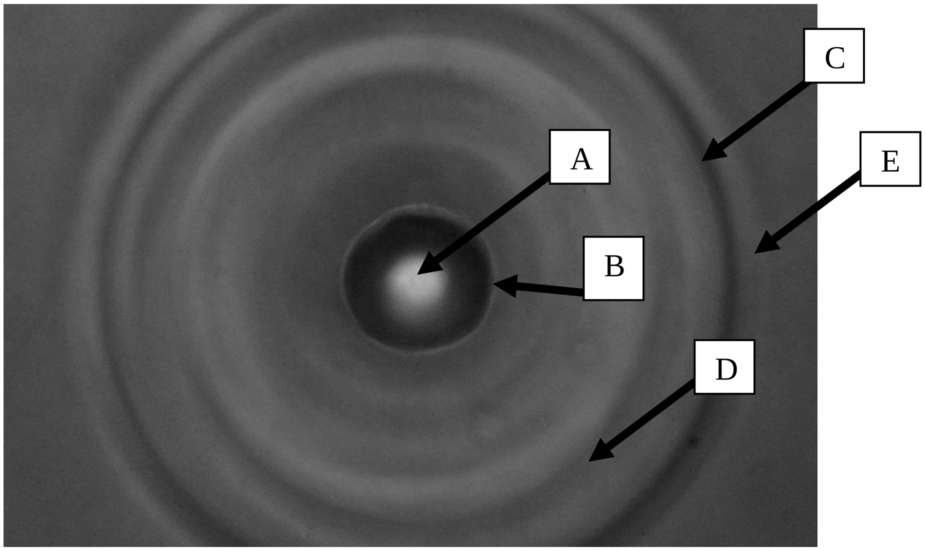

Figure 28a:200 ns Phase Contrast image.

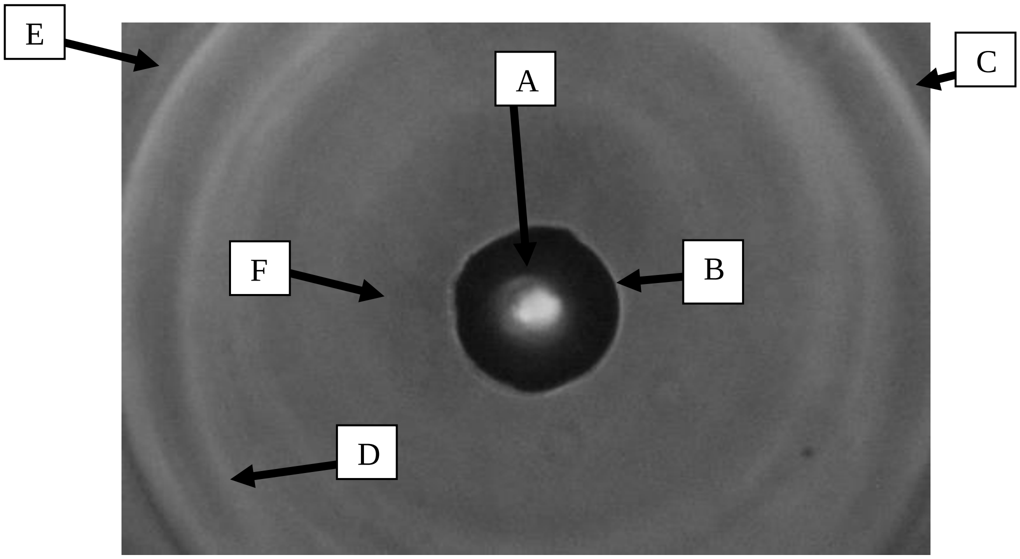

Figure 28b: 300ns Phase Contrast image.

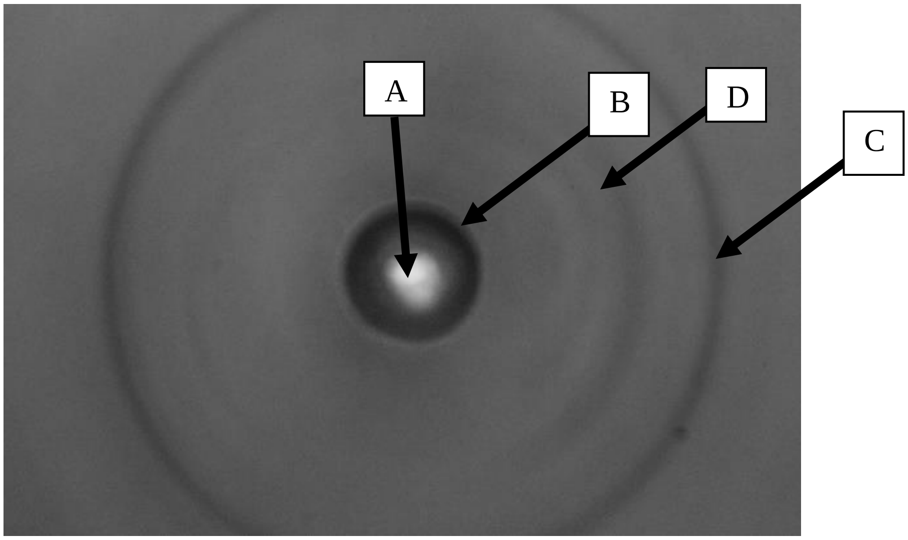

Figure 28c: 200 ns Brightfield image.

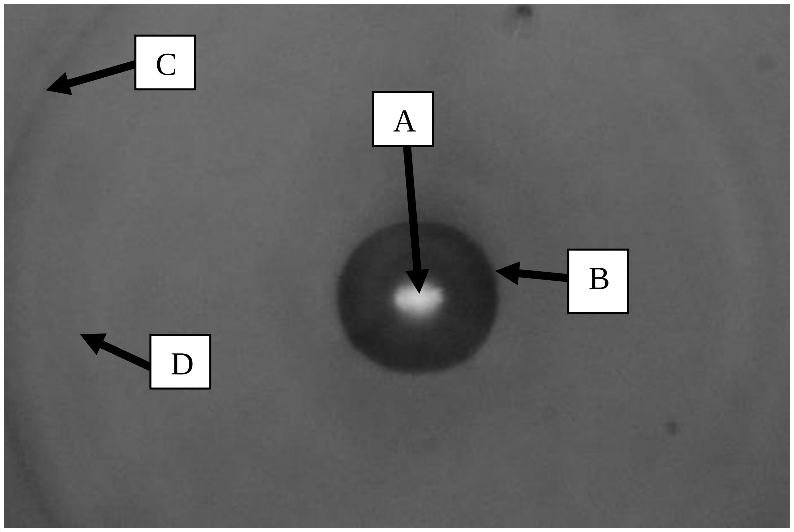

Figure 28d: 300 ns Brightfield image.

All the cavitation images in figures 28a to 28d contain a bright center (labeled A), a dark circle that surrounds the bright center (labeled B), and a dark ring (labeled C). The bright center is caused by the plasma light created with the avalanche breakdown. Since the shutter is opened before the laser pulse arrives, the unwanted plasma emission during the entire micro-cavitation process is captured with the camera along with the wanted amplitude images generated with the pulsed laser light. The dark circle (labeled B) surrounding the bright center likely represents the cavitation bubble. As the dark region appears in both the brightfield and phase contrast images, the bubble is likely visible due to diffraction as the water vapor inside the bubble and the liquid water surrounding it has a refractive index difference of ~.33 [43]. The large refractive index difference, along the spherical profile of the bubble would diffract light away from the objective, leaving a dark circle in figures 28a to 28d.

The dark ring (labeled C) indicates the location of the cavitation-induced shockwave front. The ring in phase contrast has higher contrast compared to the ring in the brightfield images. The higher contrast indicating that the shockwave is likely visible due to diffraction rather than absorption. This matches the underlying theory of shockwaves, which are extremely thin regions where flow properties change drastically. One of these flow properties is density, which can affect light diffraction[54]. After the shockwave front, the density becomes high causes the light to diffract away from the front. The objective does not collect this light and thus the region around the shockwave front appears dark in both the brightfield and phase contrast images.

However there are more features in Figure 28a and 28b. A bright ring (labeled E) surrounds the dark ring (labeled C). This bright ring is likely the halo effect as it is a reversal of intensity at the edge of a non-linear refractive index change. The halo effect also appears around the bubble boundary (labeled B), however the halo is much thinner the most of the diffracted light on the bubble boundary does not get collected by the objective. In between the dark circle and dark ring in Figure 28a are bright and dark periodic interference patterns. The transition from light to dark is likely due to the gradually increasing phase shift as the axial thickness of the spherical high pressure region get thicker near the center. However, the features are not symmetric, which does not match the spherical nature of the shockwave image. Further possible explanations of the circular features can be surmised from the analysis of the corresponding brightfield images in Figures 28c and 28d. The brightfield images also contains some unclear features and are more faded compared the phase contrast one (labeled D), which indicates that phase contrast can better resolve the bright and dark periodic interference patterns.

One possible cause of the features could be non-uniform high pressure regions between the bubble and shockwave. The bubble boundary being non-spherically at times <200ns in both BF and PS is can been seen as evidence that there are unsymmetrical pressures regions between the bubble and shockwave boundary. The non-spherical boundary would indicate that the pressure at the bubble boundary is not uniform. As the bubble boundary does not have uniform pressure, fluid continuity would dictate that part of the region between the bubble and shockwave contain unsymmetrical pressure regions to match the bubble boundary condition. Another possible cause for the unsymmetrical features can be found in a previous study. Dr. Vogel's paper viewed the cavitation process tangentially to the laser direction as opposed to normally like in our study [15]. Figure 29 illustrate the cavitation process in using the tangential direction as presented in Dr. Vogel paper.

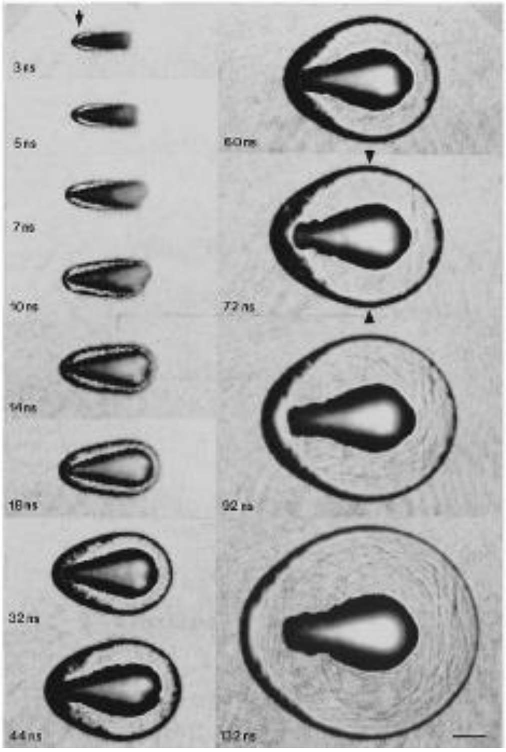

Figure 29: Side view of the microcavitation process. a 10-mJ pulse with 6 ns duration reproduced from Vogel, A., S. Busch, and U. Parlitz, Shock wave emission and cavitation bubble generation by picosecond and nanosecond optical breakdown in water. *Journal of the Acoustical Society of America, 1996.* ***100****(1): p. 148-165. With the permission of the Acoustical Societyof America [15]. The laser light is incident from the right. Arrow marks the location of the beam waist. Arrowheads mark the location of the shockwave. The time delay of the illumination pulse with respect to the pulse producing the plasma is indicated on each frame. The plasma radiation is visible on each frame, because the photographs were taken in a darkened room with open camera shutter. Shock wave and cavitation bubble are visualized at the time when the illumination pulse passes the object. The scale represents a length of 100 mm.*

While the pulse energy in this set of Vogel's experiments (~10 mJ) is higher than our experiments (~8 mJ), they are close enough to be used to analyze our early microcavitation images. The images in Figure 29 indicate that the shockwave and the bubble were elongated for at least 132 ns. As it is known that the plasma formation can be unstably initiated in the final version microscopy setup, the elongated shockwave and bubble can be tilted. Part of the tilted shockwave can be imaged as unsymmetrical periodic patterns.

Figure 28b also has these features, but fewer of them. Furthermore, the region immediately surrounding the bubble (labeled F) has a uniform intensity. The features instead are closer to the shockwave. The feature progression away from the bubble still matches the two explanations for them. The bubble in Figure 28b is more spherical, indicating that the pressure might be more uniform around the bubble at 300 ns. Vogel's paper also indicates that the shockwave becomes more spherical over time, which will reduce the effect the tilt has on creating the features.

Further image analysis can be done by comparing the evolution of the phase contrast and brightfield images over time. Comparison of the brightfield and phase contrast imaging of the microcavitation evaluation over time are given in the following figures. Figure 30a compares visually the BF and PS for <200ns. Figure 30b compares visually the BF and PS images collected between 100 and 1000 ns. Figures 32c compares visually BF and PS images collected between 1 μs and 10 μs.

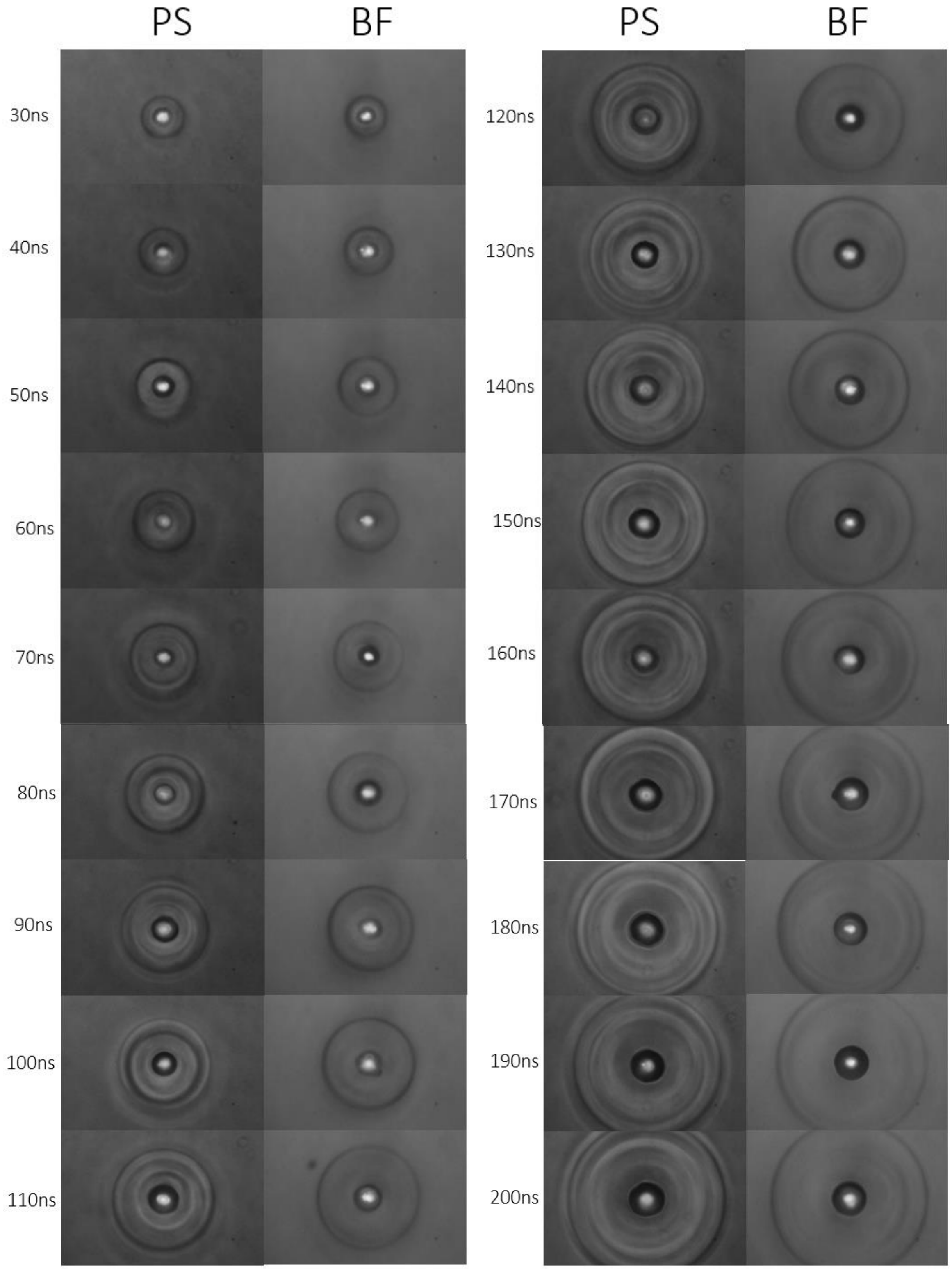

Figure 30a: Early time-lapsed comparison between BF and PS (<200ns) microcavitation images in distilled water.

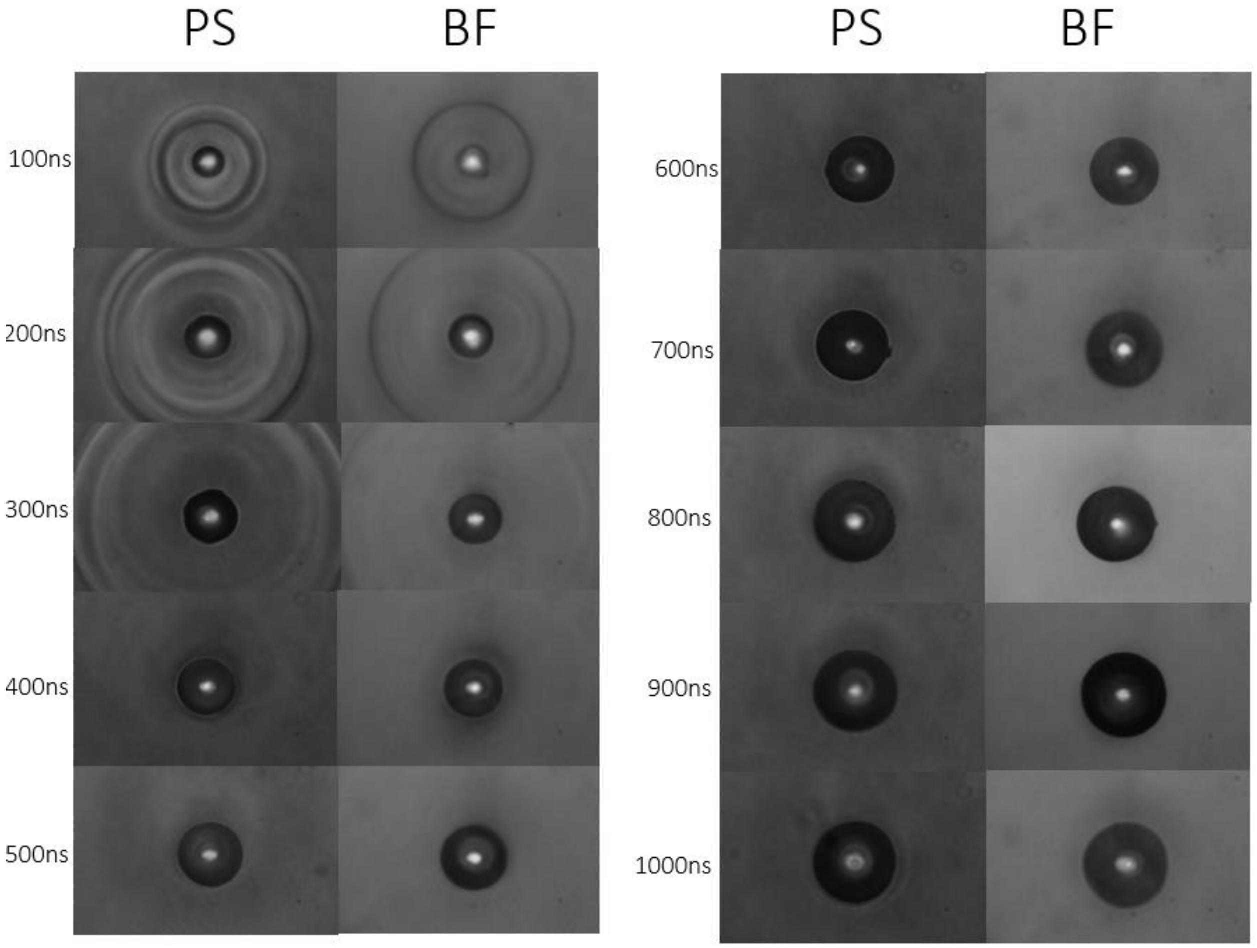

Figure 30b: 100 ns time-lapsed comparison between BF and PS microcavitation images in distilled water.

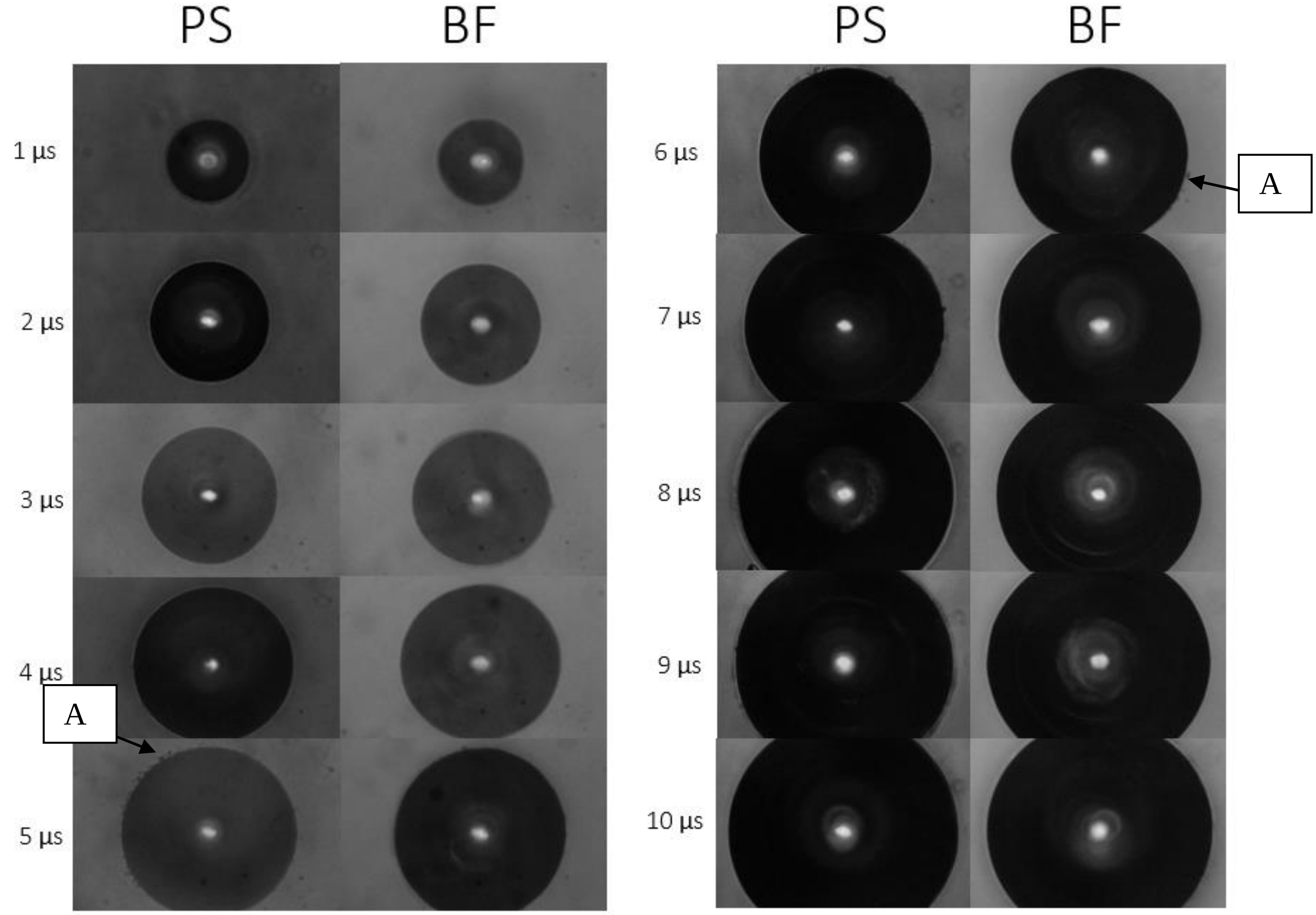

Figure 30c: 1 µs time-lapsed comparison between BF and PS microcavitation images in distilled water.

As illustrated in Figure 30a, the BF and PS images show similar contrast between the cavitation bubble and it surroundings. Secondary bubbles produced by instability are also visible in both brightfield and phase contrast images and a few of them are labeled A in Figure 30c. The secondary bubble are imaged similarly in brightfield and phase contrast. This similarity may indicates that the bubble does not have a significant phase shift, but it is more likely that the bubble has removed too much light to image the internal bubble features. However, there are four major differences between the bright field and phase contrast images of the cavitation event that can be seen. The first is the features discussed in pre-evolution part of the analysis. The second is that there appears to be a lighter region around the shock wave in Figure 30a. The halo effect around the bubble appears to be around the same over time. The third difference is that the irregularity vapor bubble shape at <200ns is more visible in the phase contrast over the brightfield images. The fourth difference that can be seen between the vapor bubble images in figure 30c after 7 µs. The brightfield bubble images have a brighter region around the plasma light, while the phase contrast images remain dark. This is likely due to lighter getting through the bubble near the center as the bubble boundary become flatter relative to the direction of the illumination light. As the boundary becomes more normal to the direction of the illumination light, less light is likely to be diffracted away from the objective. In phase contrast, the phase plate will reduce the intensity of the undiffracted light to the point where it would be barely visible.

After comparing the phase contrast and brightfield images visually, bubble and shockwave diameters were measured and plotted to identify any changes the PS microscopy would have on imaging the shockwave progression and bubble expansion. The cavitation bubble and shockwave sizes during the early microcavitation (<200 ns) are compared in figures 31a and 31b respectively. The bubble size during late microcavitation (>200 ns) are compared in Figure 31c.

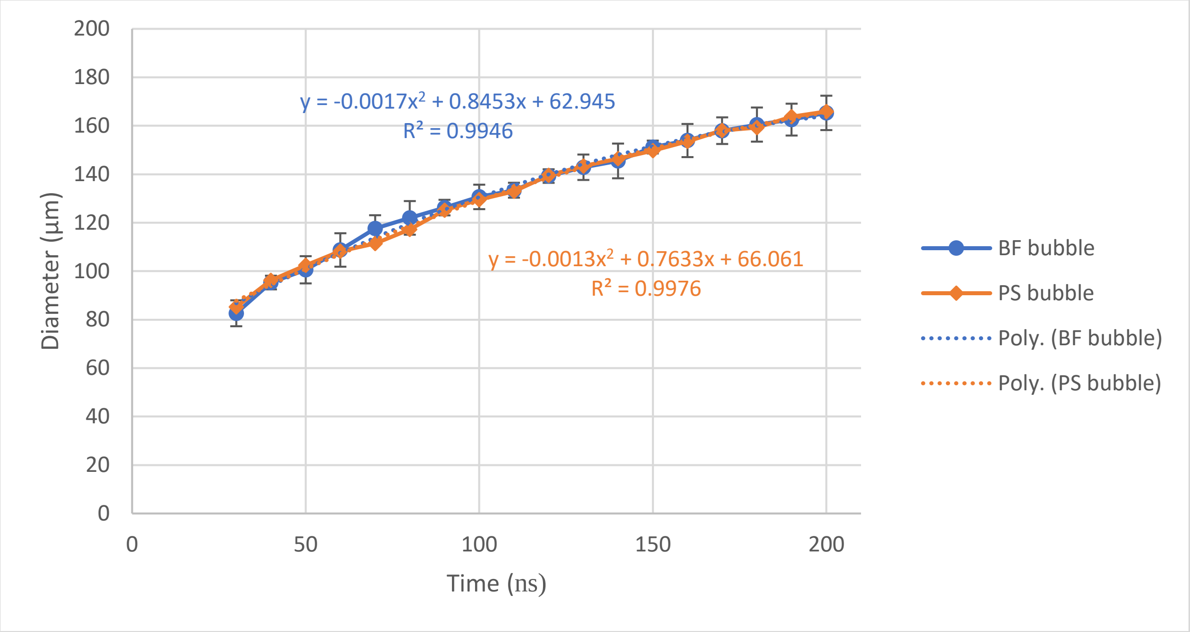

Figure 31a: Early Cavitation bubble diameter measurement comparison between brightfield (BF) and phase contrast (PS) microscopy. Standard deviation determines the error bars.

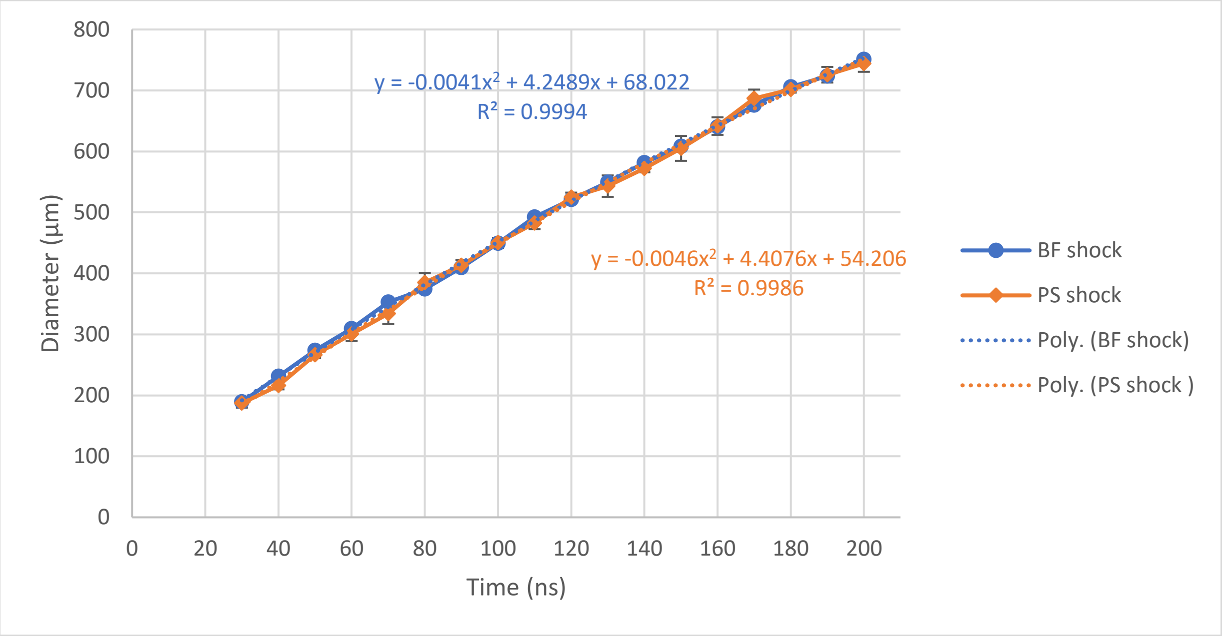

Figure 31b: Shockwave diameter measurement comparison between brightfield (BF) and phase contrast (PS) microscopy. Standard deviation determines the error bars.

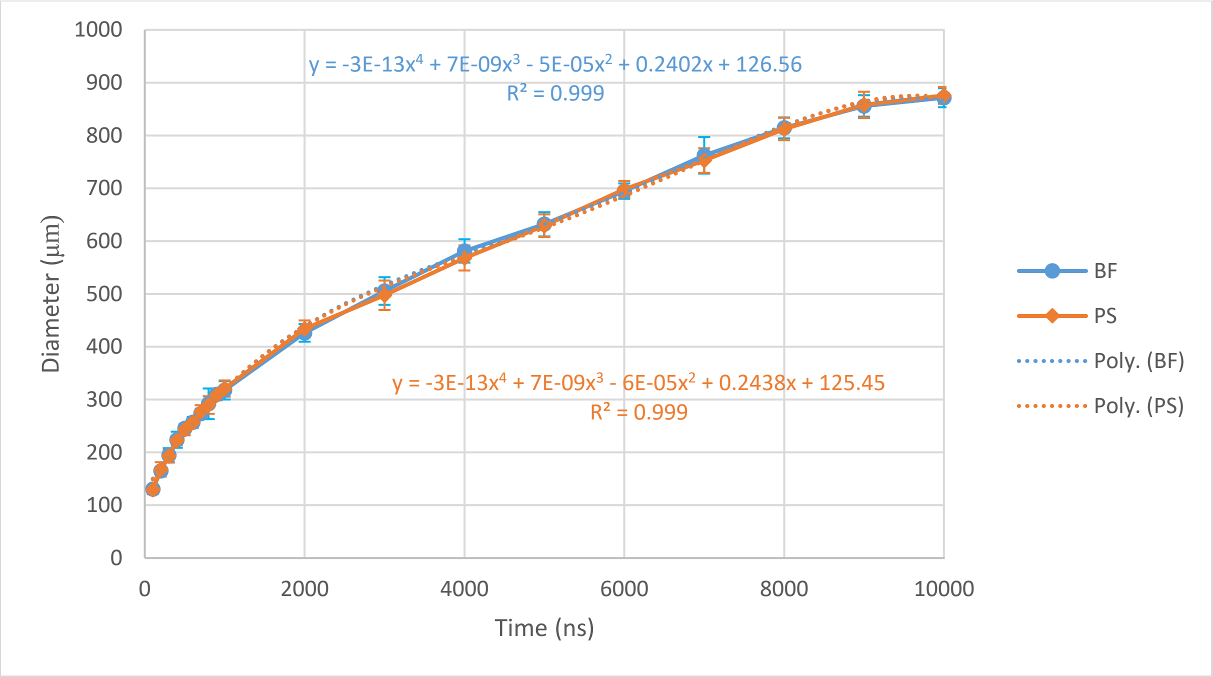

Figure 31c: Late Cavitation bubble diameter measurement comparison between brightfield (BF) and phase contrast (PS) microscopy. Standard deviation determines the error bars.

From the microcavitation plots in figures 31a to 31c, bubble expansion matches within error for all time frames imaged (10 µs). The shockwave progression matches within error for all time frames imaged (<200 ns). The matching plots indicates that we can get consistent results with either BF or PS microscopy method. Getting consistent results with BF microscopy give validation to PS contrast microscopy as BF microscopy is an established imaging method for microcavitation.

5.6 Phase Contrast (PS) vs Brightfield in 10% Polyacrylamide Gel (10% PAA gel)

The cavitation bubble and shockwave sizes during the early microcavitation (<200 ns) in 10% polyacrylamide gel in water solution (10% PAA gel) are compared between phase contrast (PS) and brightfield (BF) in the following figures. Figure 32 compares the images visually. The time evolutions of the diameters of the bubble and spherical shockwave in 10% PAA gel were measured from the images of the PS configuration of the final microscopy setup and plotted in

Figures 33a and 33b respectively. The cavitation bubble and shockwave sizes during the early microcavitation (<200 ns) are compared in Figure 34a and 34b respectively.

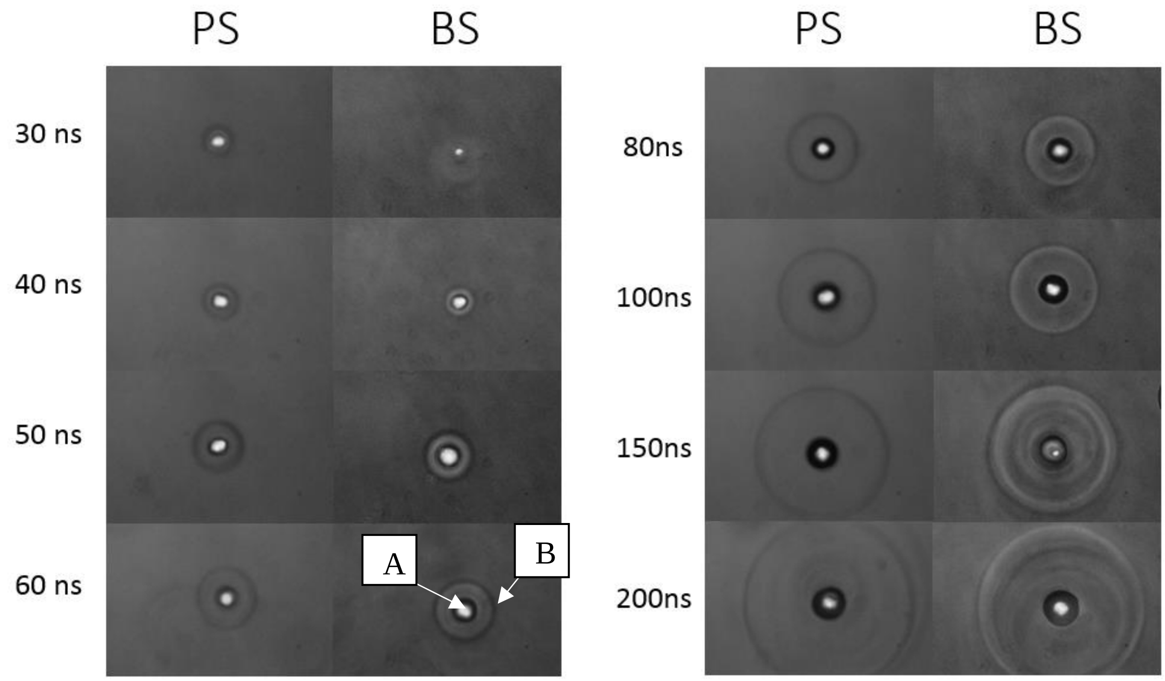

Figure 32: 1 μs time-lapsed comparison between BF and PS microcavitation images in 10% PAA gel.

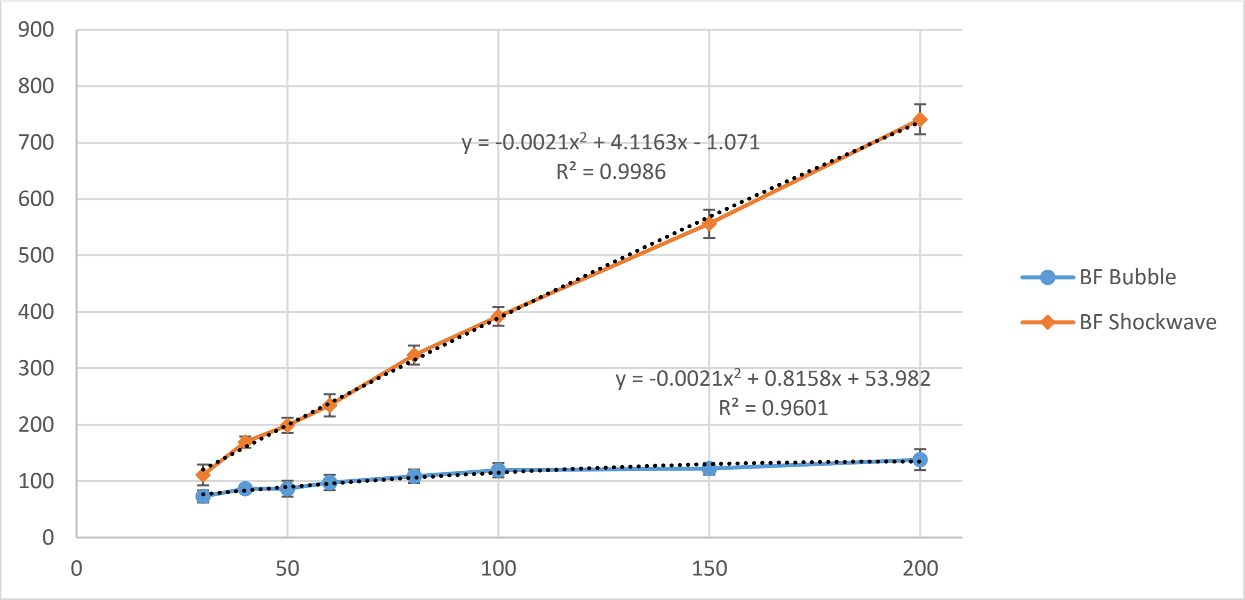

Figure 33a: Evolutions of the sizes of the vapor bubble and both shockwaves from brightfield imaging of laser-induced microcavitation with laser pulse energy at ~2 mJ in 10% PAA gel. Standard deviation determines the error bars.

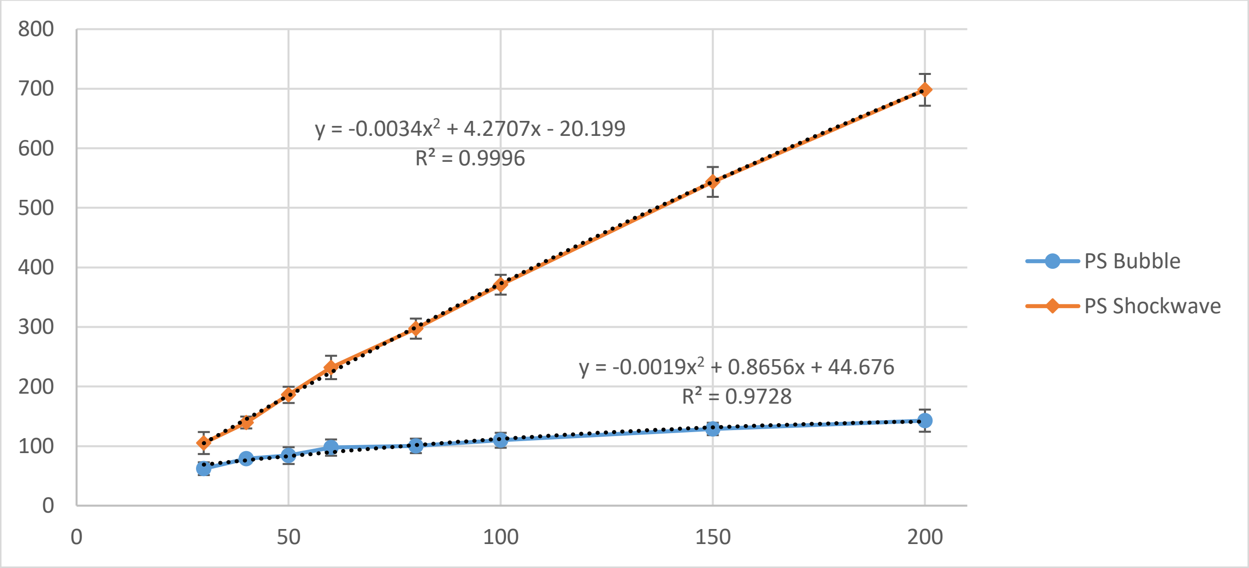

Figure 33b: Evolutions of the sizes of the vapor bubble and both shockwaves from phase contrast imaging of laser-induced microcavitation with laser pulse energy at ~2 mJ in 10% PAA gel. Standard deviation determines the error bars.

As illustrated in Figure 32, the shockwave (labeled B) appears to be a little thinner in the PS images than in the BF images however, the size does look about the same. The region between the shockwave and bubble appear bright until the 60ns time frame in the PS images. The bright region can be attributed to the halo effect as it also occurs in the water images. It is also noted that the circular features appear later (>100 ns).

The general trend of the shockwave and bubble diameters in Figures 33a and 33b seem to match that of the distilled water plots in Figures 26 and 27 with the shockwave diameter expanding at a faster rate than the bubble diameter, including the early expansion speed. The trend line does not match the data as closely as the trend lines in Figures 26 and 27, however this is expected due to the reduced number of imaged times. The negative second order term of all trend lines in Figures 33a and 33b indicate that the shockwave propagation and bubble expansion speed does decelerate over time. Previous studies have shown that shockwave propagation and bubble expansion deceleration do occurs over time [15].

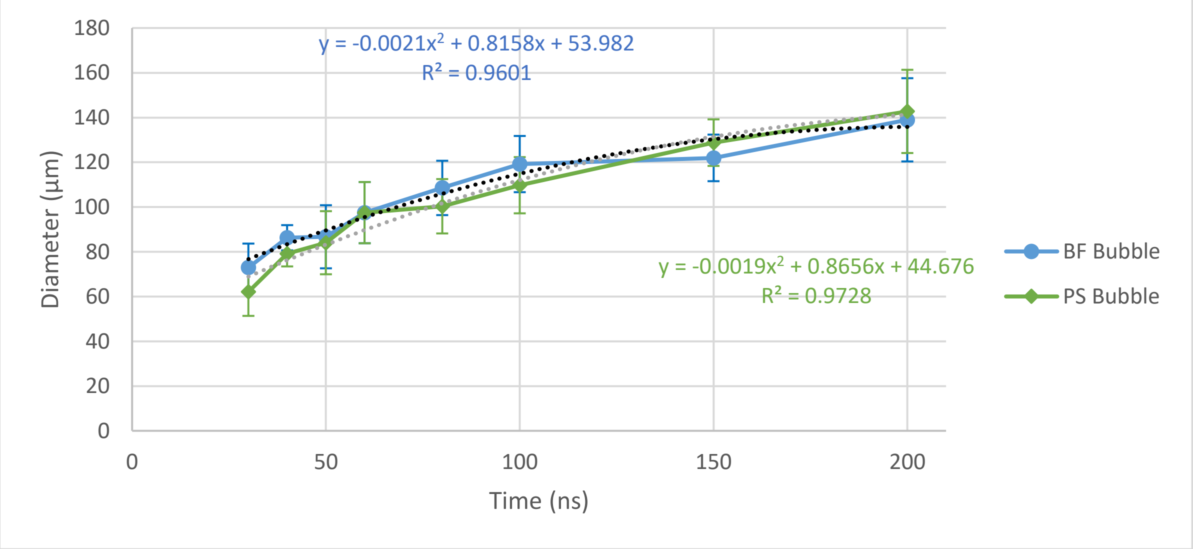

Figure 34a: Bubble comparison of laser-induced microcavitation with laser pulse energy at ~2 mJ in 10% PAA gel. Standard deviation determines the error bars.

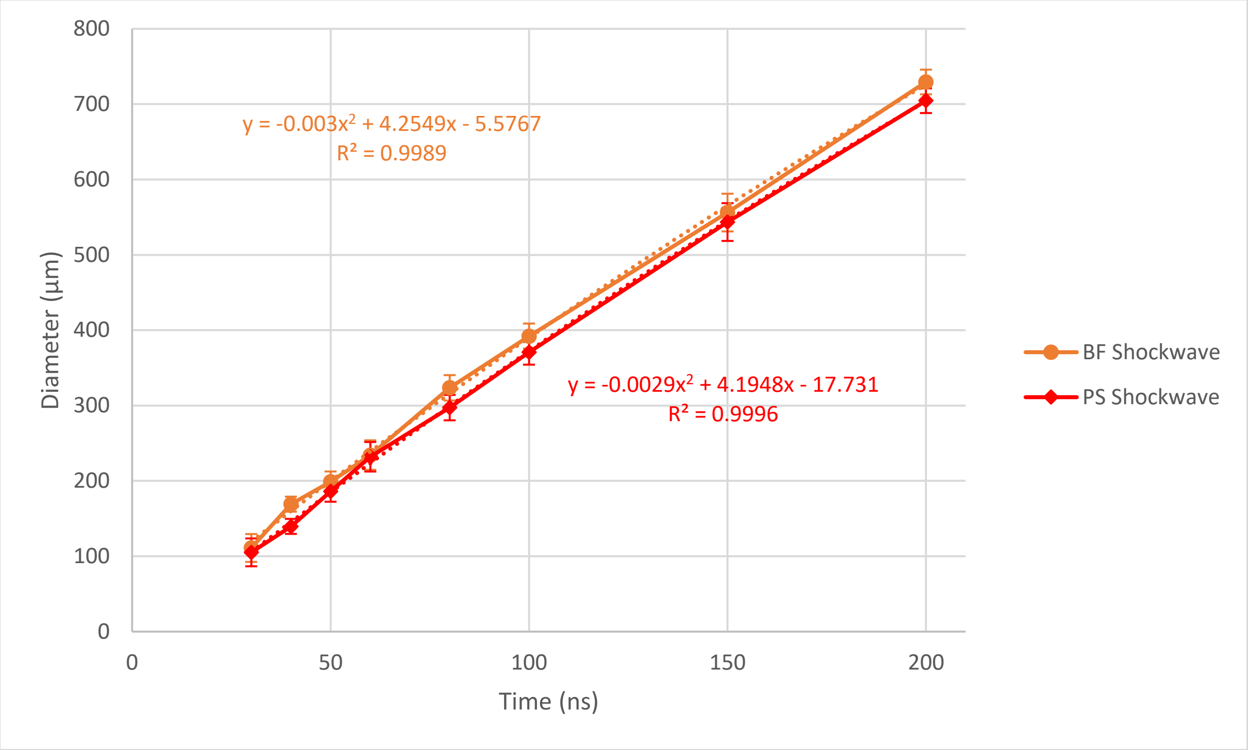

Figure 34b: Shockwave comparison of laser-induced microcavitation with laser pulse energy at ~2 mJ in 10% PAA gel. Standard deviation determines the error bars.

From the microcavitation plots in Figures 34a and 34b, the bubble expansion appear to match for all times up to 200 ns. Note large standard deviation error from unstable cavitation. The average shockwave diameter value is smaller in PS imaging compared to BF imaging in 10% PAA gel. The differences match with the image comparison, as the shockwave boundary does look thinner in PS compared to BF at all times. It is possible that halo effect is enhance the location of the shockwave bubble in PS or that the PS images happen to be photographed with more focus than BF images. However the difference may be insignificant as the error of both shockwave plots overlap.

5.7 Summary

In summary, the brightfield (BF) and phase contrast (PS) images on average indicate that both types of microscopy will measure about the same the bubble and shockwave diameters. The similar measurements holds true for nearly all selected time in both distilled water and 10% polyacrylamide gel in water solution (10% PAA gel). The similar methods can provide validation for PS microscopy due to having consistent results with BF microscopy. Secondary bubbles were also visible in both the BF and phase contrast images, which are probably due to instability at the bubble-fluid interface. One major difference between the BF and PS images are that the halo artifact is present for the both the bubble and shockwave outer boundaries in phase contrast microscopy. The other is the bright and dark periodic interference patterns between the shockwave and bubble boundaries in the PS images. The transition from light to dark in these patterns are likely due to the gradually increasing phase difference as the axial thickness of the spherical high pressure region get thicker near the center. However the bright and dark periodic interference patterns are not symmetric, which does not match the spherical nature of the shockwave image. Further possible explanations of the features can be surmised from the analysis of the corresponding brightfield images. The brightfield images also contains some unclear features and are more faded compared the phase contrast ones. The faded features in the brightfield indicate that the phase contrast is better at resolving the bright and dark periodic interference patterns. One possible cause of the bright and dark periodic interference patterns are unsymmetrical high pressure regions between the bubble and shockwave. As pressure can affect the refractive index of the fluid, non-uniformity pressures can translate to non-uniform intensity amplitude in both brightfield and phase contrast microscopy. Further evidence of the non-uniform pressure comes from the vapor bubble not appearing spherical. Another possible cause of the bright and dark periodic interference patterns is the shockwave being tilted due to the instability of the bubble formation. In short, some of the features were identified as optical artifacts. Causes for the other features are identified, thought additional information is needed to confirm those causes.

6 CONCLUSION AND FUTURE WORK*

6.1 Conclusion

A direct numerical simulation and corresponding pulsed illumination microscopy with an emphasis of phase contrast technique are developed in this study to detailed study the laser-induced micro-cavitation process happening in most laser surgeries with water-rich tissues. Note that no direct numerical simulation of laser-induced micro-cavitation during a laser surgery has been presented before. Also, no pulsed illumination phase contrast microscopy has been constructed before. Pulsed illumination phase contrast microscopy allows measuring the evolution of the vapor bubble and shockwave from a laser-induced micro-cavitation with ns time resolution. From the pulsed illumination phase contrast microcopy, the average speed of the shock wave in both water and 10% PAA gel were ~1600 m/s. This value is similar to ~1800 m/s obtained from the direct simulation. Though the shock wave propagation shows a good agreement between the experiment and the direct simulation, the evolution of the vapor bubble shows less consistency between the experimental and the simulation: where the simulation predicts an evolution of the vapor bubble from elliptical to spherical shape in the first 1 µs after the laser pulse, and the shape of the vapor bubble is a spherical shape from ~20 ns after the laser pulse based on the experiment. Also, the vapor bubble expands at a much lower speed from the simulation compared with the experimental measurement.

These deviations in the vapor bubble dynamics predicted from the direct simulation and that measured from the experiment can be attributed to two main factors. First, the wavelength applied in the simulation and the experimental are ~4 µm and 1 µm, respectively. Water provides

---

* Part of this chapter is reprinted with permission from "Direct numerical simulation of microcavitation processes in different bio environments" by Kevin Ly, Sy-bor Wen, Morgan s. Schmidt, and Robert J. Thomas, 2017. *Optical Interactions with Tissue and Cells Xxviii*, Vol. 100602, Copyright 2017 by SPIE.

two orders of magnitude higher light absorption at λ=4 μm compared with that at λ=1 μm. Therefore, the simulated laser energy to induce the micro-cavitation is ~0.02 mJ which is much lower than E~8 mJ in the experiment. Second, the light absorption mechanism in water at λ=4 μm is mainly due to linear light absorption while the light absorption mechanism in water at λ=1 μm is mainly due to photoionization and the followed plasma formation. The plasma formation can be observed from an interesting feature in all the images from the experiment that have a white light spot in the center that cannot be eliminated with a notch filter at the strobe beam wavelength. For delay times shorter than ~20- 30 ns, the plasma light is too strong, and obscures the features of both the bubble and pressure wave. As the current simulation does not yet account for the plasma formation, it is not surprising that the simulation does not match the results of this portion of the experiment, especially in the evolution of the size/shape of the vapor bubble. As a result, only the propagation speed of the laser-induced shockwave from the experiment can fit from our direct numerical simulation.

The final version of phase contrast microscopy setup is able to resolve additional features between the vapor bubble and shockwave boundary. The outer edge of bubble has higher contrast to the liquid surroundings in phase contrast microscopy compared to brightfield microscopy. However, the high contrast edge did not significantly affect the bubble diameter measurements as diameter measurements match between BF and PS microscopy with small deviations. One major difference between the brightfield and phase contrast images are that the halo artifact is present for both bubble and shockwave outer boundaries in phase contrast microscopy. Another is the circular features between the shockwave and bubble boundaries in the phase contrast images. The transition from light to dark in these features are likely due to the gradually increment of phase difference as the axial thickness of the spherical high pressure region get thicker near the center.

However, the additional features observed in PS microscopy are not symmetric, which does not match the spherical nature of the shockwave image. One possible reason is due to having non-symmetric high pressure regions between the bubble and shockwave. As pressure can affect the refractive index of the fluid, non-symmetric pressures can translate to non-symmetric intensities. As the bubble appears not uniform in the early microcavitation images, then it is possible that the bubble interface is causing some instability in the high pressure region. As the bubble does become more spherical later one, the region around the bubble has a uniform intensity, and the number of bright and dark periodic interference patterns are reduced. One possible cause of the bright and dark periodic interference patterns is unsymmetrical high pressure regions between the bubble and shockwave. As pressure can affect the refractive index of the fluid, unsymmetrical pressures can translate to unsymmetrical bright and dark patterns in phase contrast microscopy. Further evidence of the non-uniform pressure comes from the vapor bubble not appearing spherical. Another possible cause of the feature is the shockwave being tilted due to the instability of the bubble formation. Another possible explanation of the non-symmetric PS interference rings can be due to the elongated vapor bubble. The elongation is identified by images that are taken from the side point of view (Figure 41). In short, PS microscopy can more clearly image the irregularity of bubble boundary at <200ns and identify additional features causing phase angle changes between the shockwave and bubble boundaries. The features indicate that the refractive index and the corresponding pressure field in the shockwave is non-uniform. In other words, compared with bright field imaging, pulsed illumination PS does advance our understanding of the microcavitation process. However additional information needs to be acquired to quantify the bright and dark periodic interference patterns between the bubble and shockwave as identified by PS microscopy.

6.2 Future Work

For the future of the numerical model, we will integrate cascade ionization in our direct numerical simulation to better analyze the evolution of the vapor bubble during laser-induced micro-cavitation with a shorter IR wavelength laser pulse, as shorter IR wavelength pulses can be better absorbed by transparent tissue.

In order to more accurately image the cavitation event in phase contrast microscopy, the initiation of the avalanche breakdown should be placed at a more stable spot by raising the numerical aperture closer to 1. Additional microcavitation images should also be taken in the side view orientation to better identify the causes of the bright and dark periodic interference patterns observed in this study. Experiments could also then be done on other transparent tissues like cartilage to analyze any additionally features on a more rigid tissue. Additionally, Differential interference contrast (DIC) microscopy should be used in conjunction with phase contrast microscopy to make a more quantitative study as phase contrast alone can only give a qualitative image of phase angle change due to absorption and change of refractive indices. DIC observes the gradient of phase shift rather than the phase shift magnitude. Using DIC can help determine if the transition from a light to dark region is due to change of the optical path length. DIC also can eliminate the halo effect, which was an optical artifact that affect the analysis of the shockwave in the microcavitation process. The ability to image the phase shift gradient is particularly useful in quantitatively analyzing the bright and dark periodic interference patterns in the region between the cavitation bubble and shockwave. The halo effect is eliminated due to the setup not needing a phase plate that geometrically interact with two types of light (undiffracted and diffracted) separately. Note that phase contrast microscopy is still important in the analysis as DIC is not designed to measure the phase shift amplitude directly.

REFERENCES

1. Huang, S.C. and H.C. Chen, *Overview of laser refractive surgery.* Chang Gung Med J, 2008. **31**(3): p. 237-52.

2. Müller, G., K. Dörschel, and H. Kar, *Biophysics of the Photoablation Process.* Lasers in Medical Science, 1991. **6**(3): p. 14.

3. Vij, D.R. and K. Mahesh, *Medical applications of lasers*. 2002, Boston: Kluwer Academic. xii, 375 p.

4. Jansen, E.D., et al., *Laser-tissue interaction during transmyocardial laser revascularization.* Ann Thorac Surg, 1997. **63**(3): p. 640-7.

5. Niemz, M.H., *Laser-Tissue Interactions: Fundamentals and Applications*. Third ed. 2007: Springer.

6. Dick, H.B., M. Elling, and A. Willert, *Femtosecond laser in ophthalmology – A short overview of current applications.* Medical Laser Application, 2010. **25**(4): p. 258-261.

7. Andrews, D.L., *Multiphoton absorption in molecules*, in *Molecular Photophysics and Spectroscopy*. 2014, Morgan & Claypool Publishers. p. 14-1-14-7.

8. Fang, C., et al., *The accurate calculation of the band gap of liquid water by means of GW corrections applied to plane-wave density functional theory molecular dynamics simulations.* Physical Chemistry Chemical Physics, 2015. **17**(1): p. 365-375.

9. Conrads, H. and M. Schmidt, *Plasma generation and plasma sources.* Plasma Sources Science & Technology, 2000. **9**(4): p. 441-454.

10. Ready, J.F., *Effects of high-power laser radiation*. xiii, 433 pages.

11. Vogel, A. and V. Venugopalan, *Mechanisms of pulsed laser ablation of biological tissues.* Chem Rev, 2003. **103**(2): p. 577-644.

12. Wan, M., Y. Feng, and G. Haar, *Cavitation in Biomedicine: Principles and Techniques*. 2016: Springer Netherlands.

13. Vogel, A., et al., *Femtosecond-laser-induced nanocavitation in water: Implications for optical breakdown threshold and cell surgery.* Physical Review Letters, 2008. **100**(3).

14. Brujan, E.A., et al., *The final stage of the collapse of a cavitation bubble close to a rigid boundary.* Physics of Fluids, 2002. **14**(1): p. 85-92.

15. Vogel, A., S. Busch, and U. Parlitz, *Shock wave emission and cavitation bubble generation by picosecond and nanosecond optical breakdown in water.* Journal of the Acoustical Society of America, 1996. **100**(1): p. 148-165.

16. Blake, J.R., et al., *The interaction of a cavitation bubble with a rigid boundary.* Sonochemistry and Sonoluminescence, 1999. **524**: p. 87-96.

17. Kodama, T. and Y. Tomita, *Cavitation bubble behavior and bubble-shock wave interaction near a gelatin surface as a study of in vivo bubble dynamics.* Applied Physics B-Lasers and Optics, 2000. **70**(1): p. 139-149.

18. Schmidt, M.S., et al., *Temperature dependence of nanosecond laser pulse thresholds of melanosome and microsphere microcavitation.* Journal of Biomedical Optics, 2016. **21**(1).

19. Schmidt, M.S., et al., *Trends in nanosecond melanosome microcavitation up to 1540 nm.* Journal of Biomedical Optics, 2015. **20**(9).

20. Schmidt, M.S., et al., *Trends in melanosome microcavitation thresholds for nanosecond pulse exposures in the near infrared.* Journal of Biomedical Optics, 2014. **19**(3).

21. Liu, Z.J., et al., *Real-time brightfield, darkfield, and phase contrast imaging in a light-emitting diode array microscope.* Journal of Biomedical Optics, 2014. **19**(10).

22. Schmidt, M.S., et al., *Trends in nanosecond melanosome microcavitation up to 1540 nm.* J Biomed Opt, 2015. **20**(9): p. 095011.

23. Brujan, E.A., et al., *Dynamics of laser-induced cavitation bubbles near an elastic boundary.* Journal of Fluid Mechanics, 2001. **433**: p. 251-281.

24. Vogel, A., et al., *Cavitation bubble dynamics and acoustic transient generation in ocular surgery with pulsed neodymium: YAG lasers.* Ophthalmology, 1986. **93**(10): p. 1259-69.

25. Kelly, M.W. and C.P. Lin, *Microcavitation and cell injury in RPE cells following short-pulsed laser irradiation.* Laser-Tissue Interaction Viii, Proceedings Of, 1997. **2975**: p. 174-179.

26. Leboffe, M.J. and B.E. Pierce, *A Photographic Atlas for the Microbiology Laboratory*. 2012: Morton Publishing Company.

27. Thorn, K., *A quick guide to light microscopy in cell biology.* Mol Biol Cell, 2016. **27**(2): p. 219-22.

28. Arnison, M.R., et al., *Linear phase imaging using differential interference contrast microscopy.* Journal of Microscopy, 2004. **214**(1): p. 7-12.

29. Zernike, F., *Phase contrast, a new method for the microsopic observation of transparent objects.* Physica, 1942. **9**: p. 686-698.

30. Murphy, D.B., *Fundamentals of light microscopy and electronic imaging.* 2001.

31. Flynn, H.G., *Cavitation Dynamics .1. Mathematical Formulation.* Journal of the Acoustical Society of America, 1975. **57**(6): p. 1379-1396.

32. Muller, S., P. Helluy, and J. Ballmann, *Numerical simulation of a single bubble by compressible two-phase fluids.* International Journal for Numerical Methods in Fluids, 2010. **62**(6): p. 591-631.

33. Zein, A., M. Hantke, and G. Warnecke, *On the modeling and simulation of a laser-induced cavitation bubble.* International Journal for Numerical Methods in Fluids, 2013. **73**(2): p. 172-203.

34. Ahmed, T.H., *Equations of state and PVT analysis: applications for improved reservoir modeling*. 2007: Gulf Pub.

35. Wagner, W.a., *International Steam Tables Properties of Water and Steam Based on the Industrial Formulation IAPWS-IF97*. 2008: 2nd ed. Berlin, Heidelberg : Springer Berlin Heidelberg, 2008.

36. Barr, V.A. and S.C. Bunnell, *Interference Reflectance Microscopy*. Current protocols in cell biology / editorial board, Juan S. Bonifacino ... [et al.], 2009. **CHAPTER**: p. Unit-4.23.

37. Bhattacharjee, S., *DLS and zeta potential - What they are and what they are not?* J Control Release, 2016. **235**: p. 337-351.

38. Preza, C., D.L. Snyder, and J.A. Conchello, *Theoretical development and experimental evaluation of imaging models for differential-interference-contrast microscopy*. Journal of the Optical Society of America a-Optics Image Science and Vision, 1999. **16**(9): p. 2185-2199.

39. Murphy, D.B., *Fundamentals of light microscopy and electronic imaging*. 2001, New York: Wiley-Liss. xii, 368 p.

40. Fisher, R.A. and W. Bischel, *Role of Linear Dispersion in Plane-Wave Self-Phase Modulation.* Applied Physics Letters, 1973. **23**(12): p. 661-663.

41. Kohler, D., et al., *Speckle Reduction in Pulsed-Laser Photographs.* Optics Communications, 1974. **12**(1): p. 24-28.

42. Santhanam, J. and G.P. Agrawal, *Raman-induced spectral shifts in optical fibers: general theory based on the moment method.* Optics Communications, 2003. **222**(1-6): p. 413-420.

43. Hutton, C., *A philosophical and mathematical dictionary, containing an explanation of the terms, and an account of the several subjects, comprised under the heads mathematics, astronomy, and philosophy both natural and experimental; with an historical account of the rise, progress, and present state of these sciences; also memoirs of the lives and writings of the most eminent authors, both ancient and modern, who by their discoveries or improvements have contributed to the advancement of them*. New ed. 1815, London,: Printed for the author etc.

44. Anderson, J.D., *Fundamentals of aerodynamics*. 5th ed. Anderson series. 2011, New York: McGraw-Hill. xxiii, 1106 p.

45. Yadav, H.S., et al., *Measurement of Refractive-Index of Water under High Dynamic Pressures.* Journal of Applied Physics, 1973. **44**(5): p. 2197-2200.

46. Bennett, A.H., *Phase microscopy; principles and applications*. 1951, New York,: Wiley. 320 p.

47. Bioimager. *Phase Contrast Microscopy*. 2017 [cited 2018; Available from: https://www.bioimager.com/blog/post_/phase_contrast/.

48. Diez-Silva, M., et al., *Shape and Biomechanical Characteristics of Human Red Blood Cells in Health and Disease.* Mrs Bulletin, 2010. **35**(5): p. 382-388.

49. Manohar Reddy, N., et al., *A study on Refractive index of plasma of blood of patients suffering from Tuberculosis.* International Journal of Innovative Technology and Creative Engineering, 2012. **VOL.2**: p. 23-25.

50. Buddhiwant, P., et al. *Simultaneous determination of size and refractive index of red blood cells by light scattering measurements*. in *(CLEO). Conference on Lasers and Electro-Optics, 2005.* 2005.

51. Vogel, A., et al., *Cavitation Bubble Dynamics and Acoustic Transient Generation in Ocular Surgery with Pulsed Neodymium - Yag Lasers.* Ophthalmology, 1986. **93**(10): p. 1259-1269.

52. Vogel, A., W. Lauterborn, and R. Timm, *Optical and acoustic investigations of the dynamics of laser-produced cavitation bubbles near a solid boundary*. Journal of Fluid Mechanics, 1989. **206**: p. 299-338.

53. Cole, R.H., *Spherical Shock Waves from Underwater Explosions.* Physical Review, 1947. **72**(2): p. 177-177.

54. Anderson, J.D., *Fundamentals of aerodynamics*. 4th ed. McGraw-Hill series in aeronautical and aerospace engineering. 2007, Boston: McGraw-Hill Higher Education. xxiv, 1008 p.